28

Dynamic Nanometer Alignment for Nanofabrication and Metrology

by

Euclid E. Moon

Submitted to the Department of Electrical Engineering and Computer Science in partial fulfillment of the requirements for the degree of

Master of Science in Electrical Engineering and Computer Science
at the

MASSACHUSETTS INSTITUTE OF TECHNOLOGY
September, 1998

© Massachusetts Institute of Technology, 1998.

All rights reserved.

Signature of Author..
Department of EECS
Sept. 8, 1998

Certified by................ ....
Henry I. Smith
Keithly Professor of Electrical Engineering
Thesis Supervisor

Accepted by...
Arthur Smith
Chairman, Undergraduate Thesis Committee

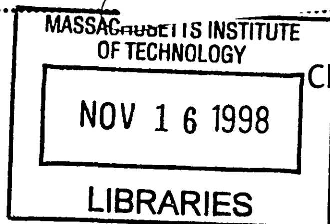

Eng

Dynamic Nanometer Alignment for Nanofabrication and Metrology

by
Euclid E. Moon

Submitted to the Department of Electrical Engineering and Computer Science
on Sept. 8, 1998 in partial
fulfillment of the requirements
for the Degree of Master of Science

Abstract

Future generations of IC fabrication depend in part on continued improvements in lithography. To meet the lithographic challenges posed by 25-nm lithography, a novel through-the-mask, interferometric imaging alignment method is described that has demonstrated detectivity below 1 nm. A proximity x-ray alignment and exposure system was constructed which incorporates this "Interferometric Broadband Imaging" (IBBI) alignment scheme. IBBI employs complementary grating and checkerboard-type alignment marks on mask and wafer, respectively. Interference fringes are imaged onto a CCD camera when viewing the marks at a Littrow angle of 15 degrees. Alignment is signified by the spatial phase discontinuities between two identical sets of interference fringes that move in opposite directions as the mask is translated relative to the wafer.

The robustness of IBBI was verified by demonstrating that the relative spatial phase is not affected when overlayers of resist, polysilicon, or aluminum cover the alignment marks. Further verification of robustness was found when the illuminating and viewing beams traversed long optical paths through air, glass, and helium. It is significant that IBBI measurements are made external to a helium enclosure through the above optical paths, since this allows continuous observation of alignment during exposure.

Feedback stabilization was developed to nullify the effects of thermal drift and mechanical disturbances during exposure. Over several hours the relative position of the mask and wafer was demonstrated to be locked to within σ=1.4 nm.

Thesis Supervisor: Professor Henry I. Smith
Title: Keithly Professor of Electrical Engineering

Dedication

To the letters P, D, A, L, A, T, M

and the numbers 2, 6, 21, 250.

Quoteable Quotes:

"... there's a party in my mind..."

- Alberto Moel

Acknowledgements

A great debt is owed to Prof. Hank Smith for his faith in me and his receptivity to ideas, to say nothing of his incisive questions that *always* go right to the heart of the matter, his inspirational presentation style and his superhuman enthusiasm.

Many thanks are due to David Breslau, whose talent in design was always a source of inspiration and pleasure.

To the students and staff in the NSL who made the lab an enjoyable place to work:

First, I would like to thank Alberto Moel, who mentored me through my first years as a UROP. His unique, vibrant, and sometimes unpredictable personality was one of the best parts of working in the lab. I will never forget his rendition of opera songs in the cleanroom at 3 in the morning.

To Jawoong Lee, who gave me the sense of having been to South Korea, and who was forever leaving me with insights into the differences, as well as the similarities between our countries.

To Patrick Everett, who constantly reminded me of the meaning of a good experiment.

To Maya Farhod, who often injected energy and brightness into some otherwise dull days.

To Mark Mondol, for his memorable Christmas parties, and for introducing me to tofu dogs.

To Kathy Early, who showed us that an 8kV voltage is not always lethal.

To my parents, for their love.

Finally, a debt is owed to RUSH for the following song, capturing a defiant (poetic) energy that sometimes helps one to push on through the most challenging periods:

Cut To The Chase
--- -- --- -----
It is the fire that lights itself
But it burns with a restless flame
The arrow on a moving target
The archer must be sure of his aim

It is the engine that drives itself
But it chooses the uphill climb
A bearing on magnetic north
Growing farther away all the time
Can't stop -- moving
Can't stop -- moving
Can't stop

YOU MAY BE RIGHT
IT'S ALL A WASTE OF TIME
I GUESS THAT'S JUST A CHANCE
I'M PREPARED TO TAKE
A DANGER I'M PREPARED TO FACE
CUT TO THE CHASE

It is the rocket that ignites itself
And launches its way to the stars
A driver on a busy freeway
Racing the oblivious cars

It's the motor of the western world
Spinning off to every extreme
Pure as a lover's desire
Evil as a murderer's dream

Young enough not to care too much
About the way things used to be
I'm young enough to remember the future --
The past has no claim on me

I'm old enough not to care too much
About what you think of me
But I'm young enough to remember the future
And the way things ought to be

WHAT KIND OF DIFFERENCE
CAN ONE PERSON MAKE?
CUT TO THE CHASE

CONTENTS

1) INTRODUCTION

1.1 REMOTE DETECTIVITY AND ROBUSTNESS ANALOGY 12

1.2 ALIGNMENT CONTEXT 14

1.3 OBSTACLES TO NANOMETER ALIGNMENT.................................... 18

1.4 THESIS OUTLINE 20

2) INTERFEROMETRIC BROADBAND IMAGING (IBBI) ALIGNMENT

2.1 PAST ALIGNMENT APPROACHES... 22

2.2 PRINCIPLES OF INTERFEROMETRIC BROADBAND IMAGING ALIGNMENT.. 27

2.3 DETECTIVITY 32

2.4 CAPTURE RANGE 33

2.5 DESIGN CRITERIA SUMMARY 37

3) IMAGE ANALYSIS

3.1 SPATIAL PHASE DETECTION 40

3.2 NON-INTEGER FRINGES 44

3.3 MASK-WAFER AND CAMERA ANGLE 46

3.4 WIDE ACQUISITION ALIGNMENT 48

3.5 SPEED AND EFFICIENCY 50

4) ALIGNMENT AND X-RAY EXPOSURE SYSTEM

4.1 SYSTEM ARCHITECTURE 52

4.2 X-RAY SOURCE 56

4.3 NANO-POSITIONING STAGES 60

4.4 HELIUM ENCLOSURE 67

4.5 BROADBAND LIGHT SOURCE 70

4.6 MICROSCOPES 72

5) EXPERIMENTAL VERIFICATION: IBBI DETECTIVITY AND ROBUSTNESS

5.1 ALIGNMENT DETECTIVITY 75

5.2 DETECTIVITY VARIATION WITH GRATING PERIOD 81

5.3 IMMUNITY TO PROCESS COATINGS 83

5.4 INSENSITIVITY TO ENVIRONMENTAL CONDITIONS 87

6) MEASUREMENT CORROBORATION WITH TWO MICROSCOPES

6.1 EXPERIMENTAL SETUP 90

6.2 IBBI-TO-IBBI COMPARISON 93

6.3 IBBI-PIEZO COMPARISON 94

6.4 OBSERVATION OF MAGNIFICATION OFFSET 97

7) FEEDBACK-STABILIZED ALIGNMENT

7.1 THERMAL AND MECHANICAL INSTABILITY: DRIFT AND FLUTTER 101

7.2 FEEDBACK STABILIZATION TO ONE NANOMETER 106

8) CONCLUSION AND FUTURE EFFORTS 110

APPENDIX A

OPERATION OF EXPOSURE SYSTEM 114

APPENDIX B

DETECTION AND CONTROL SOFTWARE 117

APPENDIX C

MICROSCOPE ALIGNMENT 134

APPENDIX D

HEAD 4 MECHANICAL DRAWINGS 137

BIBLIOGRAPHY 163

LIST OF FIGURES

FIGURE 1-1: ARTIST'S CONCEPTION OF THE INTERNATIONAL SPACE STATION 13

FIGURE 1-2: NATIONAL TECHNOLOGY ROADMAP FOR SEMICONDUCTORS 16

FIGURE 1-3: NTRS PREDICTED OVERLAY BUDGET 17

FIGURE 2-1: IBBI ALIGNMENT INFORMATION IS CONTAINED IN THE SPATIAL PHASE 27

FIGURE 2-2: INTERFERENCE FRINGES ARE GENERATED BY SUPERPOSITION 28

FIGURE 2-3: SCHEMATIC OF IBBI ALIGNMENT 29

FIGURE 2-5: TWO IBBI MARKS ELIMINATE PHASE AMBIGUITY 34

FIGURE 2-6: FINE FRINGE ALIGNMENT, COARSE FRINGE AND BAR MISALIGNMENT 36

FIGURE 3-1: STEPS IN PHASE DETECTION ALGORITHM 41

FIGURE 3-4: IMAGES OF THE SAME FRINGE PATTERN WITH THE ROI SHIFTED 45

FIGURE 3-7: INTENSITY DISTRIBUTION OF A SLICE THROUGH A BAR-MARK IMAGE 49

FIGURE 4-1: IBBI ALIGNMENT AND EXPOSURE SYSTEM 53

FIGURE 4-2: SCHEMATIC OF ALIGNMENT/EXPOSURE SYSTEM 55

FIGURE 4-3: PHOTOGRAPH OF AN ELECTRON-BOMBARDMENT X-RAY SOURCE 58

FIGURE 4-4: X-RAY SOURCE IN OPERATION 59

FIGURE 4-5: SCHEMATIC OF MASK AND WAFER 61

FIGURE 4-6: PLOT OF THE MAXIMUM ALLOWABLE MASK-SAMPLE GAP 62

FIGURE 4-7: MIT X-RAY MASK STRUCTURE 64

FIGURE 4-8: PHOTOGRAPH OF MASK AND WAFER WITH WAFER STAGE 65

FIGURE 4-9: PHOTOGRAPH OF MASK IN MASK STAGE 66

FIGURE 4-10: ATTENUATION OF Cu_L X-RAYS THROUGH AIR/HELIUM MIXTURE 68

Figure 4-12: Multi-line argon laser and remote control box 71

Figure 4-13: Uniphase argon laser spectrum 72

Figure 4-14: IBBI microscope 73

Figure 5-1: Fringe pattern observed through IBBI microscope 79

Figure 5-3: Variation of alignment detectivity with grating period 82

Figure 5-4: Image of an IBBI alignment mark etched into silicon 83

Figure 5-5: Immunity of IBBI to overlayers of resist 84

Figure 5-6: Comparison of alignment under different optical paths 87

Figure 5-7: Effect of helium flow on IBBI images 89

Figure 6-1: Alignment observed at two marks simultaneously 91

Figure 6-2: Table of steps taken prior to experiments 92

Figure 6-3: Two IBBI microscopes alternately observe one mark 93

Figure 6-4: Agreement between two simultaneous IBBI measurements 95

Figure 6-5: Printing magnification due to x-ray point source 97

Figure 6-6: IBBI measurements at marks separated in the X-direction 98

Figure 6-7: IBBI measurements at marks separated in the Y-direction 99

Figure 7-1: Vibration of mask/wafer detected simultaneously 102

Figure 7-2: Drift trends of two microscopes 103

Figure 7-3: 150 nm drift in alignment over six hours 104

Figure 7-4: Response of feedback system to large misalignments 107

Figure 7-5: Six-hour alignment data with closed-loop operation 109

CHAPTER 1:

INTRODUCTION

1.1 Remote Detectivity and Robustness Analogy

Let us set the stage with an analogy. Imagine floating in space (Fig. 1-1) and watching the Earth revolve below you. Naturally, you are interested in the goings-on below you. This is of special interest to you since you are on the team building the International Space Station and you are in desperate need of resupplies from Earth to repair the latest system glitch. Your communications are out, but fortunately, you were an optics guru before becoming an astronaut, and you happened to bring a telescope of your own design with you on this visit to the space station. The first thing on your mind is: have the orders been signed to approve the launch of your replacement parts? Now this special telescope has the remarkable power to detect the position of objects

on the Earth to within a millimeter, even though you are orbiting at an altitude of 200 miles.

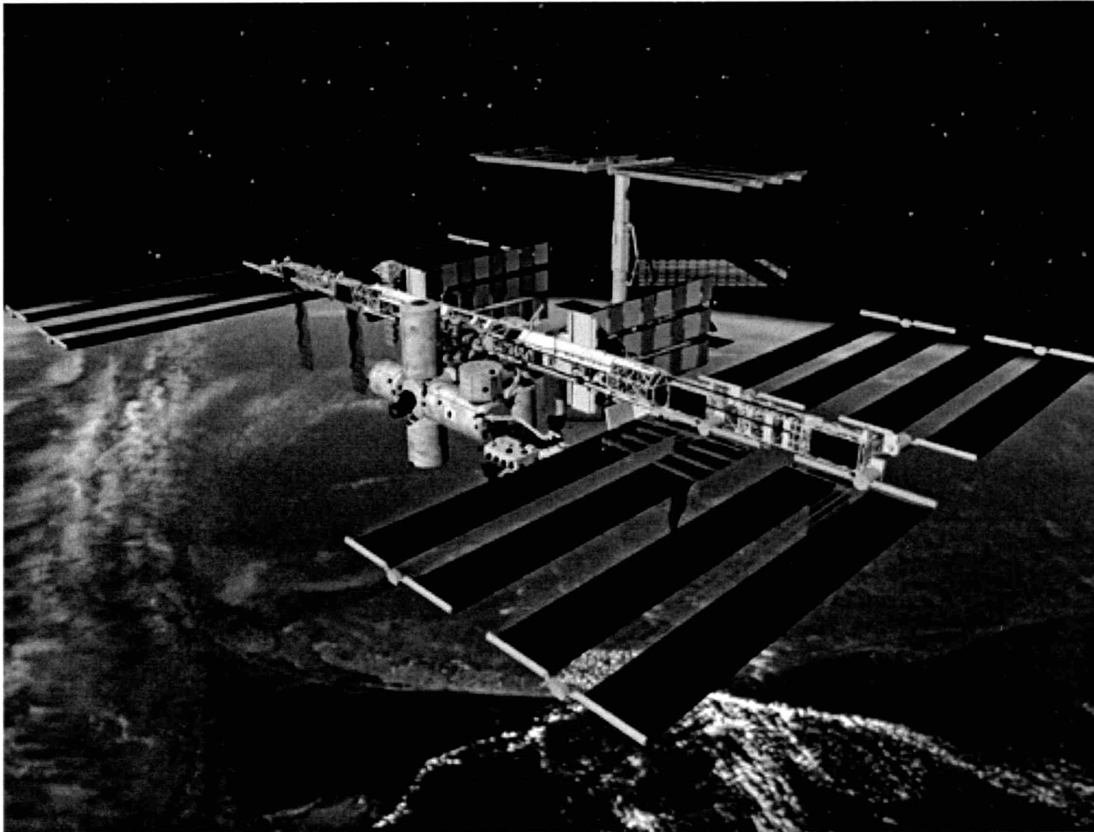

Figure 1-1: Artist's conception of the International Space Station.

As you peer down into NASA headquarters, to your relief you see the Chairman of Space Supplies writing a letter. Using some custom motion-tracking software, you trace out the position of his pen as he writes on the form. Clouds drift over NASA as you are tracking his pen, but your device is not disturbed by their intrusion. To make a long story short, the tracking software traces the words "Send supplies IMMEDIATELY" and you receive the vital components by shuttle the next day.

Considering the reputed resolution of spy satellites, the detectivity of the optics in this fanciful story is not that farfetched. (Of course, we are setting aside the fact that the numerical aperture of such a telescope would be far too large to pack with your personal effects). The point is that both high resolution and immunity to spurious influences can be achieved at relatively long distances. The optics employed in this thesis have a detectivity-to-working distance analogous to the telescope in the story. And this has many advantages, as this thesis will demonstrate.

1.2 Alignment Context

Let us consider the problem of alignment in a simple, mundane context. Every time you make a sandwich you are unconsciously doing alignment. You take a slice of bread, apply a thin film of mayonnaise, align and place a slice of cheese, perhaps some lettuce and tomato, and another slice of bread. In each step you are following the basic premise of aligned fabrication. The success of your culinary attempts depends in large measure on your ability to properly align all the layers of different materials. Consider how difficult it would be to eat a sandwich that had the cheese drooping off one side and the tomato sliding out the other side! In a similar way, a transistor should have its component layers aligned to $1/10^{th}$ of the size of the gate.

In our modern society, so thoroughly integrated with computers, alignment is of considerable commercial and technological interest. To remain competitive, computer chip manufacturers must continuously increase the performance of their products. Historically, decreasing the size of the transistors in the chip has done this. Several advantages accrue with diminishing dimensions:

- reduced power consumption (good for handheld, portable devices)
- reduced signal propagation time
- reduced switching delay
- increased clock speed

To continue the miniaturizing trend there are two fundamental steps that must be taken. The first is to use a wavelength of light that is small enough to define the features. The second is to align a mask and a wafer to about $1/10^{th}$ of the minimum feature size.

Presently, semiconductor fabrication plants make chips with 250 nm minimum feature sizes, or design rules. Over the past 20 years, the miniaturization has followed Moore's "Law", steadily halving feature size every year and a half. Recently, even in the face of increasing technological difficulties, the trend has accelerated. The National Technology Roadmap (Fig. 1-2) now predicts feature sizes (single lines) of 100 nm by the year 2003.

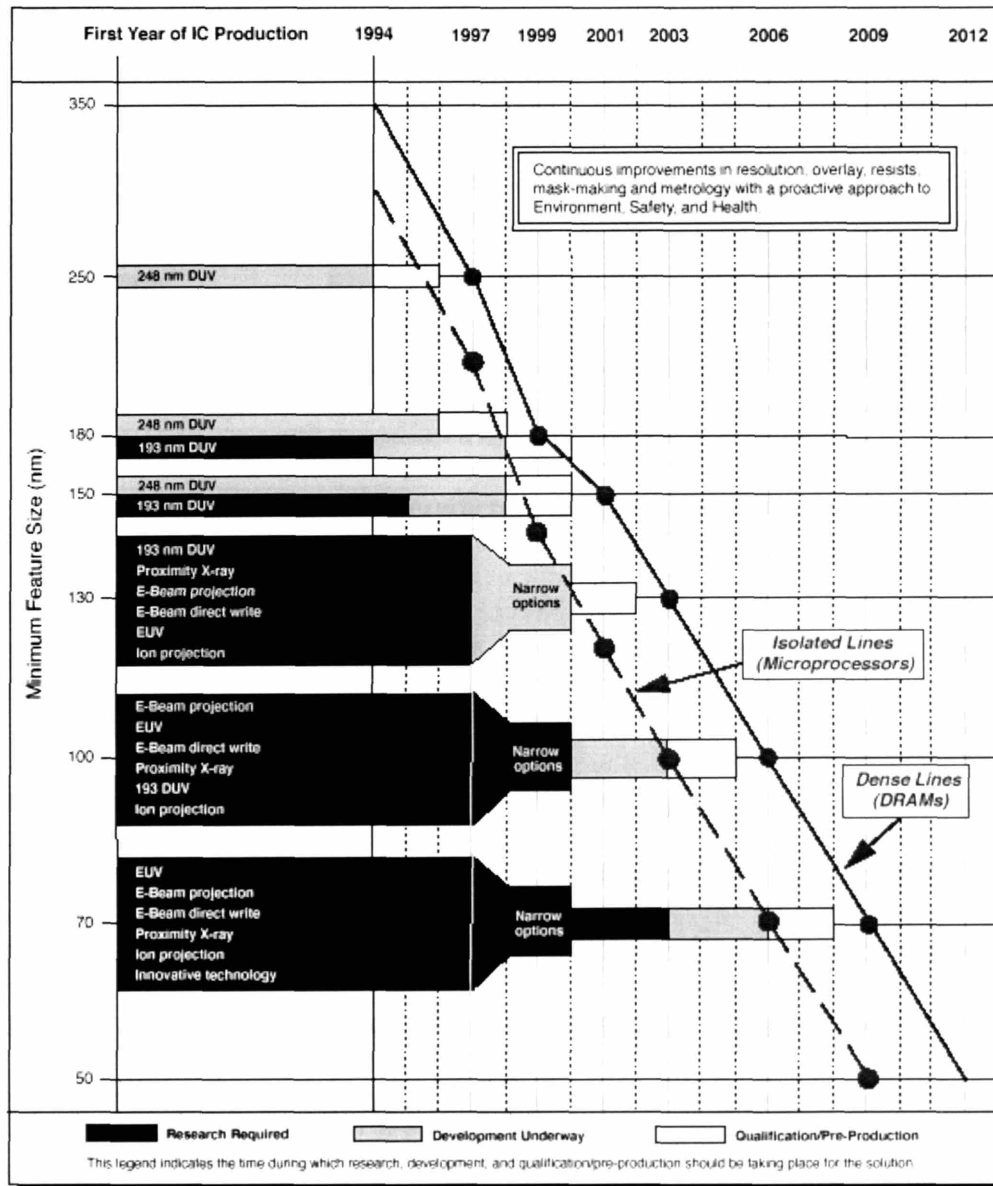

Figure 1-2: National Technology Roadmap for Semiconductors (1997).

The choice of lithography for 100 nm linewidths is not yet settled, but of all the contenders, proximity x-ray lithography is the most mature. It is therefore logical to use x-ray lithography as a test vehicle for an alignment system, as described in this thesis. But regardless of the lithography, the

overlay issue must be addressed. Figure 1-3 illustrates the overlay accuracy required in the near future, as specified in the 1997 NTRS roadmap.

Year of First Product Shipment Technology Generation	1997 250 nm	1999 180 nm	2001 150 nm	2003 130 nm	2006 100 nm	2009 70 nm	2012 50 nm
Gate CD control (nm)	20	14	12	10	7	5	4
Final CD output metrology precision (nm, 3 sigma) *	4	3	2	2	1.4	1	0.8
Overlay control (nm)	85	65	55	45	35	25	20
Overlay output metrology precision (nm, 3 sigma)*	9	7	6	5	4	3	2

Solutions Exist ☐ Solutions Being Pursued ☐ No Known Solution ■

* Measurement tool performance needs to be independent of line shape, line materials, and density of lines

Figure 1-3: NTRS predicted overlay budget (1997).

As we can see, within the next 10 years the overlay control must be at least 25 nm and the 3σ precision must be 3 nm. These are challenging requirements. However, the limits to lithography lie at about 25 nm design rules. It is therefore our goal to invent and implement a robust alignment system that can meet the requirements of all presently foreseeable lithography and provide a metrological tool with sub-nanometer detectivity under a wide range of conditions, in essence, one-nanometer alignment detectivity and placement.

1.3 Obstacles to Nanometer Alignment

If you are still thinking about that example of the sandwich, it may not appear there is much difficulty to alignment. But on the nanometer scale, obstacles to alignment abound. The most obvious problem is that of detection: displacements on this scale cannot be seen using ordinary optical microscopes. The limit of resolution of a microscope is given by

$$P = \frac{\lambda}{2(NA)}$$

where P is the spatial period, λ is the wavelength and NA is the numerical aperture. A high-quality Leitz 100x, 0.8 NA objective can resolve 200 nm features, but this is obviously insufficient for alignment on the order of one nanometer. As is well known, the preferred approach is to use interference of light, allowing an increase of over three orders of magnitude in detectivity over an optical microscope.

But detectivity is only the beginning. As one might imagine, greater sensitivity can imply greater susceptibility to spurious influences. It does no good to have a sensitive alignment scheme if it can be easily corrupted by multitudinous influences. These influences include variations or defects in the alignment marks, thin-film interference effects from translucent coatings on the marks, turbulence in the atmosphere between the marks and the optics,

pointing stability of the illumination and different indices of refraction of gases in the optical path.

Perhaps the most fundamental obstacle is that what appears to be solid and immutable on the macroscopic scale is quite flexible on the nano-scale. Materials flex and bend easily, and generally behave more like rubber than steel. The slightest change in temperature will cause significant expansion or contraction of most materials. For every 0.1 degree C variation in temperature, a 10-cm aluminum stage expands by several tens of nanometers.

A consequence of the flexibility of materials is that the measurement must be made at the position of importance to have much meaning over any period of time. Laser interferometers, for instance, suffer from several of the drawbacks just mentioned: they are currently capable of detectivity below 0.3 nm [1], but are limited by variations in the index-of-refraction of the atmosphere, the flatness of the mirrors, etc. Even if these factors can be taken into account, the fact that the laser interferometers measure the position of the edge of a sample holder means that thermal expansion will introduce disparities between the position of interest on the sample and the position read by the laser interferometer.

The basic message is that position, and therefore alignment, is not a static quality on the nano-scale. Even if objects are positioned with nanometer

accuracy in the first place (which is quite a challenge) they will not remain aligned over time.

1.4 Thesis Outline

The purpose of this thesis is to find a method of detecting the relative position of two objects to better than one nanometer. Equally important, this method should not be susceptible to extraneous influences. Once the metrological problems are addressed, this thesis will describe a method of locking the position of the two objects to within about one nanometer over indefinite periods of time. Chapter 2 will describe the principles of the Interferometric Broadband Imaging alignment scheme. Chapter 3 will respond to the issues of interferometric-fringe spatial-phase analysis. The implementation of IBBI alignment in an in-house, custom-built alignment and exposure system will be described in Chapter 4. Then in Chapter 5 several experiments are related demonstrating the detectivity and robustness of IBBI alignment. Chapter 6 goes on to describe the sub-nanometer consistency found between two microscopes observing the same mark, as well as two different marks during a piezo scan of the mask, and scale consistency found between IBBI and the printing-magnification effect from an x-ray point source. Chapter 7 describes observations of drift and vibration in the alignment system and

makes the case for using feedback to control drift and vibration, even during exposure. With feedback, the alignment stability is shown to be σ = 1.4 nm over six hours. Chapter 8 concludes the thesis and makes suggestions for future improvements.

CHAPTER 2:

INTERFEROMETRIC BROADBAND IMAGING (IBBI) ALIGNMENT

2.1 Past Alignment Approaches

Previous alignment schemes can be divided into two broad categories:

- optical schemes based on imaging geometric objects in a high-magnification microscope, and
- interferometric schemes based on the interference of light diffracted from gratings or zone plates on the mask and wafer.

Interferometric schemes can be further subdivided into those which detect the amplitude and those which detect the phase of an interferometric signal. In this section we will describe examples of, and delineate the strengths and weaknesses of each scheme.

A variety of universities and companies have pursued improved alignment methods applicable to x-ray lithography. In industry the current participants are Suss Advanced Lithography, Silicon Valley Group Lithography in the United States and Canon, NTT, Sumitomo and Toshiba in Japan. The universities having done work in this field are the University of Wisconsin, Louisiana State University, and MIT. The following examples will focus primarily on what has been done in industry, since that is the real-world application, and therefore represents the most wide-spread use of the respective alignment schemes.

Over the years, optical magnification alignment schemes have been the mainstay of the semiconductor industry. Perhaps the most refined example of a geometric imaging optical alignment scheme applied to x-ray lithography is found at Suss Advanced Lithography, a spin-off company of Karl Suss specializing in x-ray steppers. In the SAL aligner, high-magnification, high NA optics image a set of horizontal and vertical bars on the mask, similar to a tic-tac-toe pattern. On the wafer there is a complementary pattern, which creates a set of box patterns when aligned. An image of the box pattern is formed on a CCD camera. The image is analyzed by an edge detection algorithm to determine the spacing between the boxes. Since the basic element of the pattern repeats several times, the spatial period of the pattern can be used for error checking. With this scheme, alignment detection of 3σ = 17 nm has been demonstrated [2]. This approach has the advantage of a long

heritage, many worker-hours of development and experience in a widely installed user base, but has the disadvantages of costly optics and on-axis operation. That is, the microscopes must view the marks at normal-incidence at a millimeter or so from the mask. Since the microscopes block the exposure path, they must be moved out of the way prior to exposure, thus forcing an artificial and undesirable separation between the alignment and exposure operations. This impacts integrated circuit (IC) fabrication in two important ways. First, throughput is compromised by the time taken at every exposure to move the microscopes into and out of the exposure path. In the second way, as device features shrink, the structural stability of the stepper comes into question. Short exposure times achieved with a synchrotron source ameliorate this problem, but the flexibility of materials on the nanometer level demands that greater engineering efforts must be focused on achieving structural stability. The cost/performance curve is not favorable at this level: marked increases in efforts and cost can only achieve minimal gains. One of the arguments developed in this thesis is that a more potent long-term strategy is to pursue closed-loop alignment. This argument is likely to have increasing strength as the transition from global alignment to site-by-site alignment progresses.

An example of interferometric-based alignment is presented by SVGL. This scheme utilizes a linear grating on the mask and a checkerboard grating on the wafer. These marks are illuminated at an angle by a set of lasers of various

wavelengths. The diffracting beams from these gratings are detected at an off-normal angle with a photodetector. By scanning the mask and wafer past each other, a series of amplitude peaks are found. These peaks are contained within an envelope. Alignment is determined by locating the center of this envelope and correlating it with the position of the stage. After the scan, the stage is moved back to the calculated "aligned" position. The published performance data for this method is a 3σ of 40 nm [3]. The advantage of the SVGL scheme is that it can work without blocking the exposure path, but there is a potential problem: alignment cannot be detected without scanning the mask or wafer. It seems counterintuitive to require a movement in order to detect a position. It also makes great demands upon the stages, since they must move back to a predetermined position with nanometer accuracy. Of course, the position of the stages can be sensed with laser interferometers, but the interferometers, however good their detectivity, cannot tell us the truly meaningful information - what the alignment condition is at any point of interest between the mask and wafer. Drift and vibration may occur between the mask and wafer regardless of the quality of the interferometrically controlled stage position. In sum, perhaps the fundamental flaw in this scheme is that it is based on detecting the *amplitude* of an interference signal.

To overcome some of the limitations described above, an alignment scheme called On-Axis Interferometric (OAI) alignment based on a comparison of the spatial phase of two periodic patterns was developed in the 1993 MIT

Ph.D. thesis of Alberto Moel. A grating of period p_1 on a mask was superposed upon a grating of similar period p_2 on a wafer. A CCD camera with a 20x Leitz objective imaged interference fringes under white-light illumination. To determine alignment, the spatial phase of these interference fringes was compared with a fiducial grating of the same period as the fringes, etched into the wafer. Although $3\sigma = 18$ nm alignment in exposed features was demonstrated [4], this scheme suffered from several disadvantages. First, as in the SAL aligner, the microscope was positioned normal to the mask, precluding the possibility of observing alignment during exposure. Second, the fringe contrast was very low due to specular reflections from the mask and wafer. Third, the fiducial grating on the wafer was subject to distortions caused by overlayers. The overlayers, such as photoresist or aluminum, would change the spatial phase of the two patterns in different ways, resulting in spurious alignment signals.

The alignment scheme described in this thesis finds its roots in OAI alignment, but Interferometric Broadband Imaging (IBBI) alignment includes numerous improvements and additions that enhance its potential for future industrial applications.

2.2 Principles of Interferometric Broadband Imaging Alignment

To address the present and future alignment needs of lithography, in particular, proximity x-ray lithography, a novel through-the-mask, site-by-site alignment scheme was invented at the MIT NanoStructures Laboratory. This scheme, termed Interferometric Broadband Imaging (IBBI) alignment, achieves interferometric sensitivity through a comparison of the spatial phase of two periodic interference patterns. Alignment is encoded in the spatial phase discontinuity across the fringes. Figure 2-1 shows several images of fringe patterns with a sequence of spatial phase disparities.

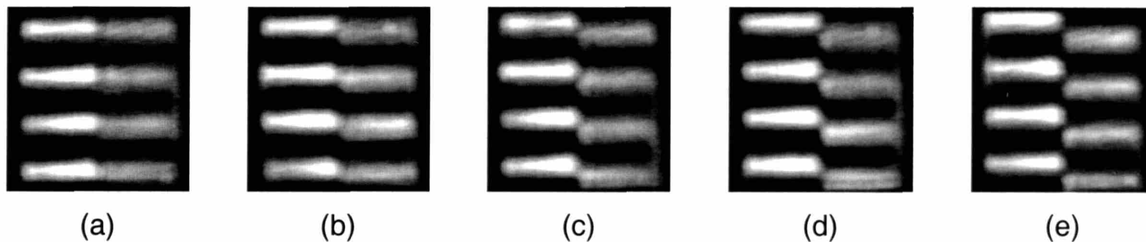

Figure 2-1: IBBI alignment information is contained in the spatial phase of a pair of interference patterns. Images (a)-(e) illustrate spatial phase disparities corresponding to steps of 50 nm.

These interference fringes are created by diffraction of spatially-coherent broadband illumination from complementary gratings on a mask and wafer. The period of the fringes, P, is related to the grating periods p_1 and p_2 by

$$P = \frac{p_1 p_2}{|p_1 - p_2|}.$$

The grating arrangement requires gratings with periods p_1 and p_2 side by side on both mask and wafer, but with period p_1 on the wafer facing period p_2 on the mask (Fig. 2-2), and period p_2 on the wafer facing period p_1 on the mask. In this manner, matched sets of interference fringes are created which move in opposite directions. The counter-motion of the fringe sets further increases (doubles) sensitivity.

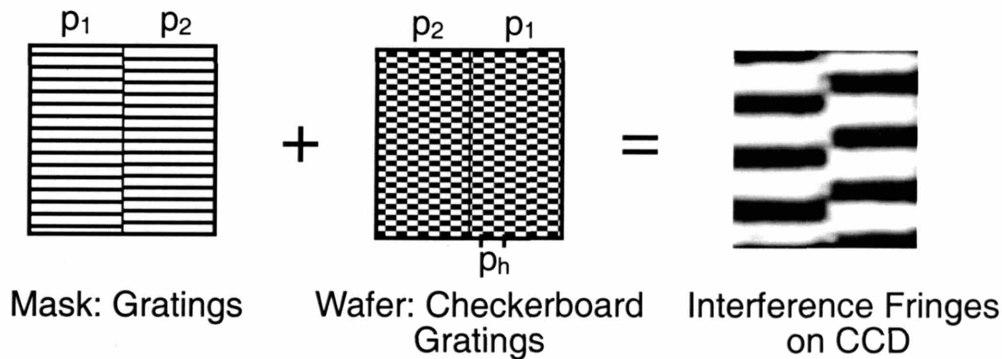

Figure 2-2: Interference fringes are generated by superposition of gratings and checkerboard patterns on the mask and wafer, respectively.

Displacement is magnified in the spatial phase of the interference patterns. Each interference fringe set magnifies the relative displacement of the mask and wafer by the factor M, where

$$M = \frac{1}{2}\frac{p_1 + p_2}{|p_1 - p_2|}.$$

The fringes are imaged by low-NA optics onto a CCD camera (Fig. 2-3). The microscopes operate at a large working distance (110 mm) and are employed for both illumination and imaging (as described in Chapter 4).

Interferometric magnification of displacement allows the use of low-NA microscopes to observe nanometer displacements at a working distance of more than 10 cm, in marked contrast to the working distance of a few millimeters required by high magnification optical microscopes.

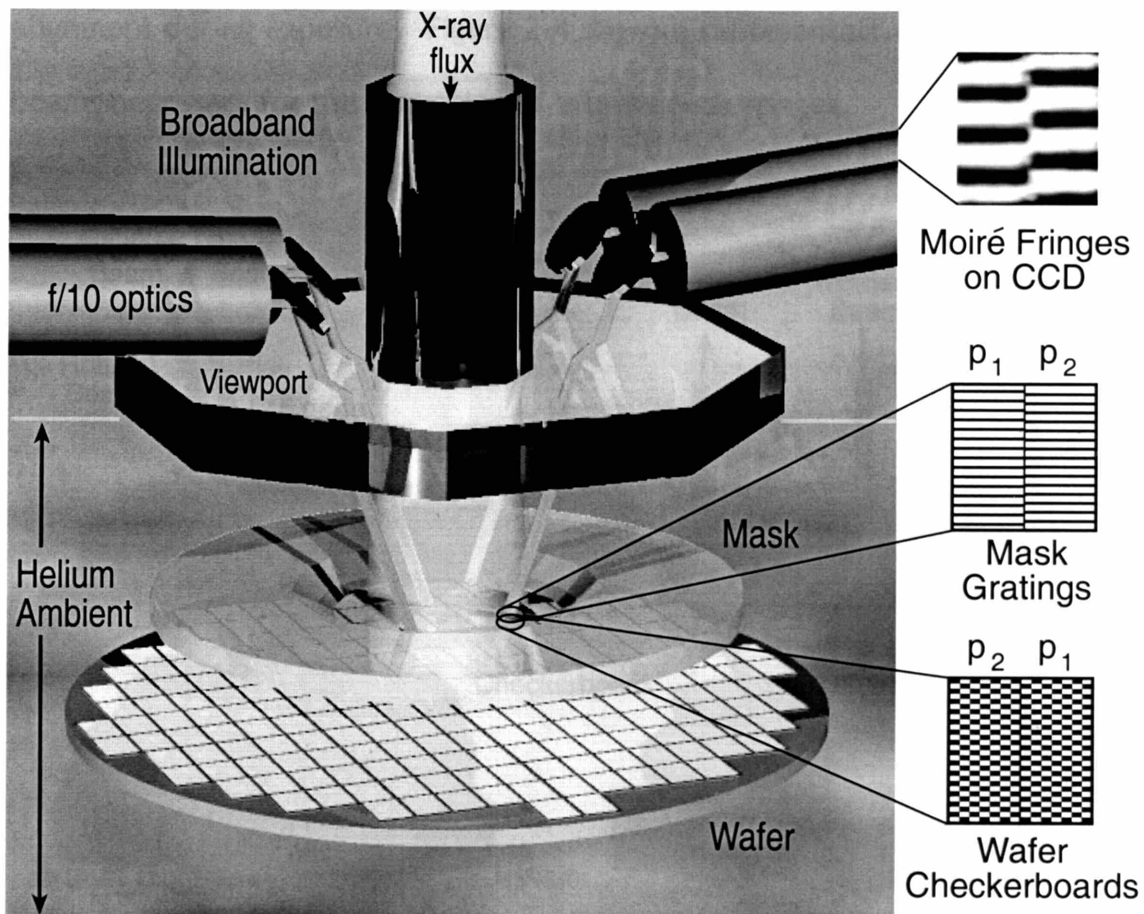

Figure 2-3: Schematic of IBBI alignment. Moiré patterns are formed by superposition of gratings and checkerboards illuminated by broadband light. Checkerboard patterns diffract beams back to microscopes. Alignment is signified by the spatial phase of counter-propagating moiré fringes. Off-axis viewing allows simultaneous x-ray exposure and observation of alignment.

Employing "checkerboard"-type gratings on the wafer causes a "fan" of diffracted beams from the mask gratings to be repeated at several angles[1]. Each fan of diffracted beams lies in a plane corresponding to a different order diffracted from the hatched grating period p_h. Choosing a viewing angle other than the normal to the mask allows off-axis observation without obstruction of the x-ray exposure, thus opening the possibility of feedback-stabilized alignment during exposure. Figure 2-4 shows a representative set of diffracted beams necessary for the formation of interference fringes.

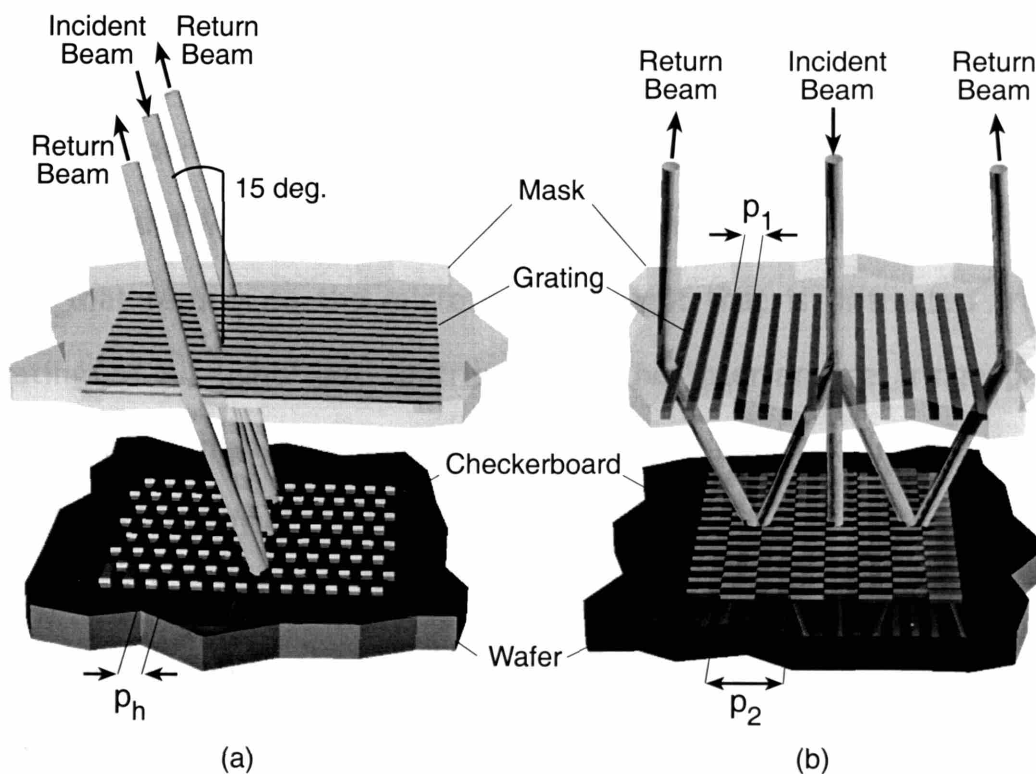

Figure 2-4: Views of diffracted beams relevant to image formation. (a) Beams returned at 15 deg. angle by diffraction from grating hatch p_h. (b) Interference of returning beams creates fringes. Selection of grating periods p_1 and p_2 determine the angle of the returning beams in the plane containing the fan of beams at a 15 deg. angle, and hence the period of the fringes.

[1] Fay, et al. [5] initiated the use of back-diffraction in mask alignment.

For convenience, the viewing and incident illumination angles are chosen to be the same. This is known as a Littrow angle and is given by

$$\theta = \sin^{-1}\left(\frac{\lambda}{2p_h}\right)$$

where λ is the wavelength of the incident illumination and p_h is the hatch period. Typically, the grating hatch period is 1 μm and the Littrow angle is 15 degrees. An additional advantage of the checkerboard gratings is that they eliminate the gap-dependence of the interference fringes. Fringes detected by the CCD are at half the fundamental fringe period, further doubling sensitivity.

By operating at off-normal incidence specularly reflected beams from the mask and wafer are not included in the image. In other words, the only light that returns to the microscopes is light that is diffracted from the gratings, i.e., light that contributes to the interference fringe pattern. Consequently, high contrast and signal-to-noise ratio (SNR) is achieved in the interferometric image.

Furthermore, the robustness of IBBI interference fringes was shown by their insensitivity to the long optical beam path through air, glass, and helium. Since each interference pattern on a CCD is formed along essentially identical optical paths, whatever affects one fringe set will affect the other set to the same degree. For this reason, the relative spatial phase is unaffected by

spurious influences. Experimental evidence of the robustness and detectivity of IBBI will be described in Chapter 5.

2.3 Detectivity

The detectivity of IBBI is determined by the moiré magnification, the doubling of sensitivity from the counter-motion of the fringes, another doubling from the first fringe harmonic, the magnification of the microscope which images the interference fringes onto the CCD camera, the pixel size in the CCD, the number of pixels over which the fringes are imaged, and many details of the algorithm, which will be discussed in the next chapter. The ultimate detectivity of IBBI is predicted to be about 0.1 nm.

To gain an appreciation of the numbers, we will describe a representative scenario. Assume grating periods of 1.00 and 1.02 μm. The resulting fringe period is 51 μm and the corresponding moiré magnification (including counter-motion of the fringes) is a factor of 101. The 1st harmonic fringes will then have a 25.5 μm period. Note that this is within the 7 μm resolution of the microscopes. The length of the grating regions is selected to be 100 μm, hence the image will contain almost 4 fringes. This 100 μm mark

(in the image plane) is magnified by the microscope to 1200 μm (in the plane of the CCD). The pixel size is 6 mm, and there are 200 pixels across the mark.

The detectivity of the CCD is found by calculating the displacement of the mask δx corresponding to a phase disparity of one pixel in the CCD, so

$$\delta x = \frac{(\text{pixel size})}{(\text{Moire mag.})(\text{1st harmonic})(\text{Microscope mag.})} = \frac{6\mu m}{(101)(2)(12)} = 2.5 \text{ nm}$$

The algorithm is capable of sub-pixel detectivity since the fringes are essentially sinusoidal and spread over the size of the mark, or 200 pixels. In this case the detectivity will increase by $\sqrt{200}$, or about 14. Thus the estimated detectivity is 2.5nm/14 = 0.2 nm.

2.5 Capture Range

The spatial phase alignment scheme described above requires that the mask and wafer are pre-aligned to less than a fourth of the grating period in either direction, or typically about 0.25 μm, in order to avoid the problem of phase ambiguity. Such coarse alignment can be achieved in a variety of ways. In its purest form this can be achieved with a set of alignment marks (Fig. 2-5) that consist of four gratings with periods p_1, p_2, p_3, and p_4, and the

{mask/substrate} configurations $\{p_1/p_2\}$, $\{p_2/p_1\}$, $\{p_3/p_4\}$, and $\{p_4/p_3\}$. To eliminate ambiguities at least three out of the four periods must be different. Ideally, the two pairs would yield the same moiré period

$$\frac{p_1 p_2}{|p_1 - p_2|} = \frac{p_3 p_4}{|p_3 - p_4|}$$

in which case, the alignment algorithm could be set for only a single spatial frequency.

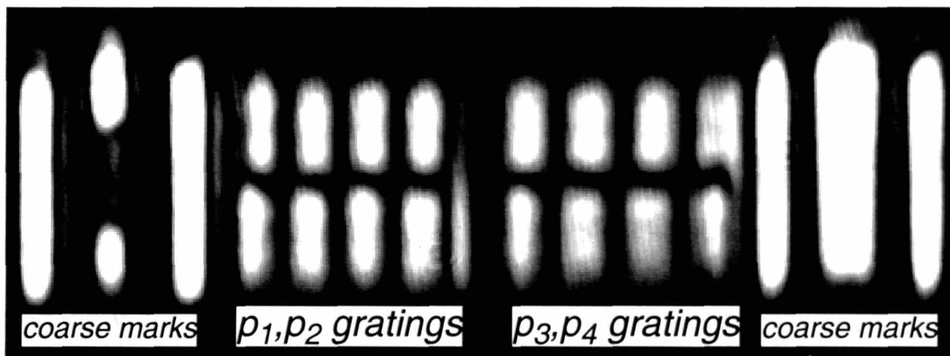

Figure 2-5: Two IBBI marks eliminate phase ambiguity over a range of several microns. Grating periods are designed to yield the same spatial period with slightly different combinations of grating periods. Bar marks on both ends are for aligning in the range of 50> x >1 μm.

Gratings p_1 and p_2 constitute one associated pair, and p_3 and p_4 constitute another; as long as three out of four periods are different, the interference fringes of the two associated pairs will move at different rates as the mask is moved relative to the substrate. All four sets of interference patterns will be in phase only once within a capture range R given by

$$R = \frac{1}{2} \frac{(p_1 + p_2)(p_3 + p_4)}{|(p_1 + p_2) - (p_3 + p_4)|} .$$

By proper choice of p_1, p_2, p_3 and p_4, the capture range can be made reasonably large (~50 μm) so that the mask and substrate can be pre-aligned within it by simple mechanical means. In practice, we find it convenient, but not imperative, to use bar-type alignment marks to indicate misalignment beyond a few microns.

Although having the same period in all four fringe sets may be elegant, it suffers from the disadvantage that a human operator must depend upon a computer analysis to determine the aligned position. The alternative is for the operator to move back and forth over a wide range to attempt to find the position at which all gratings are in phase. In short, the operator has no indication how far off from center he is and perhaps even worse, no way of knowing which direction to go to reach the aligned position. Making a clear distinction between coarse and fine gratings eliminates these problems. With distinctive fringe patterns from each grating set, it is a simple matter to gauge the direction and magnitude of the displacement from the aligned position.

With this in mind, marks with four grating sets were fabricated and tested. Some were tested with the same fringe period in all regions, and others were tested with a variety of coarser fringe periods and grating periods. The purpose of testing coarser periods is that the fringes will move a smaller distance than will the finer periods during the same displacement. This makes it extremely obvious to an observer when both the coarse and fine fringes are

in registry. As seen in Figure 2-6 it is easy to discern the coarse from the fine fringes, and the alignment of the fine fringes can be checked against the alignment of the coarse fringe and bar marks to ascertain if true alignment has been achieved.

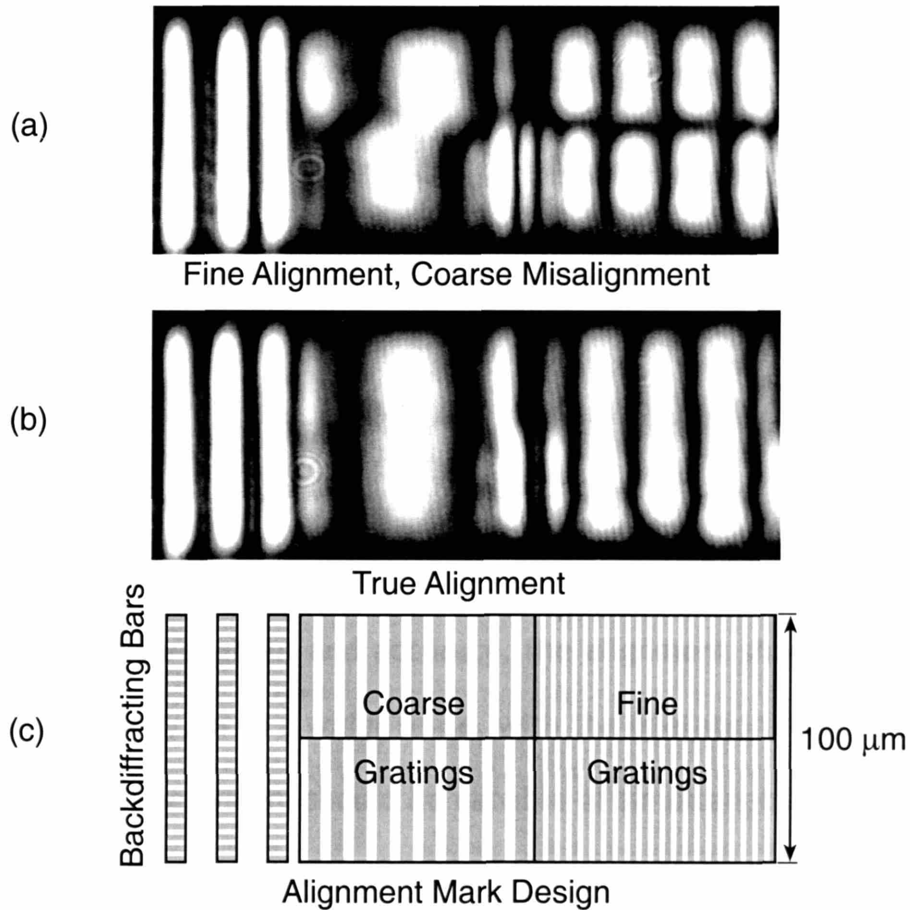

Figure 2-6: (a) Fine fringe alignment, coarse fringe and bar misalignment. (b) Alignment of all fringes and bars at a unique position. (c) Schematic of coarse/fine alignment marks.

The capture range with these marks is as wide as the spacing between the bar marks. This particular mark design allows quick convergence from 50 μm to

the aligned position. These fine and coarse marks are equally amenable to automated alignment, as will be discussed in the following chapter.

2.5 Summary of Design Criteria

From experience with the alignment schemes discussed previously, as well as many others, we can deduce several essential characteristics, which we believe any successful nano-alignment scheme should include:

1) The alignment should incorporate interferometric sensitivity.

2) For maximum throughput and accuracy, the alignment should not interfere with the lithography, or in a wider sense, with the operation of any part of the alignment tool. The system should be capable of simultaneous alignment, gap control and exposure. This is necessary for high throughput, high overlay accuracy, or long exposure time. The system should correct for background vibrations, mechanical drift, exposure-induced distortions, and increase accuracy by performing statistical averaging of many alignment operations.

3) The system should utilize optics with low NA to reduce alignment errors induced by the aberration and misalignment of the optical system. Low NA

optics allow a long working-distance, and also reduce cost, weight and complexity.

4) The alignment signal should not be corrupted by its environment. As we know from experience listening to AM radio, signal amplitude is easily affected by the interaction of the signal and its environment. Phase detection (such as that in FM radio) yields clean signals even in the presence of amplitude-distorting influences. This is important in alignment due to the need to accurately view wafer alignment marks even when covered by process coatings. This is an essential requirement, since every lithography step may require a different coating. The alignment signal also should not vary with the type or thickness of the overlayer.

5) The alignment signal requires high signal-to-noise ratio (SNR). As we have seen, the IBBI alignment signal contains spatial phase information directed to the IBBI sensors, and ignores scattered light, thereby achieving high SNR.

6) Imaging is intrinsically about spatial information, hence it is advantageous to use it for alignment. In addition there is redundant information in an image. An image contains 2-dimensional information, as opposed to a time-domain signal, which is inherently 1-dimensional.

7) The imaging information should be informative to a human user and not necessarily require computer analysis to be used for alignment, although the finest alignment must be performed automatically.

8) A short response time is desirable for the alignment signal. Wafer throughput in industry is between 40-60 wafers per hour. This throughput can be achieved using global alignment, which sets alignment at the beginning of a wafer exposure and relies upon the stages to step between dies and maintain alignment for each exposure. In site-by-site alignment, each die is aligned immediately prior to exposure. To achieve the necessary throughput with site-by-site alignment, it is important for alignment to take less than one second.

As we have begun to show in this chapter, this thesis will illustrate how IBBI incorporates all of the above features, as well as other beneficial qualities.

CHAPTER 3:

IMAGE ANALYSIS

3.1 Spatial Phase Detection

The essential goal of the image analysis is to determine the spatial phase discontinuity between one or more matched pairs of interference fringes. In this section we describe the procedure for the case of a simple pair of fringe sets, and then in Section 3.4, the variations required for a wide capture range.

An image is transferred from a CCD to a framegrabber and from there to computer memory. Two regions of interest (ROI) corresponding to each set of fringes are determined by the operator, and extracted from the image (Fig. 3-1). The sample length L is equal to the length of the region extracted from the image. The width W is selected to avoid overlapping fringes near the interface of the fringe sets. Assuming that there is no azimuthal angle between the

mask and wafer, and that the camera pixel rows are aligned to the fringes, the situation is rather straightforward:

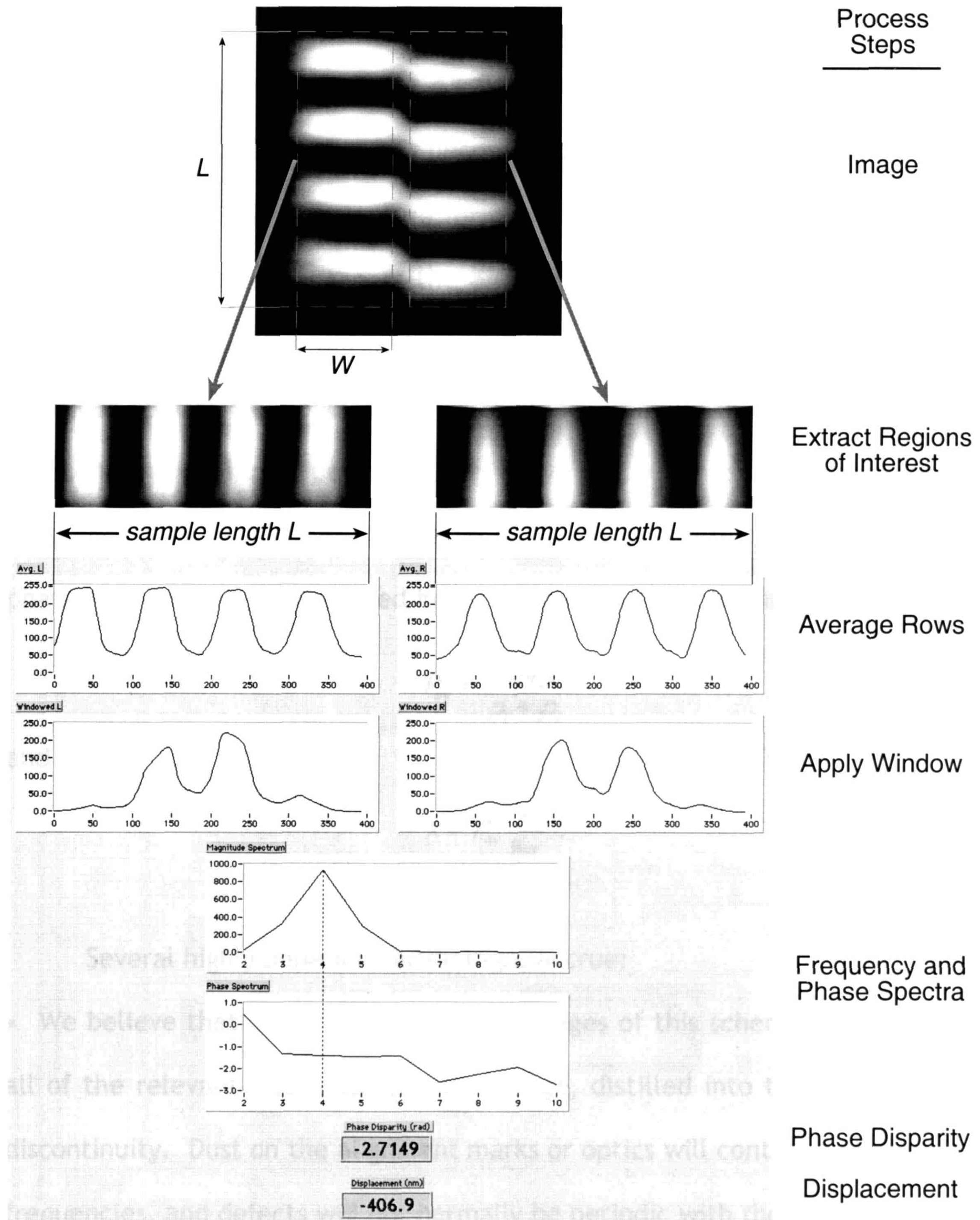

Figure 3-1: Steps in the phase detection algorithm with fringes aligned to CCD pixel rows and no angular misalignment between mask and wafer.

First, the pixels in every row parallel to the fringes are averaged. If the sample length L is not an integer multiple of the period of the interference fringes P, then a frequency-domain analysis gives an erroneous value for the displacement x, unless the phase $\phi = 0$. In order to extract an accurate value of x for arbitrary values of ϕ it is necessary to eliminate the frequency-domain artifact. The standard procedure for doing so is to apply a "window" to the sample, which smoothly tapers the ends of the sample to zero. In this way there are no sharp discontinuities at the ends of the sample to introduce fictitious spatial frequencies. The frequency-domain analysis then outputs frequency and phase spectra. The value of the phase spectrum at the frequency peak determines the spatial phase discontinuity of the fringes. The phase measurement is converted into a displacement according to the formulas

$$P_{av} = \frac{2p_1p_2}{p_1 + p_2}$$

and

$$x = P_{av}\frac{\phi}{8\pi} \ .$$

Several highly beneficial advantages accrue:

- We believe that one of the major advantages of this scheme is that it uses all of the relevant information in the image, distilled into the spatial phase discontinuity. Dust on the alignment marks or optics will contain higher spatial frequencies, and defects will not normally be periodic with the same frequency as the fringes. Since a single, predictable spatial frequency is selected when picking out the spatial phase difference this excludes contributions of every

other, spurious spatial frequency. This is believed to be more robust than an edge-detecting approach used in many alignment schemes since all pixels of the image contribute to the measurement, not just those in the vicinity of edges.

- The algorithm can be used effectively for both coarse and fine alignment.
- The algorithm is relatively simple to implement and code, and in fact can be coded using a few off-the-shelf software components. LabVIEW [6] code is shown in Fig. 3-2.

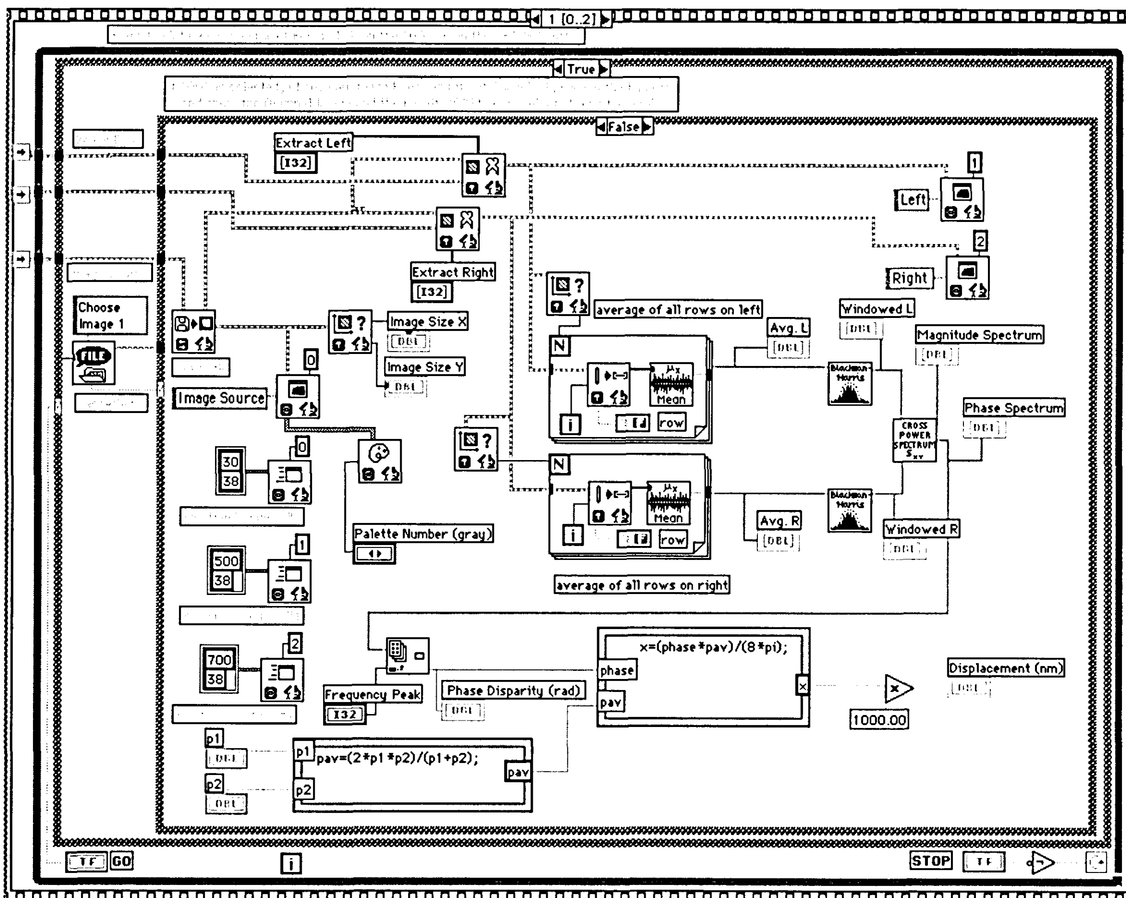

Figure 3-2: LabVIEW spatial phase detection algorithm.

3.2 Non-Integer Fringes

It will be instructive to take a closer look at the issues presented by a non-integer number of fringes within the sample length. Without windowing the input sample, errors will arise in two situations: during variations in the sample length, and in the position of the fringes within the sample.

To examine the effect of the number of fringes within a sample, the difference between a simulation of detected and actual phase is plotted in Fig. 3-3, with and without windowing. In the case without windowing, periodic phase errors are evident, amounting to ~0.1 radian. For gratings periods p_1 = 1.00 μm and p_2 = 1.02 μm this corresponds to an error of 4 nm.

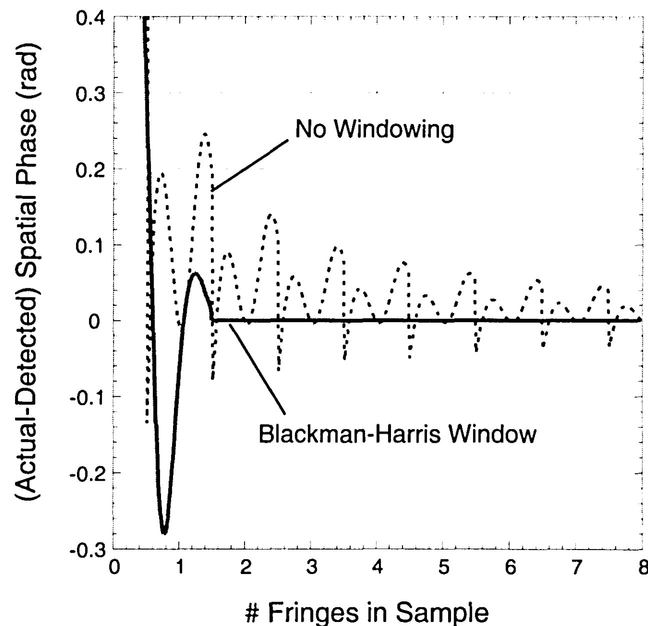

Figure 3-3: Simulated disparity between actual and detected phase as a function of the number of fringes in the sample, with and without a window.

In contrast, when windowing is employed the phase measurement error is zero (within 1 milliradian) for more than 1.5 fringes in the sample. This corresponds to an error of less than 0.1 nm. We consider this an indication that the algorithm that determines alignment is capable of true sub-pixel resolution.

Now consider the position of the fringes relative to the extracted regions of the image. The positions of the ROI are specified initially by the user, and remain the same thereafter. Thus we expect an error, if any, to be systematic: non-windowed measurements will be precise, but not necessarily accurate. Figure 3-4 shows the simulated variation in the detected alignment when the two ROI are shifted in parallel, in a direction perpendicular to the fringes.

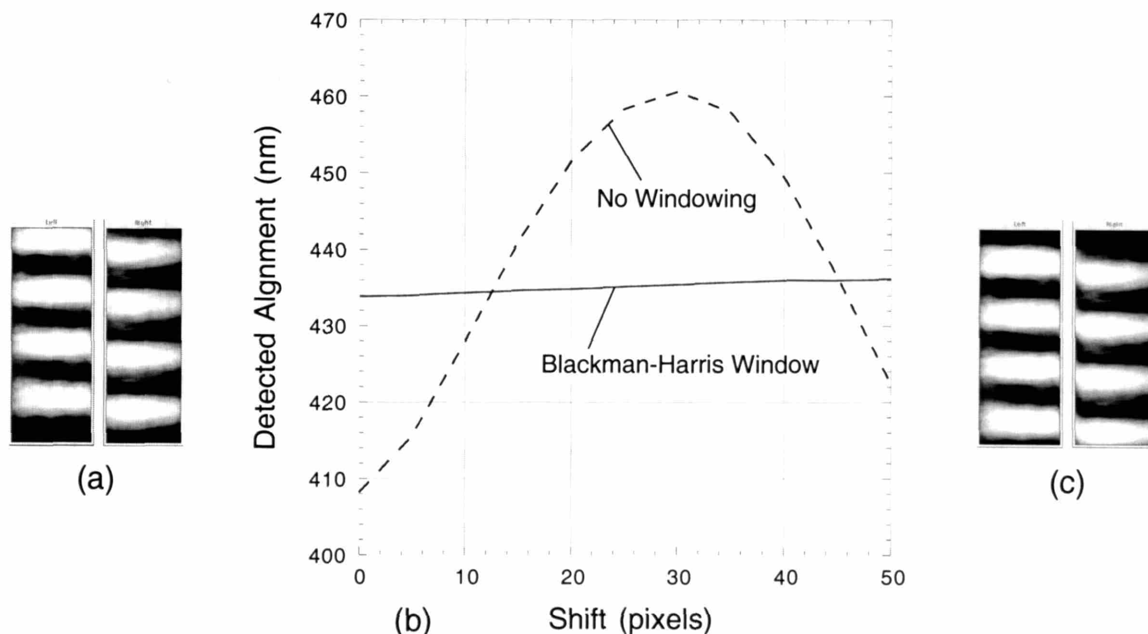

Figure 3-4: (a,c) Images of the same fringe pattern with the ROI shifted by 40 pixels. (b) Simulated errors in detected alignment due to the position of fringes with sample regions of constant length shifted in a direction perpendicular to the fringes. The error is periodic and can be >50 nm. Windowing reduces the error to <2 nm.

If windowing is omitted, systematic errors of more than 50 nm may result. Using a Blackman-Harris window reduces the possible error to less than 2 nm. Experience with a variety of other windows suggests that this error can be reduced to <1 nm with optimization of windowing parameters.

3.3 Mask-Wafer and Camera Angle

Two important parameters are the azimuthal mask-wafer angle and the camera-fringe angle, either of which will distort the alignment measurement if only one ROI is used for each fringe set, as in Section 3.1. In the general case, a finer-grained analysis is required. Figure 3-5(a) shows eight ROI of width *W* within one fringe set. The phase-detection algorithm described in Section 3.1 is applied between pairs of these small regions. For example, starting at the leftmost ROI we find the phase between the first and second regions, then between the first and third, and so on across the fringe set. This procedure yields a series of phase measurements from which we can find the *phase slope*. Continuing to the other side of the mark, the phase slope of the complementary fringe set is determined in a like manner. If the two fringe sets are found to have an equal slope, then we can conclude that they are due entirely to the angle between the fringes and the pixels of the CCD camera.

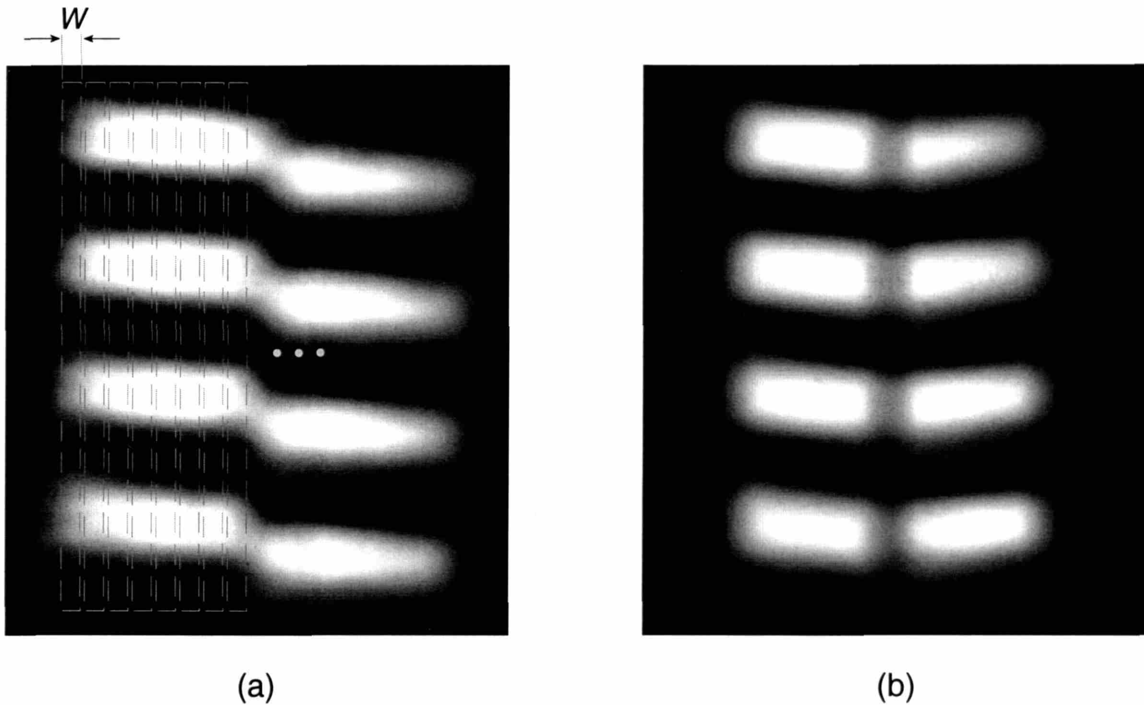

Figure 3-5: (a) Image of fringes at an angle with respect to the CCD camera. (b) Chevron pattern resulting from mask-plane angle between mask and wafer.

Alternately, Fig. 3-5(b) shows fringes with equal angles, but opposite signs - what we call a "chevron" fringe pattern, indicating an in-plane rotation between the mask and wafer. This angle can be eliminated by alignment at two widely separated marks.

In general, we take the difference in phase slopes from the two fringe sets to remove the contribution from the azimuthal mask-wafer angle and reveal the remaining angle due to the camera. The camera slope can be removed in software, or by adjusting the angle of the camera in its mount.

3.4 Wide Acquisition Alignment

The algorithm described here follows a three-tiered approach (Fig. 3-6) to achieve a wide acquisition range - the three regions of the alignment mark shown in Section 2.4 are analyzed from coarsest to finest resolution.

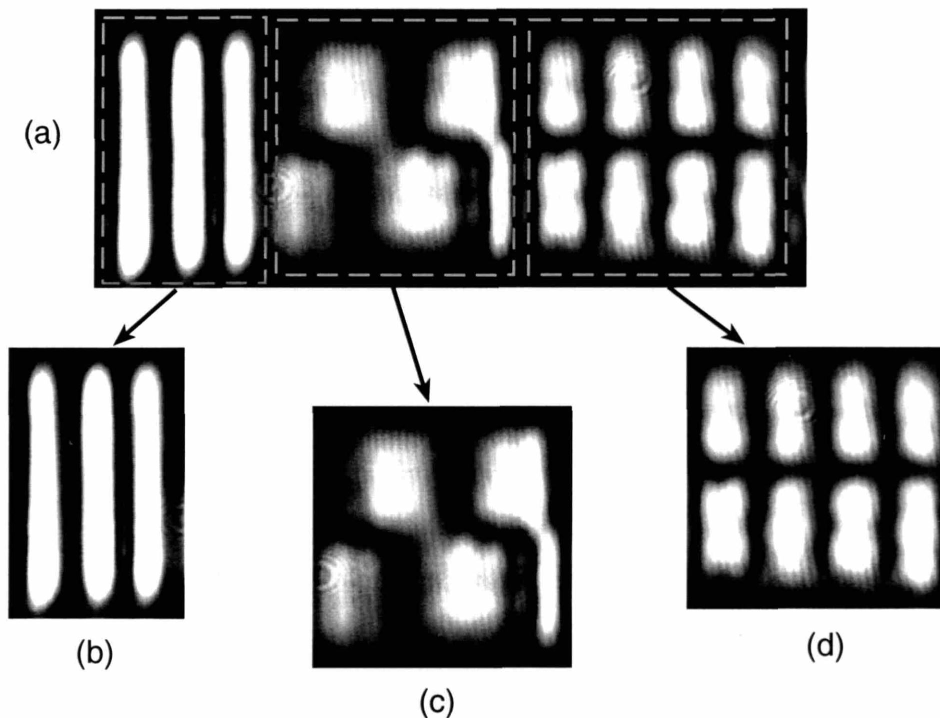

Figure 3-6: (a) Image of wide acquisition range marks. (b) Bar marks. (c) Coarse moiré marks. (d) Fine moiré marks.

Starting with the bar marks, Fig. 3-6(b), we note that alignment is indicated by the position of the center bar between the bars on both ends. An algorithm takes a slice of the mark perpendicular to the bars, fits a gaussian to each peak to find the best-fit center, and takes the difference between the interstitial spaces to determine alignment (Fig. 3-7a). With the bar marks the

acquisition range is as wide as the spacing between the outermost bars (several tens of microns) and the resolution is about 0.5 μm. Figure 3-7(b) shows a plot of the alignment repeatability for several hundred iterations of the alignment algorithm. Note that the variation in detected alignment did not exceed 0.5 μm.

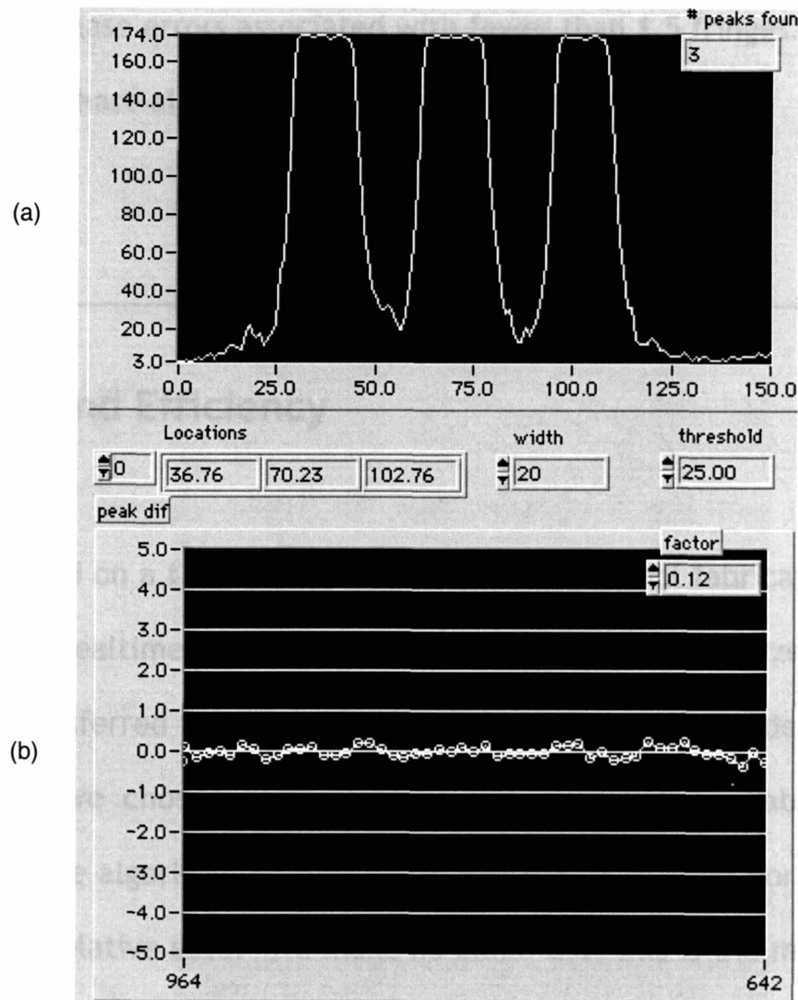

Figure 3-7: (a) Intensity distribution of a slice through a bar-mark image. The units of the vertical axis are pixel intensity (8-bit digitization). (b) Plot of the repeatability of 300 coarse alignment measurements. The units of the vertical axis are microns.

Within the 1-μm range we examine the coarse moiré mark. Depending upon the number of fringes in the mark, we use either spatial phase detection or a correlation of the position of peaks, akin to the bar mark algorithm. A comparison of the peaks from two fringes, such as those shown in Fig. 3-7(b), in conjunction with a calibration of the pixel size, gives a resolution better than 0.1 μm. The boundary between the phase and peak-detecting regimes is defined by the phase errors associated with fewer than 1.5 fringes. In the final stage, a spatial phase algorithm analyzes the fine moiré fringes.

3.5 Speed and Efficiency

To use IBBI on a true site-by-site basis for industrial fabrication, it must be capable of "realtime" operation, i.e., the images are analyzed as fast as they can be transferred from the CCD (1/30 sec). However, for developmental purposes we have chosen to implement the algorithm in LabVIEW. The complexity of the algorithm is sufficiently low that it may be ported to other platforms with relative ease. We make no claim that this is the most efficient implementation of the algorithm, only that it is supremely flexible and acceptably fast for our present laboratory needs. On a 300 MHz G3 processor, the time required for the image transfer and execution of the algorithm is about 400 ms. Once the image is digitized by the framegrabber, the transfer of

the image data to the main computer memory over a 46 MHz computer bus represents a significant fraction of the latency time. A commercially available dedicated DSP processor [7] with on-board framegrabbers is expected to be capable of analyzing the images in realtime.

CHAPTER 4:

ALIGNMENT AND X-RAY EXPOSURE SYSTEM

4.1 System Architecture

A custom alignment and x-ray exposure system (Fig. 4-1) was designed and constructed in the MIT NanoStructures Laboratory for the purposes of exploring and developing IBBI alignment. As discussed in Chapter 2, a predecessor alignment scheme to IBBI, called On-Axis Interferometric (OAI) alignment matched the spatial phase of an interference pattern to a set of fiducial marks etched into a wafer. Although the OAI scheme was demonstrated to be sensitive to better than 10 nm, one of the primary constraints of the system was the inability to observe alignment during exposure. This was exacerbated by the fact that the mask/wafer stage assembly was rolled on tracks between the alignment and exposure positions. Mechanical disturbances encountered in moving the stages between alignment

and exposure positions often made good alignment irrelevant. In the present alignment system, care was taken in the system design to permit alignment at *any* time – before and during exposure.

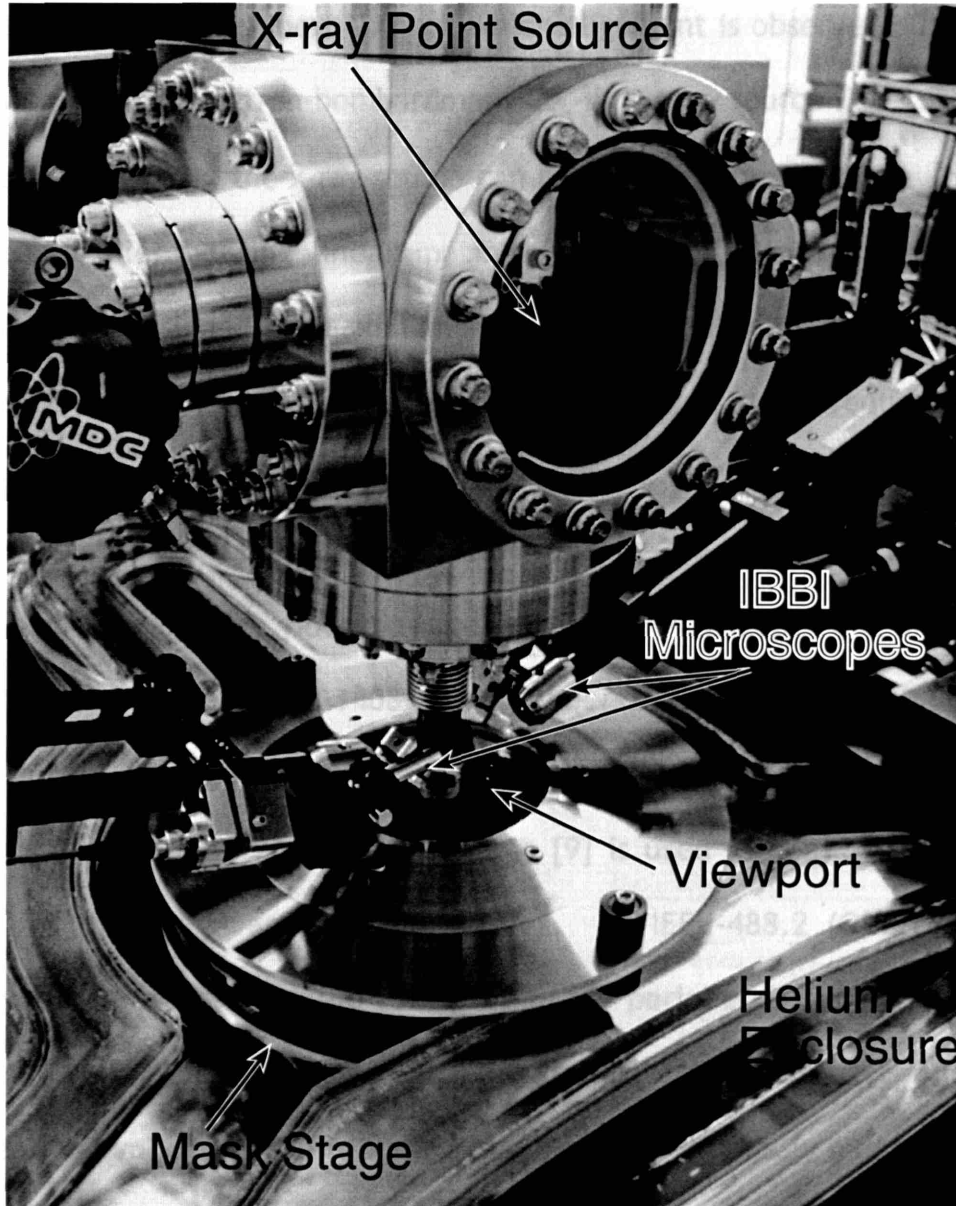

Figure 4-1: IBBI alignment and exposure system.

Figure 4-2 is a schematic of the alignment/exposure system, which we refer to as Head 4[1]. This system consists of a wafer stage capable of positioning Si wafers up to 8" diameter in X, Y and θ, a 6-axis mask stage utilizing closed-loop piezos for mask translation and DC servos for angle and gap control, three IBBI microscopes (necessary to measure alignment in X, Y and θ), a helium enclosure containing a viewport through which alignment is observed during x-ray exposure, and an electron-bombardment Cu_L-line x-ray source (λ = 1.3 nm). When loading the mask, the x-ray source can be raised or moved laterally by a pair of cross-roller bearing linear motion stages [8]. The stainless-steel superstructure is designed for maximum symmetry to ameliorate the effects of thermal expansion, and to provide a structure with high resonant frequency.

An Apple Power Macintosh 9500/G3 running at 300 MHz controls the set of servos and piezos. The video streams from the microscopes are digitized using National Instruments PCI-1408 framegrabbers. LabVIEW 4.1 software is used for image acquisition, analysis, stage control, and exposure control. A third-party image analysis software package [9] is used in conjunction with LabVIEW for the image analysis subroutines. An IEEE-488.2 (GPIB) board completes the interface from the computer to the peripheral stage and piezo controllers. During the x-ray run critical parameters such as the oxygen level, and current and voltage of the HV power supply are continuously monitored by

[1] Head 4 is the fourth in a series of x-ray sources constructed in the NanoStructures Laboratory.

the computer through an analog/digital I/O board [10]. Solenoids controlling water and helium flow are also controlled through this board.

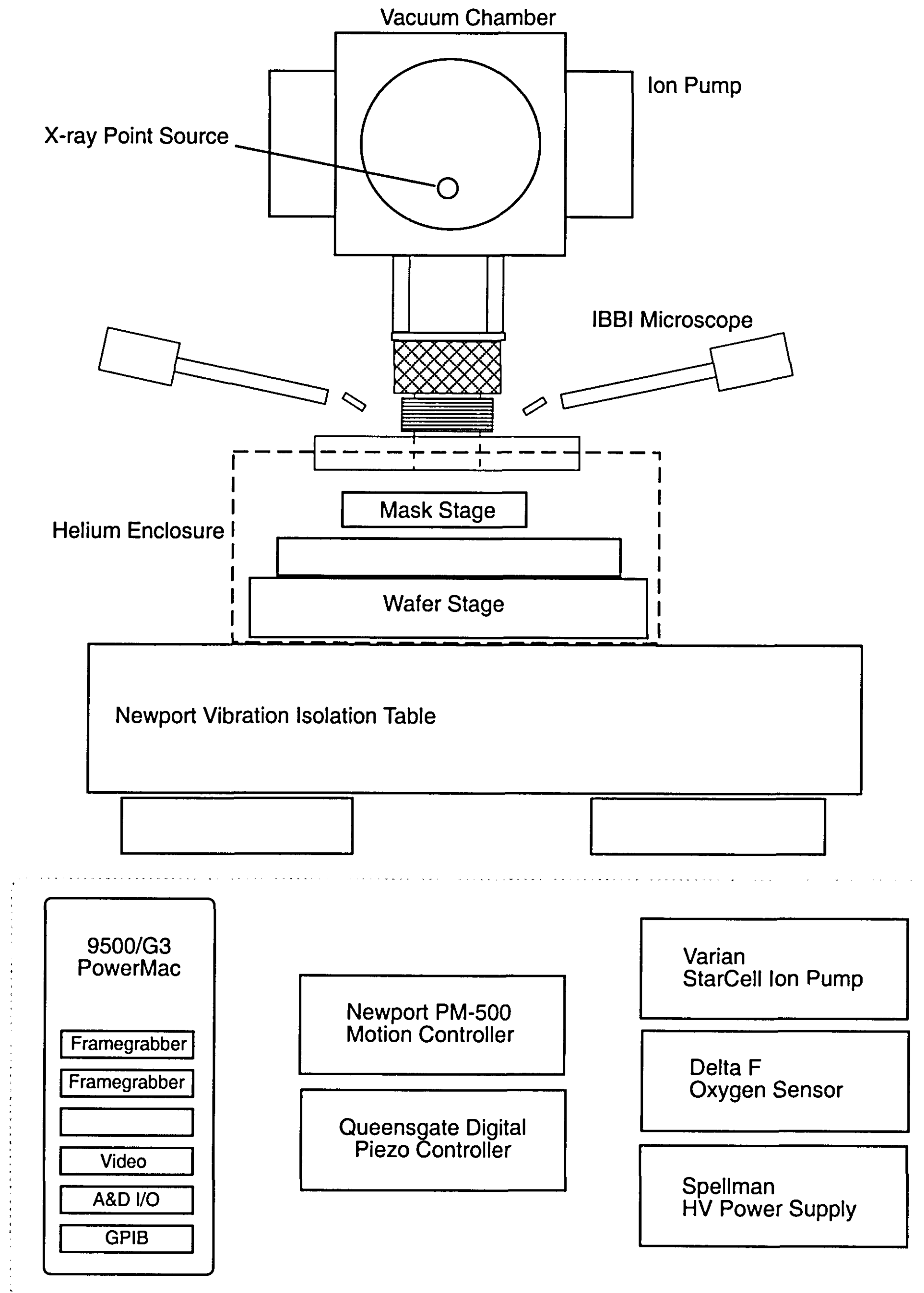

Figure 4-2: Schematic of alignment/exposure system. The multitudinous connections between the components are not shown for clarity.

The operation of the system is as follows: Prior to an exposure the mask is loaded with the x-ray source in the raised position and the top of the helium enclosure removed. The front of the helium enclosure is removed to allow the wafer stage to slide out from underneath the mask stage. After the mask and wafer are loaded, the x-ray source is lowered into position, the helium enclosure is sealed, and the IBBI microscopes are brought to their observation positions. Alignment is performed with all components in place. The path between the mask and source may be purged with helium either before or after alignment. At this point the exposure is initiated. Alignment is monitored throughout the exposure, and small corrections made as necessary. The system assumes an x-ray source that operates vertically, although the basic principles of the system can be adapted to a source which operates horizontally, e.g., a synchrotron.

4.2 X-ray Source

We choose to use x-ray lithography as the test vehicle for IBBI alignment since it has many advantages over competing exposure schemes, such as absence of spurious scattering, large process latitude, good resolution, and high throughput. Due to its history, numerous advantages, and research successes, it is not an exaggeration to say that it is the leading contender for

the dominant semiconductor manufacturing technology in coming generations. One of the primary reasons for this is that x-rays have the unique property that spurious scattering is negligible, due to the fact that the real part of the index of refraction is very close to unity for all materials. In contrast, ultraviolet (UV) photons undergo significant scattering, as do ions near the ends of their trajectories. Such spurious scattering causes exposure in regions where it is not wanted, so-called proximity effects. Absorption without spurious scattering is certainly one of the main reasons for pursuing x-ray lithography, especially for nanolithography.

In the NanoStructures Laboratory we use a low-cost electron bombardment x-ray source with a copper L-line wavelength (λ=1.3 nm). Figure 4-3 shows the pertinent parts of this source.

A tungsten filament is held at 8 kV below the potential of a grounded copper anode. A current is pulled off the filament and the electron trajectories follow paths from the circumferential filament towards the center of the copper target. Focusing is achieved by sliding the assembly holding the filament along its axis.

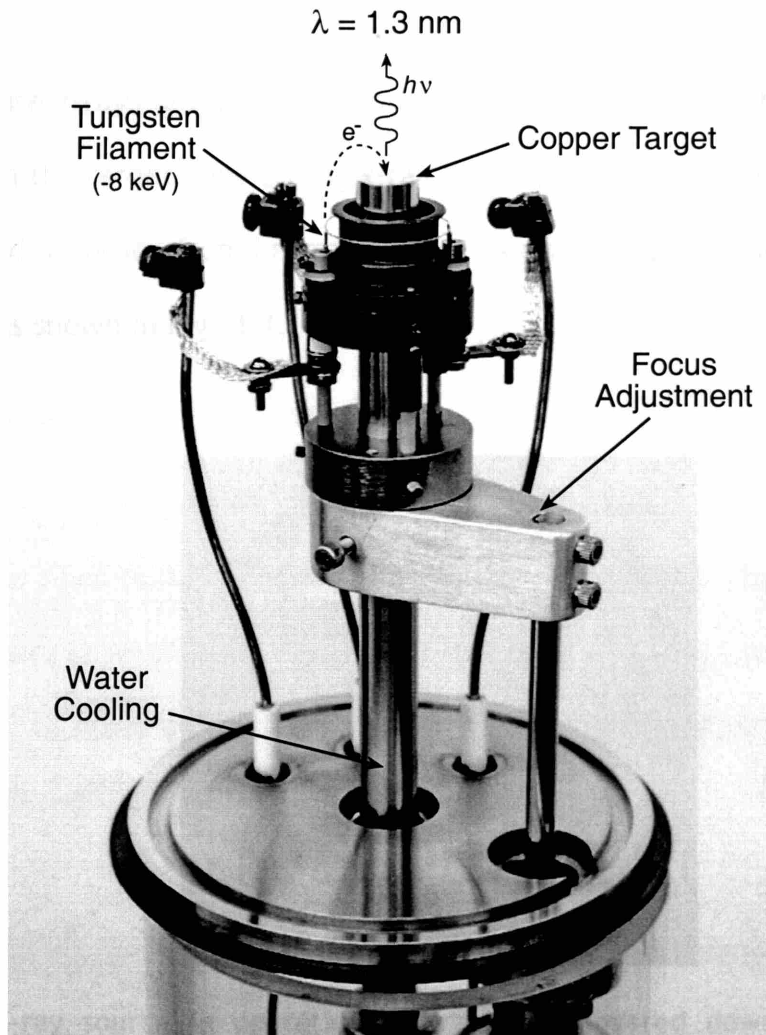

Figure 4-3: Photograph of an electron-bombardment x-ray source. A tungsten filament is held at 8 keV below a copper anode. Electrons pulled off the filament impinge on the center of the copper target. Moving the filament relative to the anode focuses the electrons. The Cu_L-line has a wavelength of 1.3 nm.

The entire assembly is held in vacuum, typically at about 10^{-7} Torr. X-rays traverse the distance to the mask (250 mm) through regions of vacuum and atmospheric-pressure helium, separated by a 1.6 μm-thick silicon nitride vacuum window held on a polished o-ring mounting in the bottom of the vacuum chamber. The diameter of the vacuum window is 20 mm.

Once the electrons impinge upon the copper target they undergo collisions which generate x-rays and many secondary effects, such as heat and electron emission from the target. One strong x-ray line is produced at 1.3 nm and there is background radiation from bremstrahlung. A photograph of the x-ray source in operation is shown in Fig. 4-4.

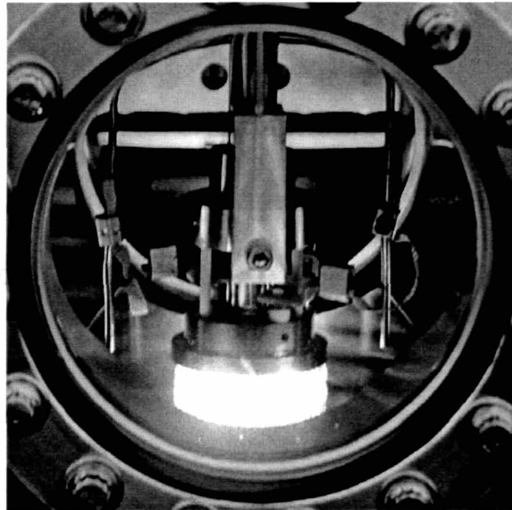

Figure 4-4: X-ray source in operation. X-rays are emitted downward into 4π steradians.

The probability that x-ray emission will occur rather than an Auger electron being ejected is called the fluorescent yield of the material. For the Cu_L line the fluorescent yield is only 0.006. This means that the copper target is not very efficient at generating x-rays. Given the inefficiency and consequent long exposure times of an electron-bombardment source, one may wonder why we use it. For the relatively modest requirements of a university laboratory, the x-ray flux from a Cu_L source is adequate. Furthermore, it is

compact and relatively inexpensive. When high throughput is a necessity, as in industrial production, synchrotrons or other sources can be substituted.

4.3 Nano-positioning Stages

To take advantage of the powerful combination of IBBI alignment and x-ray lithography, several requirements based on the needs of the lithography must be met. In order to understand these needs, we will briefly describe the principles involved.

In proximity x-ray lithography a mask is held at a microgap to a wafer coated with resist, as shown in Fig. 4-5. This mask has an absorber pattern that is a high-Z material, such as gold or tungsten. The 200-nm thickness of the absorber is designed to give a 10-dB attenuation. The mask-wafer gap determines the minimum feature size for a given wavelength of illumination. Linewidth consistency demands that the gap is consistent over the entire mask - thus, mask flatness is critical.

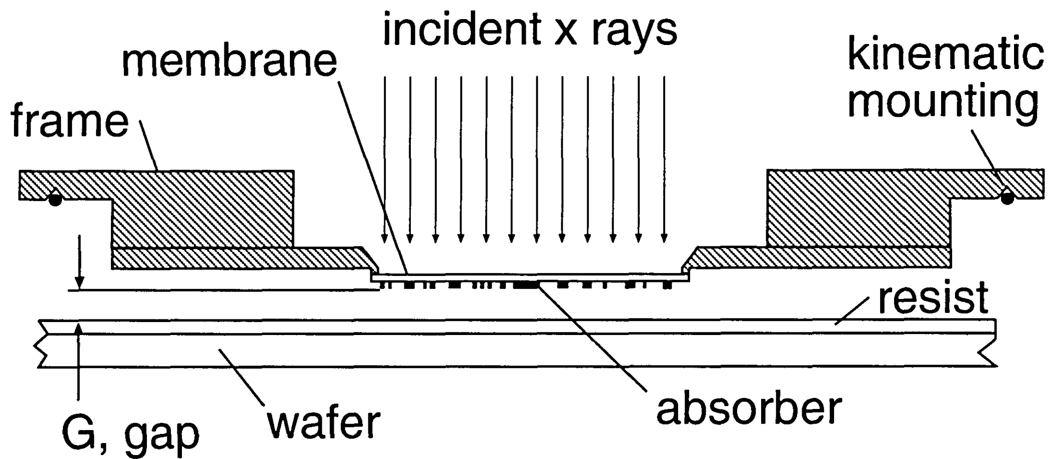

Figure 4-5: Schematic of mask and wafer. Photosenstive resist is patterned by exposure with x-rays following selective patterning by mask. Due to diffraction limitations, the gap G determines the finest possible printed feature.

Diffraction in the gap between the mask and wafer is the only important consideration in evaluating resolution since the effective range of Auger electrons is only about 5 nm. The relationship between gap, G, and the minimum printable feature size is given approximately by

$$G = \frac{\alpha (W_{\min})^2}{\lambda}$$

where α is a scaling parameter (the reciprocal of the square of so-called Fresnel number), W_{min} is the minimum linewidth, and λ is the source wavelength. Analysis and experiment show that α values of 1 are permissible for high quality pattern replication, and values of 1.5 yield good process latitude [11].

Figure 4-6 illustrates a plot of the maximum allowable mask-wafer gap as a function of the minimum linewidth for a wavelength of 1.3 nm and $\alpha = 1$, 1.5, and 3 respectively.

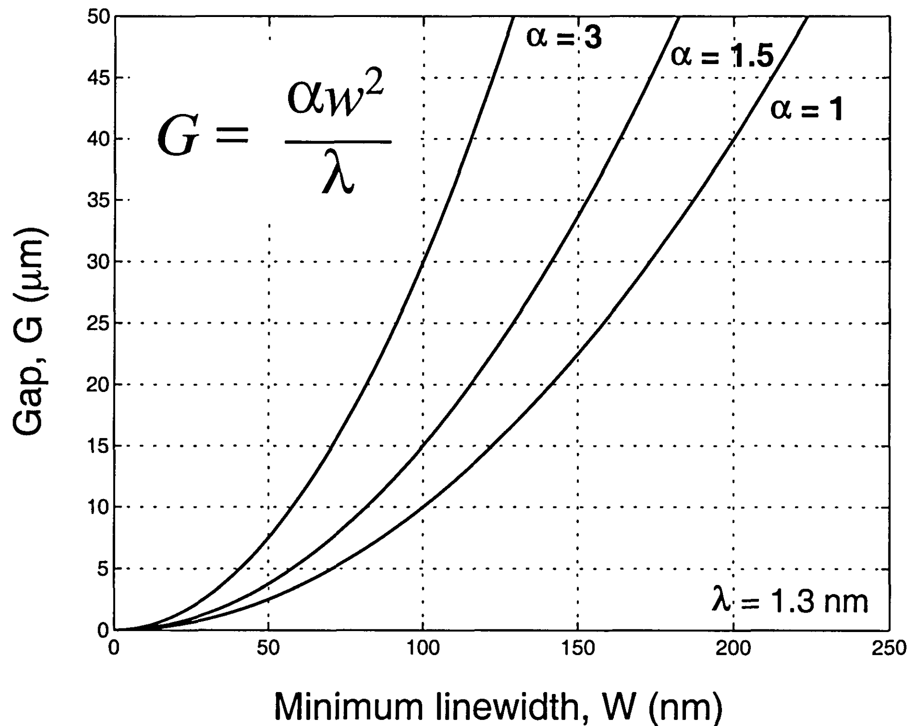

Figure 4-6: Plot of the maximum allowable mask-wafer gap as a function of the minimum linewidth for a source wavelength of 1.3 nm and α = 1, 1.5 and 3, respectively.

As we can see from Fig. 4-6, for sub-50 nm features, the maximum allowable gap is <10 μm. At this gap of a few microns, physical contact between the mask and the wafer is possible, but should be avoided to preclude damage to the mask or wafer. However, 3 μm gaps are achieved routinely on a laboratory bench in a Class 10 cleanroom in the NanoStructures Laboratory, although the mask motion is constrained by hydrodynamic effects [12] at gaps below 10-15 μm.

The resolution limit of x-ray lithography[2] can be reduced to the question of what is the smallest practical mask-wafer gap. Two requirements are apparent: the mask and wafer must be optically flat, and no dust or particles can be allowed on either surface, or else they will distort the gap.

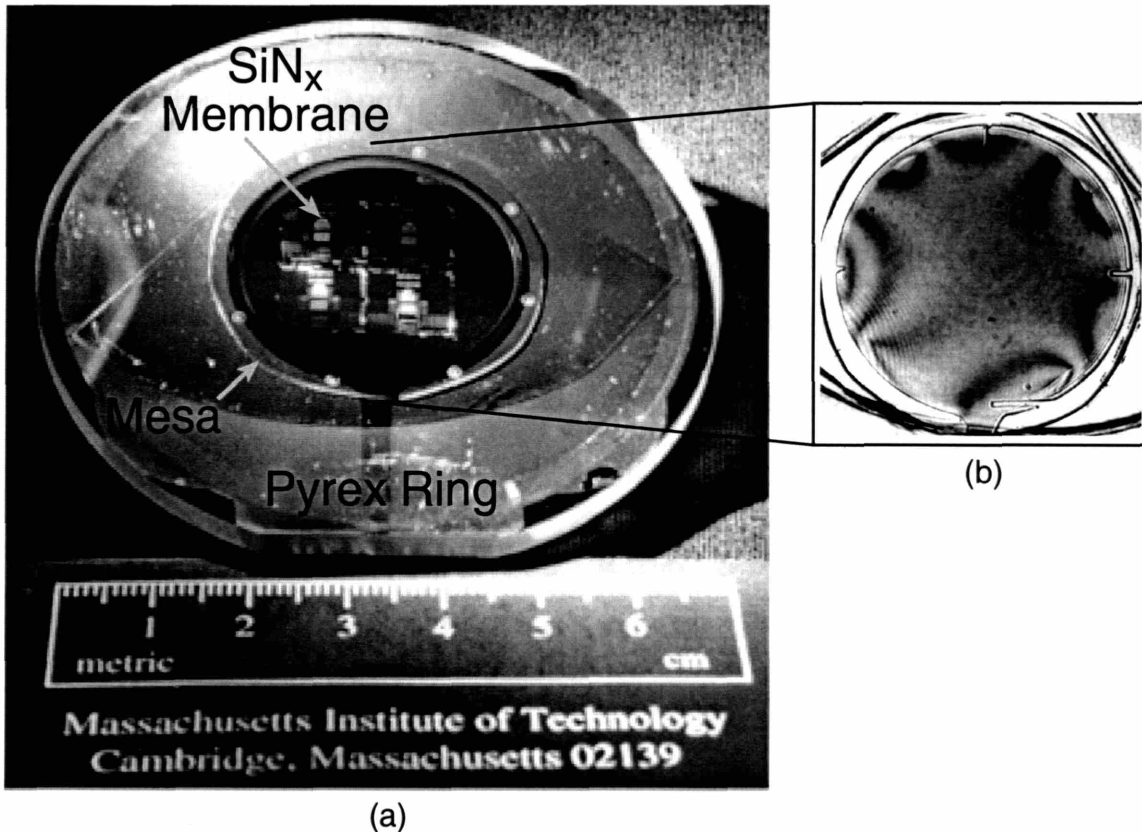

Figure 4-7: (a) MIT x-ray mask structure. (b) Interferogram showing mask membrane flatness.

The mask design used in the NSL is shown in Fig. 4-7(a). The Si-rich, low-stress silicon nitride mask membrane is supported by a silicon annulus, which is anodically bonded to a Pyrex ring. The purpose of the mesa is to allow

[2] For the moment we are setting aside the resolution limits imposed by chemically amplified resists.

the mask to approach the wafer and have room for adjustment in planarity without risking contact on the edge of the mask. Mask flatness is shown in Fig. 4-7(b). Using a Wyco interferometer, a few fringes are seen across the 31-mm mask diameter. In this case an older mask, with less than optimal mask flatness, was chosen to illustrate the fringes. With flatter masks available now [13], only half a fringe is visible across the mask surface, corresponding to flatness better than 250 nm.

In the Head 4 system a wide travel range and high repeatability require a division of responsibilities between the stages. The combination of mask and wafer stages is utilized to give precision motion better than 1 nm at any site on the surface of an 8" wafer. This task is divided between the mask and wafer stage, with the coarser alignment (down to 250 nm) done with the X, Y, θ wafer stage. Fine alignment down to <1 nm utilizes the closed-loop, piezo- X, Y, θ mask stage. Figure 4-8 shows the mask and wafer stages during loading.

Each set of stages includes some form of feedback to control the position of the actuators. The wafer stage [14] has optical encoders integrated within the stages to provide bi-directional sub-50 nm repeatability in X and Y motions. Rotation is controlled in a similar manner to 0.5 arcsec. The gap and θ_x and θ_y angles of the mask are controlled to within 50 nm by a set of three matched Z-drives with optical encoders. The mask plate is designed to rest on the three Z-drives. The interface between the drives and the plate consists of

kinematic mounts in the classical cup, v-groove, and flat arrangement, in contact with the ball tip of each Z-drive. The settling time of the DC-servos is on the order of 1 second. Not suprisingly, this is much slower than the settling time of the piezos (<0.1 sec).

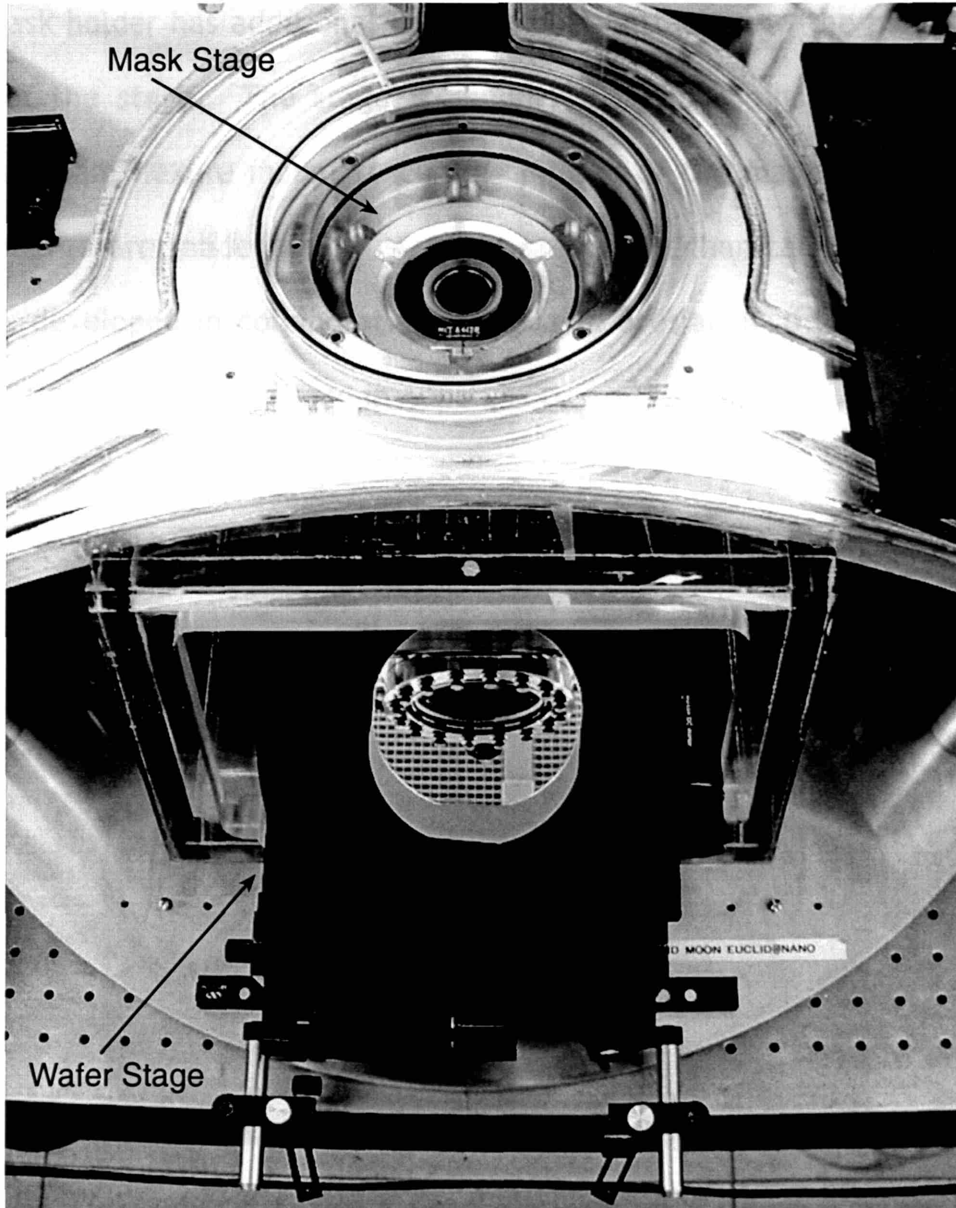

Figure 4-8: Photograph of mask and wafer with wafer stage in loading position.

The mask stage (Fig. 4-9) requires high-resolution position actuators and sensors to make precise sub-nanometer motions. In each piezo device [15], a capacitive sensor and a piezo stack are both contained in an Invar housing. A custom-built "ninja throwing star" design mask stage holds the three piezos on flexure mounts, providing nanometer positioning of the mask in X, Y, and θ. The mask holder has additional flexure mounts attached to the piezos on the sides of the stage. The stage is supported by four pins, which act as a parallelogram flexure mount to confine motion of the mask to a plane. All components are made of 304 stainless steel. Mechanical drawings of the stages, developed in collaboration with David Breslau in the MIT Center for Space Research, are contained in Appendix D.

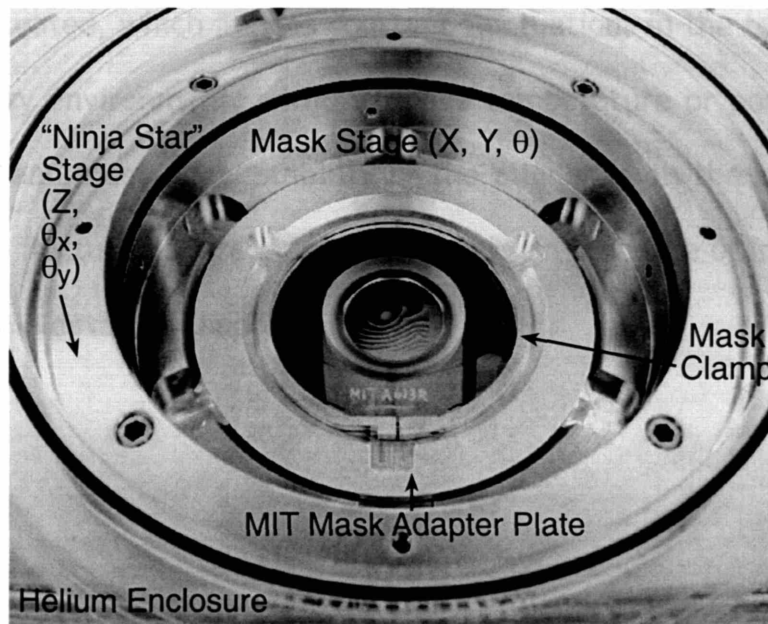

Figure 4-9: Photograph of a mask in the mask stage. The fringes observed between the mask and wafer at a microgap indicate a wedge-shaped gap, which will be removed by leveling the mask stage.

A mask is held in place by means of a circumferential ring clamped around the Pyrex ring of the mask. We prefer a circumferential clamp design since it acts in the plane in which the Pyrex mask ring has the most rigidity and it applies forces with circular symmetry. In this way, fixture-induced mask distortions are minimized. The thickness of the clamp is somewhat less that the thickness of the Pyrex, hence this ring provides a lip from which the mask can be supported easily. The clamped mask rests in a beveled holder attached to the piezos. Both NIST and MIT mask standards can be used in Head 4. A simple adapter plate is added when using the smaller-diameter MIT mask.

Note that the stages are not held within a temperature-controlled enclosure. A large volume of air is transferred in the cleanroom where the stages are situated, which implies constant fluctuations in the temperature. In the laboratory environment, without active temperature or position control, the thermal and mechanical stability of the aligner is on the order of a few nm/s. These fluctuations are indeed noticeable on our scale of interest, as will be described in detail in Chapter 7.

4.4 Helium Enclosure

As shown in Fig. 4-10, soft x-rays at λ = 1.3 nm are absorbed readily by air. The attenuation depends strongly upon the percentage of oxygen in the x-ray beampath. For this reason, we constructed a plexiglas containment enclosure and purged the region around the source and stages with helium. An oxygen sensor [16] uses a chemical reaction to detect the amount of oxygen flowing out of the enclosure. The exposure starts only when the oxygen level is below 200 ppm, and typically runs below 100 ppm during the course of the exposure.

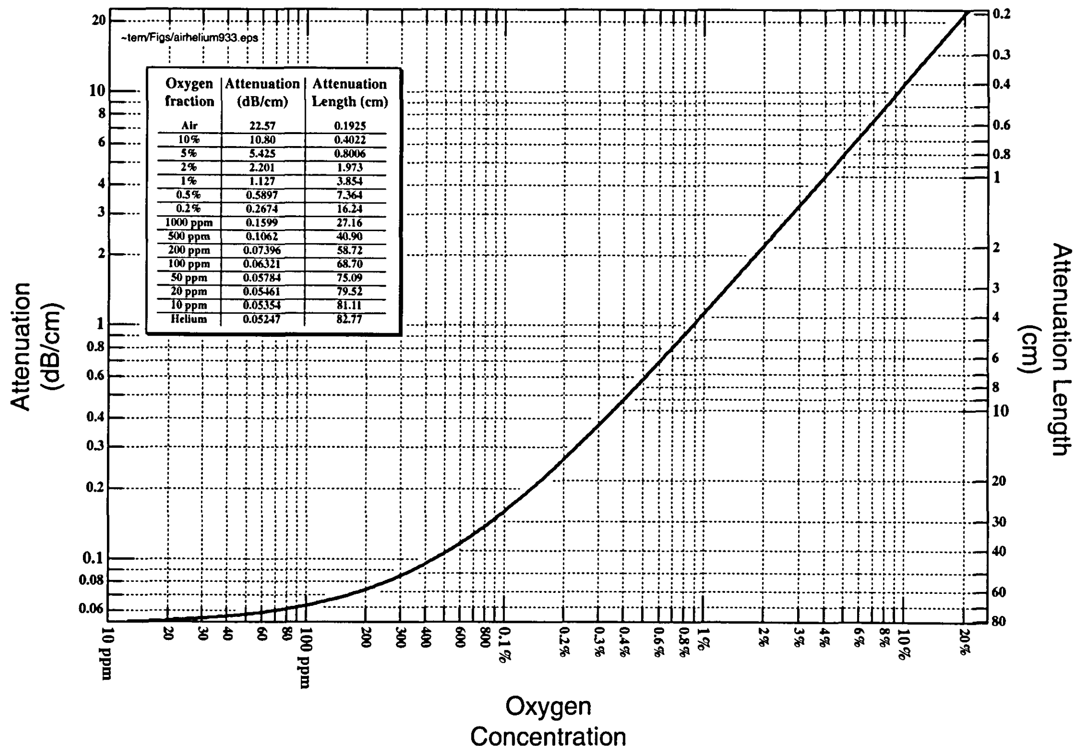

Oxygen fraction	Attenuation (dB/cm)	Attenuation Length (cm)
Air	22.57	0.1925
10%	10.80	0.4022
5%	5.425	0.8006
2%	2.201	1.973
1%	1.127	3.854
0.5%	0.5897	7.364
0.2%	0.2674	16.24
1000 ppm	0.1599	27.16
500 ppm	0.1062	40.90
200 ppm	0.07396	58.72
100 ppm	0.06321	68.70
50 ppm	0.05784	75.09
20 ppm	0.05461	79.52
10 ppm	0.05354	81.11
Helium	0.05247	82.77

Figure 4-10: Attenuation of Cu_L x-rays through air/helium mixture. In air, the x-rays are absorbed in less than 1 cm, whereas in 100 ppm O_2, the attenuation length is about 3 times the 25-cm distance to the mask[3].

[3] Figure courtesy of Thomas E. Murphy.

Our system positions the x-ray source 25 cm from the mask. If the beam path is in air, the Cu_L x-rays are absorbed in less than a centimeter. To avoid attenuation, the exposure could be performed in vacuum. However, helium is preferred due to its higher thermal transfer coefficient. In the absence of thermal transfer to an ambient gas, heating of the mask by the x-ray flux could contribute to mask distortion.

Nevertheless, helium, or any gas, causes a problem when bringing the mask into proximity with the wafer at small gaps since the gas pressure under the mask slowly equalizes with the ambient pressure through the small gap at the circumference of the mesa. The gap cannot be changed suddenly from large to small gaps of a few microns without waiting for a period of time for the gas pressure to equalize.

Particulars of the helium system are shown in Fig. 4-11. In the top of the helium box is a 4" dia. 0.5" thick window with 0.75" borethough, flat to $\lambda/10$ [17]. A plexiglas box surrounds the mask and wafer stages[4]. Doors in the front and top of the box are sealed by dual o-ring vacuum seals. The helium

[4] Even though helium is only required in the beampath, the mask and wafer stages are completely enclosed in the helium box for several practical considerations. It is impractical to enclose the IBBI microscopes and their stages inside the helium, hence they need to observe the mask from outside the helium enclosure. Then there is the fact that the minimum size helium enclosure would make contact with the mask. This brings up several problems, including the need to make a good seal, and at the same time have a seal that will not couple vibrations to the mask or hinder the motion of the mask. The difficulties encountered here seem overwhelming, which means that the seal must be made to the mask stage. This brings up many complexities, involving making a good seal to the moving stage. Finally, the pressure of the helium must be regulated much more carefully, since the slightest overpressure would cause bowing of the mask membrane, and possible mask distortion.

flow is controlled through a manual flow controller and during the initial He purge is pulled through by vacuum applied to the outlet of an oxygen sensor. A differential pressure meter [18] monitors overpressure of the helium ambient. This minimizes the risk of breaking the nitride vacuum window from overpressure inside the enclosure. Helium flow is enabled on the front panel of the Head 4 control software. The flow is automatically halted at the end of an x-ray run.

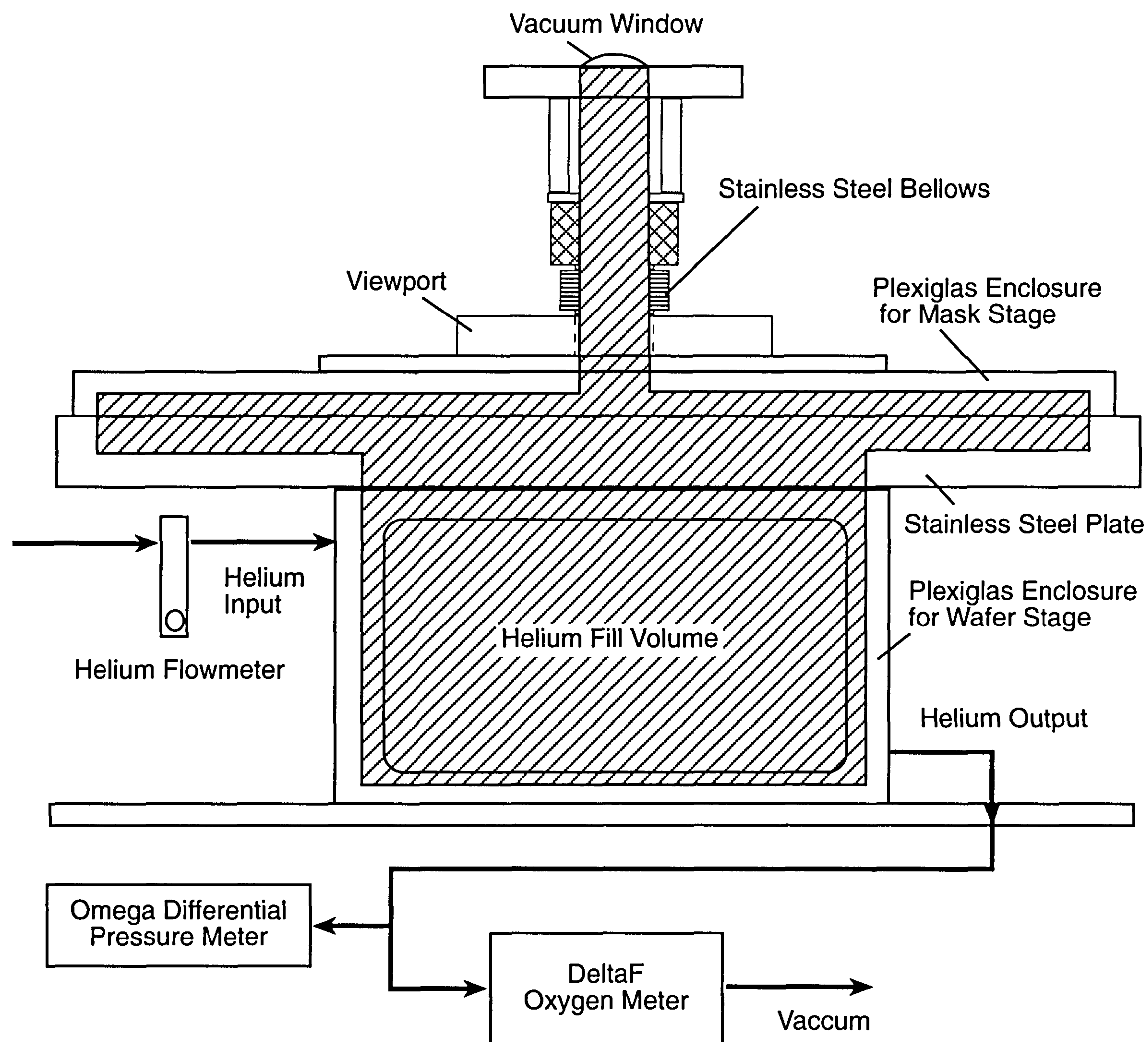

Figure 4-11: Helium enclosure and purge system.

4.5 Broadband Light Source

Broadband illumination is chosen to reduce speckle and thin-film effects in layers of resist. Although IBBI is compatible with spatially coherent white-light illumination, for reasons of signal intensity we use a multi-line single-mode argon laser [19], with six spectral lines between 457 and 515 nm. Figure 4-12 shows the compact laser we use currently. The output power of the laser is 40 mW.

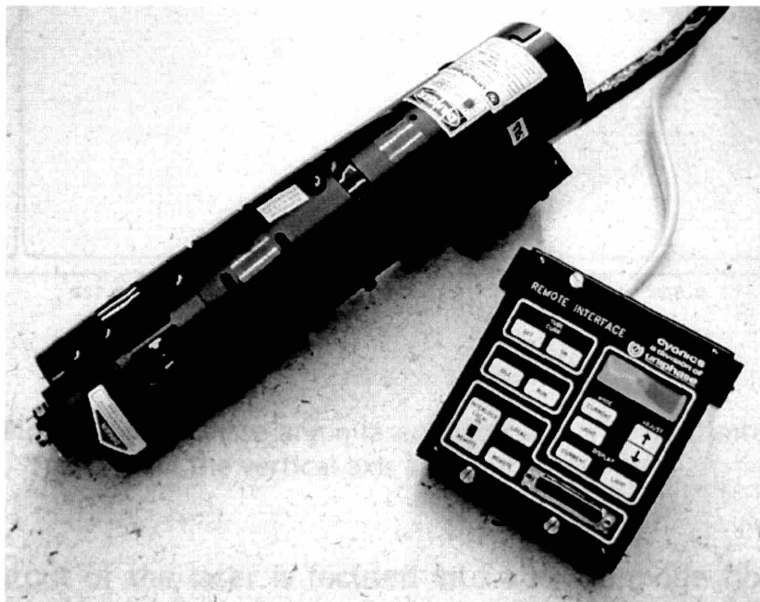

Figure 4-12: Multi-line argon laser and remote control box.

Figure 4-13 shows the spectrum of this laser. To avoid thin-film interference effects, the most desirable situation would be to have equal intensity in a broad spectrum of lines. While not considered optimal, the six

spectral lines (457, 476, 487, 496, 501 and 515 nm) are arranged in three pairs of roughly equal intensity. Although the line pairs of lower intensity are only about a quarter to an eighth of the intensity of the strongest lines at 487 and 515 nm, this multi-line laser has proven to be far more effective at reducing speckle than a combination of two monochromatic lasers.

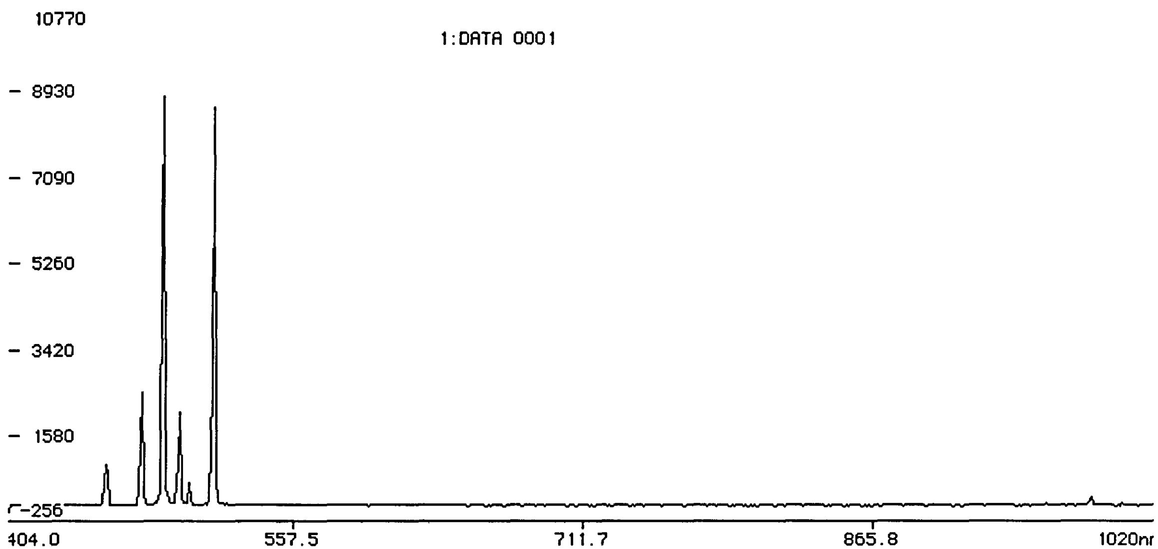

Figure 4-13: Plot of the Uniphase argon laser spectrum. The horizontal axis has units of nanometers. The units of the vertical axis are arbitrary.

The output of the laser is focused into a single-mode fiber optic [20], whereupon it is split into several parts, one for each IBBI microscope.

4.6 Microscopes

Each set of microscope optics (Fig. 4-14) includes a 12x, f/10, 110 mm working-distance microscope [21], a monochrome CCD camera, [22], a 5-axis kinematic fiber mount, and a silicon mirror held by a kinematic mirror mount [23].

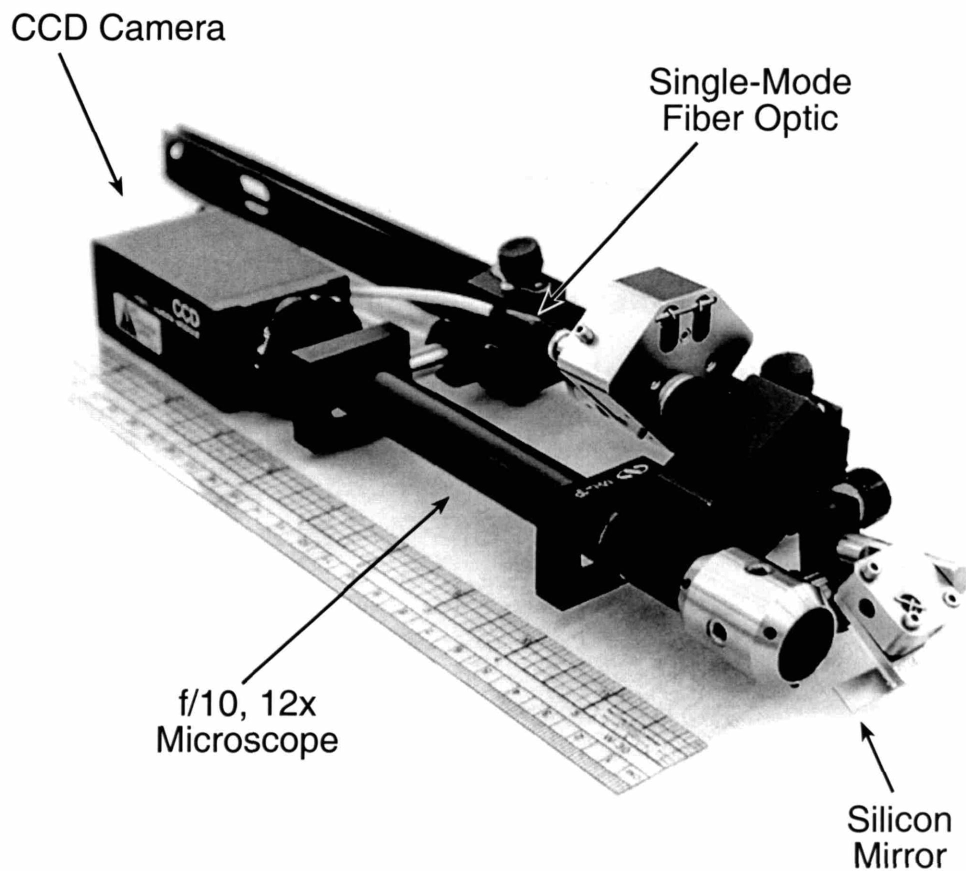

Figure 4-14: IBBI microscope.

The illumination is brought to each microscope via a single-mode fiber optic [24]. For convenience and compactness we choose to house the

illumination path and the imaging path in the same microscope body. By positioning an image of the emitting end of the fiber in the back focal plane of the microscope objective, a collimated beam of broadband light is formed beyond the microscope objective to illuminate the mask and wafer alignment marks. The laser light is combined into the microscope's optical path through an internal beamsplitter, and emerges in a 0.5-mm diameter collimated beam, placed about 2 mm from the optical axis. This displacement minimizes reflections back toward the CCD and must lie in the plane of incidence to the mask. The microscope alignment procedure is described in Appendix C.

The resolution of the microscopes is rather low, only 7 microns, yet through the moiré magnification of the interference pattern, the microscopes are used to detect displacements 10,000 times smaller than their resolution.

CHAPTER 5:

EXPERIMENTAL VERIFICATION:

IBBI DETECTIVITY AND ROBUSTNESS

5.1 Alignment Detectivity

An experimental verification of the detectivity of IBBI [25] compared the spatial phase detected by IBBI microscopes prior to exposure with the spatial phase of a moiré pattern in the resist after exposure and development. Before the exposure, a fringe pattern resulting from the interference of diffracted beams was observed by the IBBI microscopes. After the exposure, a moiré pattern between the patterned resist and the complementary pattern etched into the wafer was viewed at normal incidence by an ordinary optical microscope. Despite the fact that the physical mechanisms forming the fringe patterns are different, the spatial phase should be the same in both cases. The agreement between the two moiré patterns observed by two different physical

mechanisms and two different types of microscopes is taken as an indication that the pattern transferred to the resist is highly correlated with the IBBI measurement.

In preparation for this experiment, numerous factors required consideration. First, an array of marks was written on a mask to allow statistics to be generated using a single mask and exposure. But this raised issues of pattern placement, namely, e-beam placement accuracy over the diameter of the mask. Between each e-beam field (typically on the order of 100 nm) there are stitching errors, which can include shifting, rotation and scaling of the field by several nanometers[1]. These errors are considerably greater than the detectivity of IBBI, and, if included in the measurements, would invalidate the experiment. Marks written within a single field, however, contain minimal distortions, i.e., only intrafield distortions. The spatial consistency from mark to mark may be further complicated by distortions in the mask resulting from absorber stress and mechanical fixturing. Pattern magnification due to the point source, a final source of error from mark to mark, was eliminated by performing the exposure with the mask in intimate contact with the wafer.

[1] We expect the problem of e-beam pattern placement accuracy can be solved by spatial-phase locking methods [26]. But using Spatial Phase-Locked E-Beam Lithography (SPEBL) to write the mask at this point in time would only convolve its performance with that of IBBI, and would not truly elucidate IBBI detectivity.

The question of IBBI detectivity was separated from these issues simply by taking the difference of the spatial phase measurements before (in CCD) and after exposure (in resist). Of course, the absolute value of the measurements exhibited the distortions discussed above, but the difference of the spatial phases is the only quantity of interest in this experiment.

A final issue is how to measure with nanometer accuracy the placement of the patterns in the resist relative to patterns etched previously in the wafer. Since we are interested in nanometer or sub-nanometer measurements, there is no measurement method currently available in the semiconductor industry suitable for this task. However, moiré methods are well known to yield sufficiently high sensitivity, and fortuitously, a moiré pattern is formed between the resist and the complementary grating mark etched into the wafer, which has the same fringe period as the interference fringes viewed by IBBI. The question of analysis method then has a simple response: we analyze both the IBBI microscope image and the resist moiré image using exactly the same algorithm[2].

Thus, for tests of IBBI, instead of writing two separate marks for alignment and test purposes, a more elegant approach is to use the moiré

[2] One may ask, is it informative to use the same algorithm to analyze both types of fringes? That is, could some hypothetical, systematic error give similar results, yet not have any physical meaning? We address the issues of scale in Chapter 6. Here we can mention that the results given there indicate good agreement between IBBI and an external scale reference.

fringes for both purposes, albeit with somewhat different underlying physics and observation mechanisms.

With the above considerations in mind, we designed a special alignment/test mask and conducted the x-ray exposure tests as follows. We wrote on a JEOL JBX 5D II e-beam system at the Naval Research Laboratory (NRL) a single x-ray mask that contained 96 of the $\{p_1:p_2\}$ alignment marks appropriate for IBBI, plus a variety of additional patterns. The alignment mark gratings had periods of ~1, 2, and 4 μm. A first x-ray exposure transferred the mask patterns onto a silicon wafer, where they were subsequently etched in relief using reactive-ion etching. The substrate was then recoated with SAL 601 resist and placed back in the IBBI alignment apparatus. The x-ray mask was rotated 180 deg. which, by virtue of its designed symmetry, brought $\{p_1:p_2\}$ gratings on the mask into approximate superposition with $\{p_2:p_1\}$ hatched gratings on the substrate (i.e., a 180 deg. rotation converted $\{p_1:p_2\}$ pairs to $\{p_2:p_1\}$ pairs). The mask was then brought into alignment and lowered onto the substrate, where it went into intimate contact. We then extracted from each pair of alignment marks the spatial-phase difference between the left and right interference fringes, and converted that into a displacement, called ΔX_1. Following exposure, we developed the resist and measured the overlay of the $\{p_1:p_2\}$ resist patterns on the $\{p_2:p_1\}$ relief gratings in Si for all of the mark pairs. A representative example is shown in Fig. 5-1.

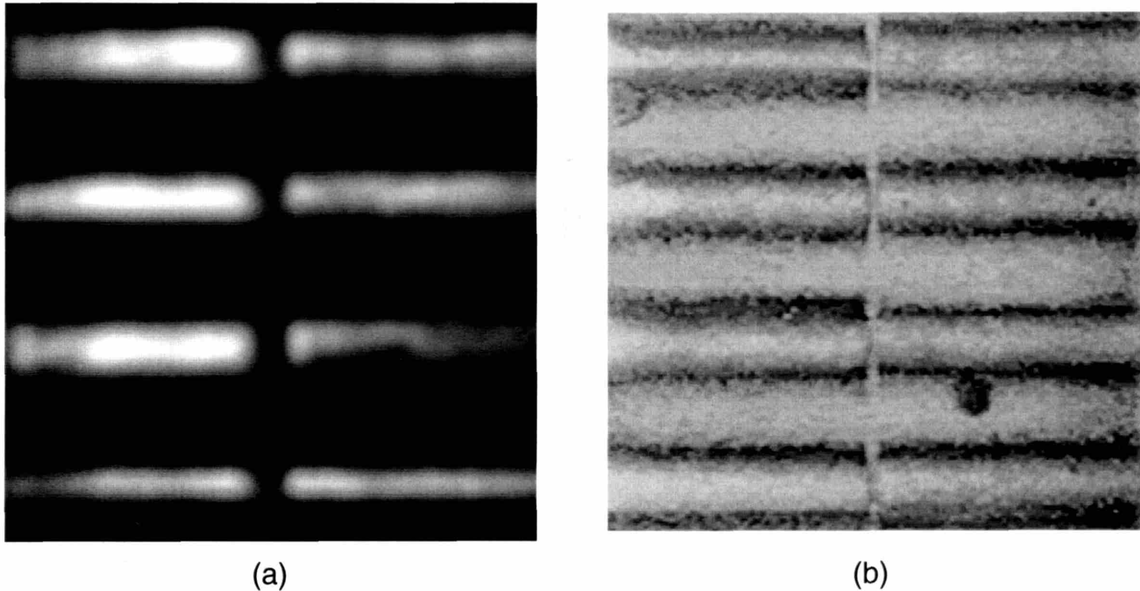

Figure 5-1: (a) Fringe pattern observed through IBBI microscope (Δx_1=1.2 nm).
(b) Fringe pattern in moiré pattern between exposed resist and grating in substrate observed by Leitz microscope (Δx_2=1.7 nm).

The measured displacement of the moiré image of resist on a Si relief grating is called ΔX_2. We call the quantity (ΔX_1 - ΔX_2) the "disparity between detected and measured misalignment". The alignment difference was found for 24 marks. The difference of these measurements is plotted in Fig. 5-2 for marks with ~1 μm grating period. Alignment as perceived by IBBI and alignment shown in the exposed pattern agreed to σ = 0.8 nm.

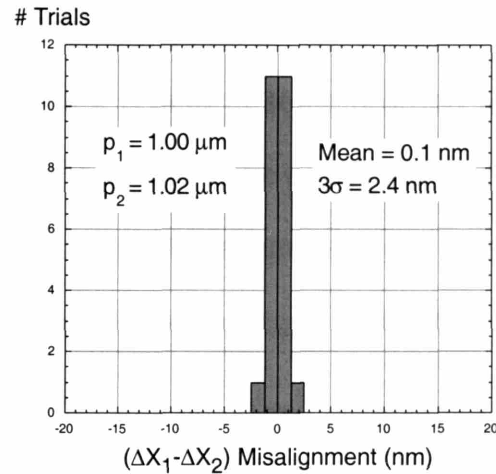

Figure 5-2: IBBI alignment detectivity, showing a histogram of $(\Delta X_1 - \Delta X_2)$ for the 1 μm-period alignment marks. The difference of moiré fringes as detected in an IBBI microscope before exposure and fringes observed in resist with a different microscope on axis after exposure and development. X-ray exposure is done with the mask in contact with the wafer to eliminate the effect of point-source magnification. The mean difference was 0.1 nm and $\sigma = 0.8$ nm.

We believe this experiment has proven that there is a correspondence between the misalignment, as *detected* by the IBBI optics and algorithm, and the misalignment as *measured* in x-ray-exposed resist. We believe the results demonstrate that the IBBI scheme has a detectivity of misalignment better than 1 nm, with a standard deviation of < 1 nm.

Due to the e-beam and other distortions that caused wide variations in the spatial phase from mark to mark, we conclude that the IBBI scheme can precisely measure not only the spatial phase differential of aligned (zero phase) fringes, but also any arbitrary amount of spatial phase offset. In practice, every alignment mark cannot be aligned at the same time, due to inaccuracies propagated from other systems or processes. Thus, one strives for

a best-fit alignment, which implies that the best overall alignment is made when each alignment mark is held at some position with a specific offset. To our knowledge, because it can measure any phase discontinuity, IBBI is the only scheme that can measure a displacement from a nominal alignment point. Such a capability is of significance in many applications.

5.2 Detectivity Variation with Grating Period

At times it may be desirable to write IBBI alignment marks in an optical stepper, which may not have the ability to write 1 μm-period gratings. From the equations governing detectivity (Section 3.1) one would expect some reduction in detectivity with enlarged grating periods. We will now ascertain if this expectation is consistent with the experimental data.

Using data from the exposure described in the previous section, the same procedure was applied to marks with 2 and 4 μm periods. Fig. 5-3 shows the statistics of the differences between IBBI and resist moiré spatial phase, converted into distance units.

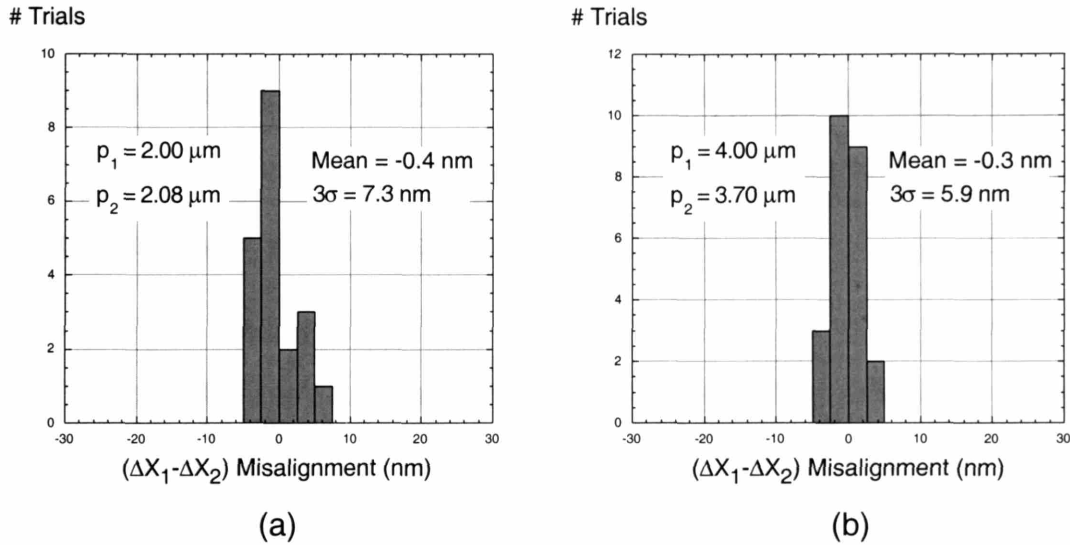

Figure 5-3: Variation of alignment detectivity with grating period for (a) 2 μm and (b) 4 μm-period gratings.

The detectivity for the larger periods is diminished, as expected. However, the standard deviation for the 2 μm-period marks is larger than for the 4 μm-period marks. We attribute this to the large number of defects (large areas of missing grating) in the 2 μm-period marks. It is noteworthy that despite these defects we still obtain $\sigma < 2.5$ nm.

5.3 Immunity to Process Coatings

In the past, several alignment schemes promised nanometer-level detection, yet in practice fell short of expectations, due in large part to the effects of process coatings. When alignment marks on the wafer are covered

with various grown and deposited layers, such as resist, polysilicon, and aluminum, the phase and amplitude of the reflected light are altered due to scattering and interference of beams from the multiple interfaces. This usually alters the alignment signal, leading to overlay errors.

We expect a spatial-phase detection scheme such as IBBI to be immune to many of these potentially disturbing influences. In an experiment [27] an IBBI alignment mark was etched into silicon, and half of the mark was covered with an overlayer (Fig. 5-4). The mark was observed with an IBBI microscope, and the resulting fringe patterns for the upper and lower halves of the mark were analyzed separately.

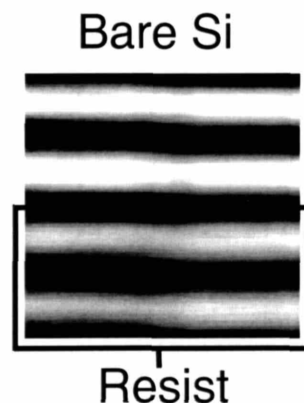

Figure 5-4: Image of an IBBI alignment mark etched into a wafer. Half of the mark was covered with an overlayer. The other half was left bare. Experiments were done with overlayers of resist, polysilicon, and aluminum.

The effects on alignment of three types of overlayers - photoresist, polysilicon, and aluminum - were investigated. Wafer alignment marks consisted of gratings p_1 = 3.7 μm and p_2 = 4.0 μm, etched 100 nm deep into a Si wafer. The marks, which occupied an area 200x200 μm, were covered with a given overlayer, and then that overlayer was removed from one half of the wafer alignment mark. When the mask alignment mark was superimposed above the wafer alignment mark, a pattern such as shown in Fig. 5-4 was obtained. In this case the overlayer was resist. Similar results were obtained for the polysilicon and aluminum overlayers. The mask-wafer gap was 10 μm.

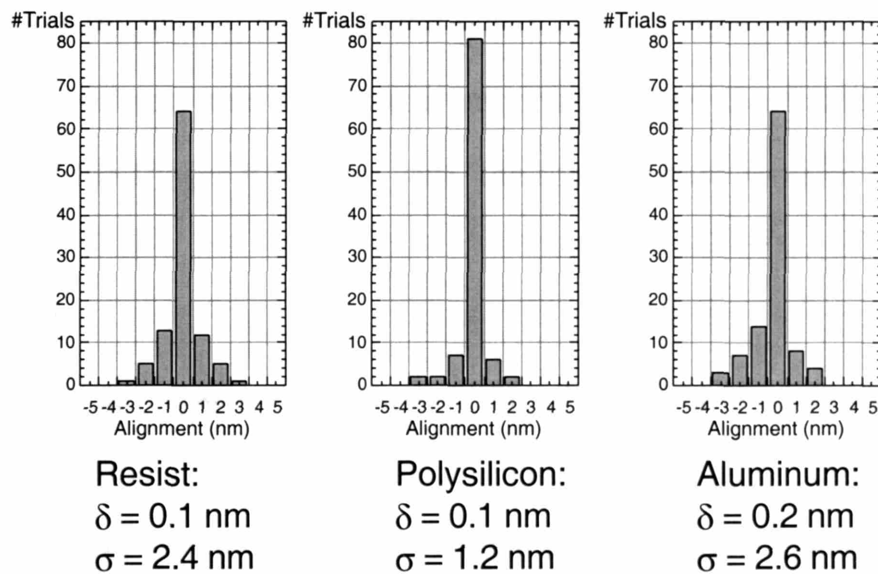

Figure 5-5: Immunity of IBBI to overlayers of resist, polysilicon and aluminum. Layers of resist, polysilicon, and aluminum are shown to cause minimal degradation of the alignment signal.

Figure 5-5 displays the results of measurements of the difference in the spatial phase discontinuity in the half of the alignment mark with the overlayer and the half without the overlayer. The 100 measurements for each overlayer

yielded a mean offset, δ, as well as a standard deviation, σ. The measured effects of the overlayers were δ = 0.1 nm, σ = 2.4 nm for 1 μm of photoresist; δ = 0.1 nm, σ = 1.2 nm for 0.3 μm of deposited polysilicon, and; δ = 0.2 nm, σ = 2.6 nm for 20 nm of deposited aluminum.

The significance of the result shown in Fig. 5-5 is that an overlayer does not appear to affect the *spatial phase* of the interference pattern. This is due to the fact that the two sides of the mark provide mutual references, and despite possible changes in the phase on each side, the relative phase is essentially unaffected. Image contrast is altered by the overlayer (increased, in the case of aluminum), but since the spatial phase is detectable over a wide range of intensities, this is of little importance. In short, although the amplitude of the fringes is seen to vary, the spatial phase remains essentially unaffected.

Another advantage of IBBI is that since it is a phase-sensitive scheme, the line-space ratio of the gratings is not of critical importance, and deposition of metallic layers will not affect the relative spatial phase. Again, these will affect image contrast, but not the phase.

We have demonstrated that any overlayer which causes a phase change on one side of the mark, will also, in all likelihood, affect the phase on the other side of the mark in exactly the same way since each set of fringes is

formed by the interference of symmetric diffractions from mask and wafer gratings. In contrast, in an amplitude-based scheme, the alignment signal could depend on a plethora of factors such as the gap, overlayer type and thickness, transmission of the mask, output stability of the laser, etc. The only situation in which the phase symmetry in IBBI would be broken would be for extreme variations in the layer thickness occurring over the small extent of the alignment mark (typically 100 microns or less). The data suggest that thickness variations of a magnitude sufficient to distort the signal are not encountered in practice. However, it should be noted that processes that induce a blazing of the gratings, i.e., an asymmetric covering of the gratings, will shift the grating lines in one direction. This is equivalent to moving the wafer gratings, which we know will cause the observed fringes to shift in opposite directions. Thus, in the special case of asymmetric overlayers, we expect a spatial offset. However, the ability of IBBI to detect arbitrary offsets with equal accuracy should allow one to correct for a systematic error caused by an asymmetric covering of the grating.

In Section 3.2 it was noted that there is a lower limit to the number of fringes allowed in the image before the spatial-phase detection algorithm begins to break down. In this experiment, which was done before we had discovered this limitation, we were operating close to this limit: about 5 fringes over the entire mark, or fewer than 2.5 fringes in each half. We now suspect that the statistics of Fig. 5-5 include error contributions from the

algorithm. As a result, we believe the effect of overlayers may be even *less* than indicated by this data.

5.4 Insensitivity to Environmental Conditions

Due to their inherent left-right symmetry, the IBBI interference fringes are expected to be indifferent to the long optical beam path through air, glass, and helium. Figure 5-6 shows the consistency of measurements performed before exposure in air without the viewport, and during x-ray exposure in helium, looking through the viewport.

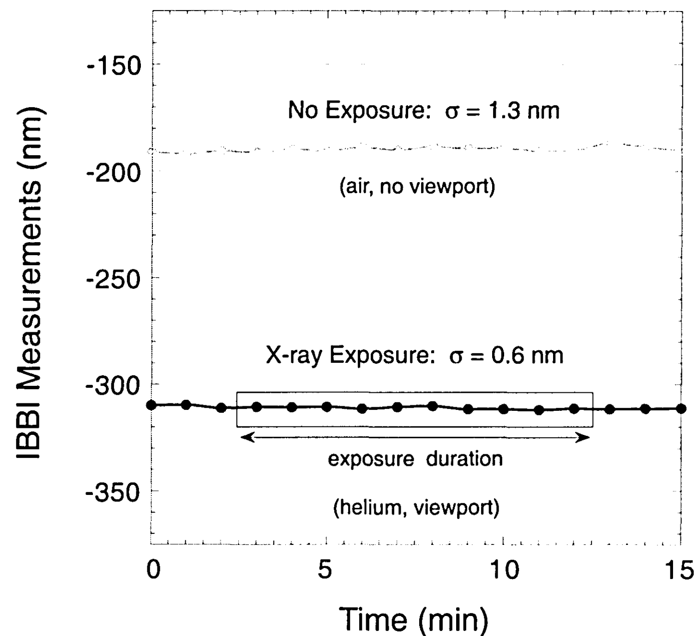

Figure 5-6: Comparison of alignment observed under different optical paths: in air and through a path consisting of air, glass, and helium.

X-rays were turned on for 10 minutes in the middle of the 15-min data acquisition. The mask was resting upon the wafer at a 3 μm gap set by Al studs.

This data suggests several null results:

- The type of gas in the optical path does not affect the spatial phase.
- The viewport does not affect the spatial phase.
- The x-ray exposure does not disturb the IBBI measurement.

The data above was taken under normal exposure conditions in Head 4. Normal conditions imply a very low helium flow, with the gas inlet and outlet several tens of centimeters from the viewport. It is of interest to determine if IBBI fringes will be affected by helium flow under (somewhat perverse) conditions of high flow and close proximity to the optical path.

An experiment was conducted with a stream of helium flowing from the end of a 1/8" dia. tube placed in front of the IBBI microscope. Figure 5-7 shows images of the interference fringes with (a) no flow, (b) 5 SCFM He, and (c) 10 SCFM He.

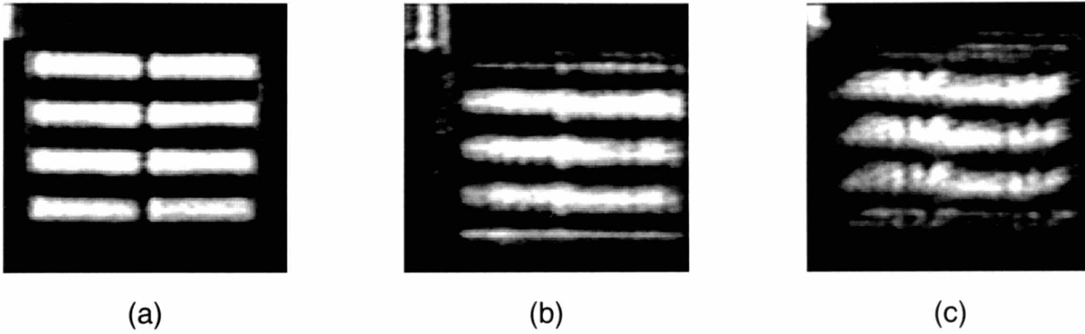

(a) (b) (c)

Figure 5-7: Effect of helium flow on IBBI images. Mask at 5 micron gap. Helium flow from 1/8" dia. tube 10 mm from microscope objective. (a) No helium flow. (b) Helium flow = 5 SCFM. (c) Helium flow = 10 SCFM. In each case the spatial phase discontinuity is unaffected, although the position of the fringes is changed.

As the helium expands from the end of the tube, it forms a wedge of gas with a different index of refraction than air. The result is that as He flow increases, the position of the fringes within the field of view of the microscope gradually moves to one side. This shift is evident between Fig. 5-7(a) and (b). Increasing the He flow further caused significant turbulence and rapid oscillations of the fringes within the image as shown in Fig. 5-7(c). Despite these effects, the spatial phase between the fringes is unchanged.

CHAPTER 6:

MEASUREMENT CORROBORATION WITH TWO MICROSCOPES

6.1 Experimental Setup

In an experiment described in this chapter, two IBBI microscopes observe the same alignment mark from opposite directions [27]. The purpose of this experiment is twofold: first, it will determine if small deviations in detected alignment are real, or noise. This experiment also will show any variation of the alignment signal from one scope to another that may be caused by differences in the optics, fibers, mirrors, etc.

Another experiment will compare the scale of the displacement measured by IBBI with an independent reference, a pair of calibrated piezos.

In this experiment two microscopes measured alignment at two marks separated by 5 mm during a series of piezo scans.

The IBBI arrangement used in this series of experiments is illustrated schematically in Fig. 6-1, along with the pair of piezo drives used to translate the mask relative to the wafer. The x-ray flux is delivered to the mask and wafer in a helium environment. IBBI microscopes observe the alignment from outside the helium chamber, through a window.

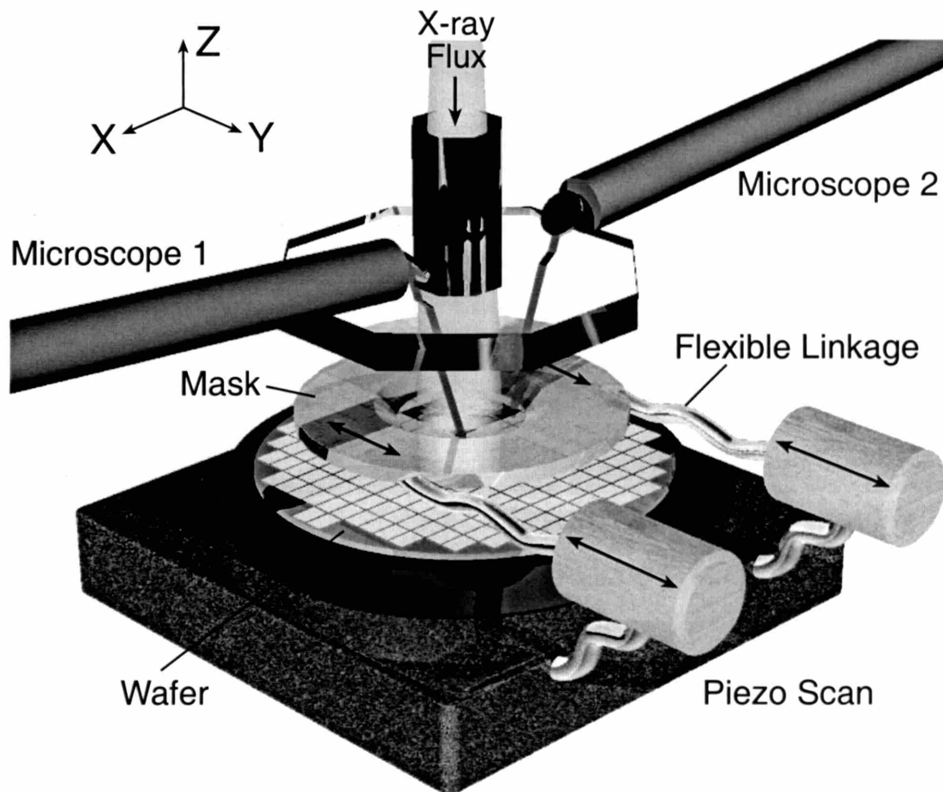

Figure 6-1: Alignment observed at two marks simultaneously by two microscopes. Closed-loop piezos scan the mask stage back and forth over 3.7 μm during observation. The comparison of IBBI with piezos confirms scale. With mask locked to wafer, the same mark is observed alternately by each microscope to determine measurement consistency.

To obtain meaningful results, several error sources must be accounted for and minimized prior to the experiment. Figure 6-2 outlines these error sources and the steps taken to eliminate them.

Error Source	Solution
Angle of incident light in plane of incident illumination	Adjusted angle of incident illumination with mirror mount
Angle of incident light in plane of diffraction at Littrow angle	Adjusted angle of incident illumination with mirror mount
Mask-Wafer azimuthal angle	Adjusted angle by aligning marks separated by 10 mm
Camera-Fringe angle	Adjusted by rotating CCD camera to minimize spatial phase gradient within one fringe set
Non-integer # fringes in CCD	Apply window to sample
Mask-wafer gap	Gap set mechanically on studs
Optical distortions	Tested effect of moving an IBBI microscope such that an alignment mark appeared in different regions of the camera's field of view

Figure 6-2: Table of steps taken prior to experiments to minimize potential errors.

Appendix C provides further information on the microscope alignment procedures.

6.2 IBBI-to-IBBI Comparison

Two IBBI microscopes, looking from opposite directions, observed the same alignment mark. This configuration was chosen to uncover any consistent measurement bias. Since the specular reflection off the mask is directed into the opposite microscope, the measurements were taken alternately, with the light from one microscope blocked while measurements were made through the other microscope. Sequences of such alternating measurements were made, for a total of 150 measurements through each microscope. The results are shown in Fig. 6-3.

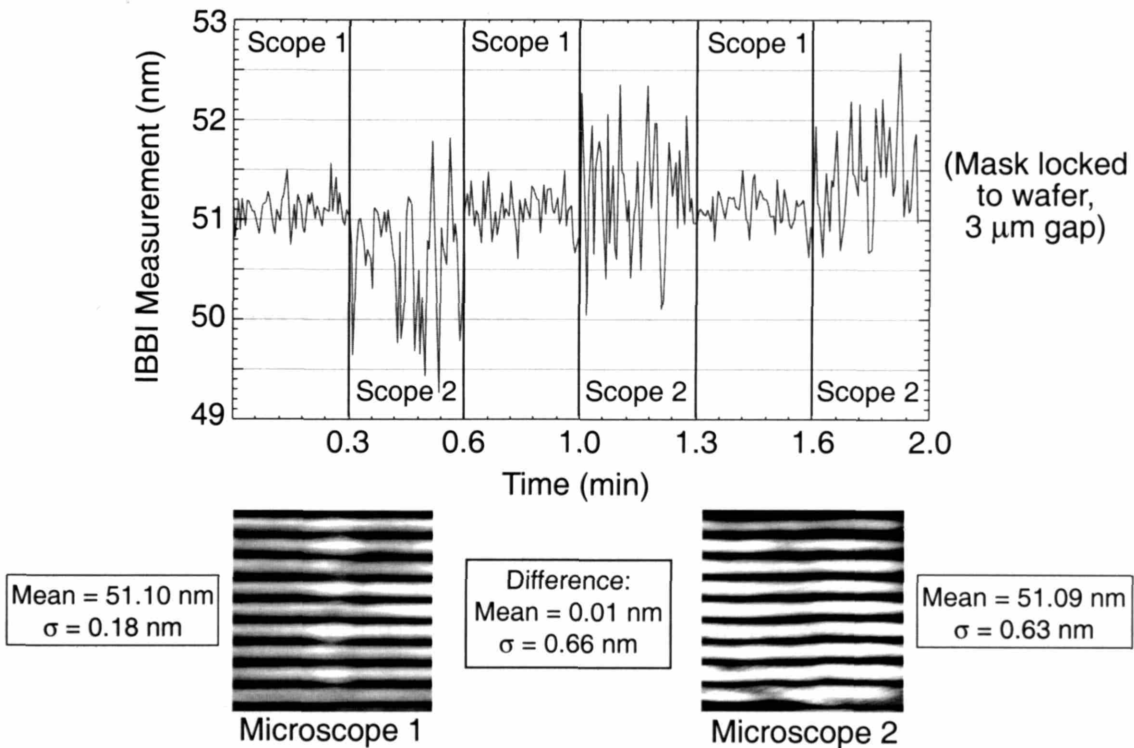

Figure 6-3: Two IBBI microscopes alternately observe the same alignment mark from opposite directions, with the mask locked to the wafer at a 3 μm gap. Measurements agree to σ = 0.66 nm despite reduced image quality in Microscope #2.

The mask was supported on the wafer by 3 μm-tall aluminum spacers evaporated on the mask mesa rim. Setting the mask on the studs implies that the mask and wafer are held in mechanical contact by friction, thereby avoiding relative motion. Any effects of vibration or drift of the mask stage is eliminated when the mask is in contact with the wafer through the studs. A consistent gap is also maintained across the mask surface[1].

Both microscopes measured the same alignment offset of 51 nm, with a standard deviation <1 nm. Microscope #2 gave noisier fringes than #1. This was attributed to greater scattering observed in the optics of the second microscope. However, the noisy fringes did not adversely affect the measurement significantly, indicating the robustness of the measurement.

6.3 IBBI-Piezo Comparison

In order to determine if the phase discontinuity of IBBI can be used to reliably measure any relative position of mask and substrate, IBBI measurements were compared with a piezo drive whose displacement is measured by a capacitive sensor, claimed by the manufacturer to be accurate

[1] The mask stage holds a circumferential ring that clamps around the mask. Lowering the mask stage beyond the point where the studs touch the wafer decouples the mask from the mask stage. The mask is normally held in its stage by gravity.

to <1 nm. This comparison enables us to establish a relative displacement scale.

In the experiment the mask was stationary and then scanned back and forth through 3.7 μm by the piezo drives. The piezos were driven in the Y direction (defined in Fig. 6-1), perpendicular to the grating lines of the marks. IBBI measurements were made continuously on two different marks, separated by 5 mm along the direction of the grating lines. The experiment was performed during x-ray exposure. The gap during the experiments was about 15 μm. Results are presented in Fig. 6-4.

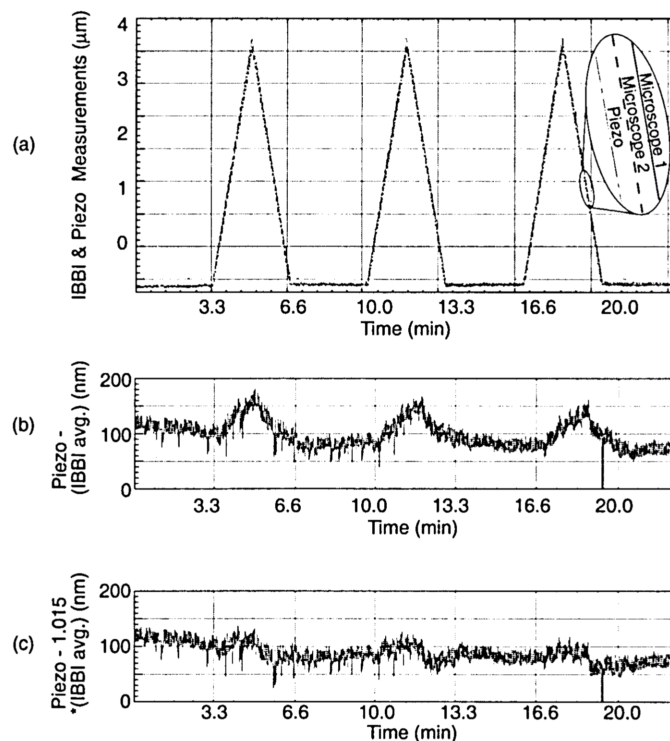

Figure 6-4. Agreement between two simultaneous IBBI measurements and piezo/capacitor drives during 3.7 μm back-and-forth scan of mask. (a) IBBI measurements and piezo displacements throughout three scan/rest cycles. (b) Difference of piezo and average IBBI showing residual scale error. (c) Best-fit found with scale increase of 1.5%. The source of the residual scale error is as yet undetermined, but will have a negligible effect in the application of IBBI.

The uppermost plot in Fig. 6-4 shows the piezo-commanded positions and the two IBBI measurements superposed. The differences were barely distinguishable on the scale of the uppermost plot.

In the middle plot (Fig. 6-4 (b)), the piezo reading minus the average of the two IBBI's is plotted on an expanded scale. This shows the following:

a) A piezo-IBBI offset of about 100 nm. Note, however, that the piezo zero is arbitrary.

b) A slow drift of ~70 nm over the 23-min. duration, attributed to temperature drift.

c) A residual ~55 nm peak-to-peak difference during the driven excursion, indicating ~1.5% scale disagreement between piezo and IBBI.

Figure 6-4(c) shows the same plot after the IBBI data has been corrected by 1.5%. On this scale, the remaining disparity can be easily accounted for by imperfections in the mechanical drives, combined with the drive not being in the same plane as the marks, (i.e. Abbé effect). We do not know the precise details of any waviness of travel in our stepper, but estimate it would lead to a scale error of less than 2%. Hence the scale of the piezo and IBBI agree to within our expected uncertainty of a few percent (e.g., at worst, perhaps a nanometer in a misalignment measurement of 30 nm). This is adequate for our near-term aligning requirements.

6.4 Observation of Magnification Offset

The alignment marks on the wafer were printed from the mask using our x-ray point-source, with a source height of 250 mm and a mask-wafer gap of 3 μm, as depicted in Fig. 6-5(a).

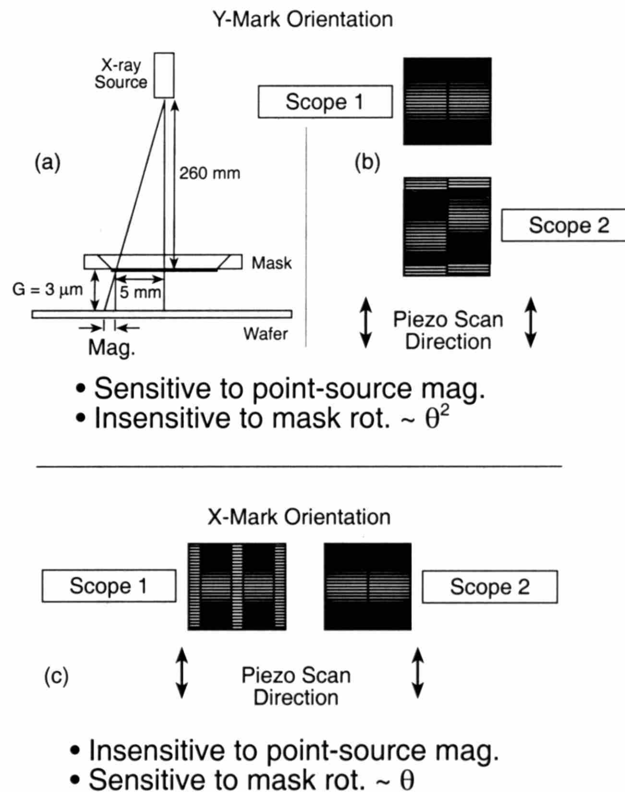

Figure 6-5: Printing magnification due to an x-ray point source, as seen by two IBBI microscopes. Wafer marks were replicated from mask marks. (a) Wafer mark offset due to a point-source exposure. (b) A spatial phase shift is visible between marks in Y-orientation due to the magnification. (c) Magnification is not observable between marks in X-orientation.

Thus, for two alignment marks on the mask, separated by 5 mm, the corresponding separation on the wafer will be increased by 58 nm. This should be evident in IBBI measurements made on marks in the so-called Y-mark orientation, i.e., marks in which the grating lines are perpendicular to a radial

vector from the center of the mask, as illustrated in Fig. 6-5(b). IBBI measurements on marks in this orientation are relatively insensitive to rotational misalignment. For marks in the X orientation (Fig. 6-5(c)) the magnification effect is not observable, but, as we will see, the X-oriented IBBI measurements are highly sensitive to rotational misalignments.

A scanning experiment was done with marks in the X orientation, in which the mask was alternately at rest and scanned back and forth through 3.7 µm, using the piezo drives. Before the scans the mask-wafer azimuthal angle was aligned, using marks separated by 10 mm in the X-direction. The results are shown in Fig. 6-6.

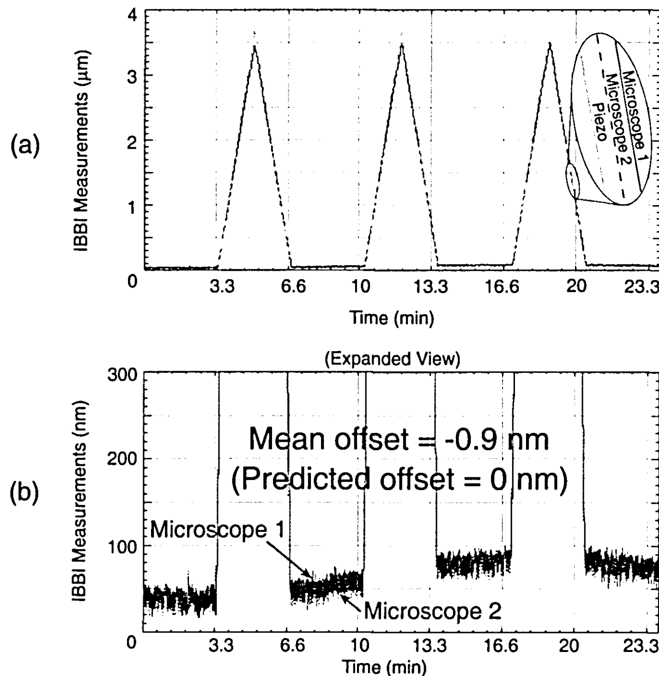

Figure 6-6: IBBI measurements at marks separated in the X-direction during piezo scan. (a) Plot of IBBI measurements during three piezo scans. (b) Plot of measurements on expanded scale. Both scopes track the drift. The mean offset agrees well with the predicted offset.

The upper graph shows piezo and IBBI data superposed. The lower graph shows the IBBI data for the full 23 minutes. The range is such that the IBBI data goes off the scale during the scanning. It is apparent that the two microscopes agree with each other, and with the predicted zero offset to within a nanometer.

The experiment was repeated immediately, but with one microscope moved such that the mark separation is in the Y-direction. The results are shown in Fig. 6-7.

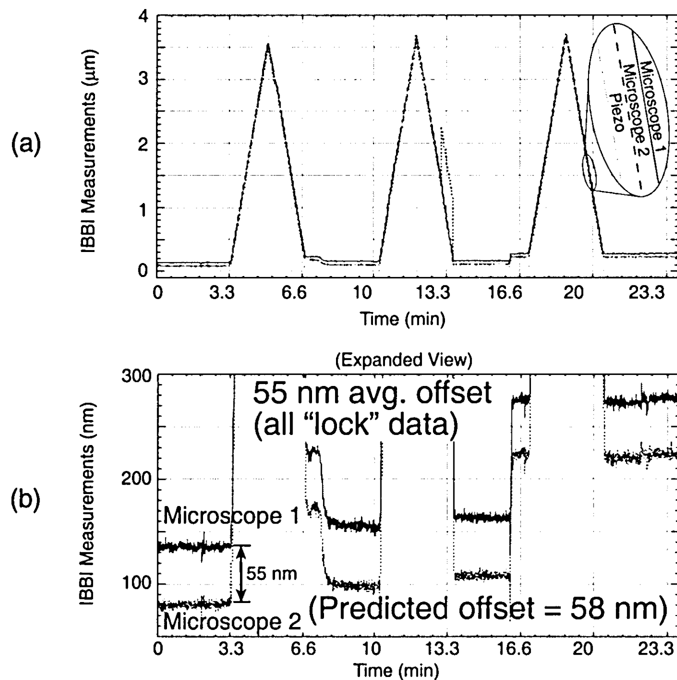

Figure 6-7: IBBI measurements at marks separated in the Y-direction during piezo scan. (a) Plot of IBBI measurements during three piezo scans. (b) Plot of measurements on an expanded scale. Both scopes track hopping. The mean offset agrees with predicted offset to within the uncertainty of the prediction.

Some unexplained hopping in relative mask/wafer position is evident, even during the stationary intervals. It is worth noting that, in spite of the hopping, the difference between the IBBI measurements remains unchanged at 55 nm. The 6% difference between 55 and 58 nm is well within the uncertainty in our gap measurement. X-rays were not on during this experiment.

We believe these experiments provide conclusive evidence that the scale of IBBI is accurate, within the uncertainty of the measurement standards. The two scale experiments done by entirely different approaches increase confidence in the metrological capabilities of IBBI.

CHAPTER 7:

FEEDBACK-STABILIZED ALIGNMENT

7.1 Thermal and Mechanical Instability: Drift and Flutter

On the nanometer scale no mechanical system is immune to thermal drift and mechanical instability. In our aligner the x-ray mask holder is coupled to piezo drives via a few centimeters of metal. The wafer chuck is separated from the piezo drives by about 100 cm of metallic structures. These structures are subject to differential thermal expansion and various forms of wander, which are significant when measuring relative displacement with nanometer resolution. Moreover, the overall stepper structure is subject to vibrational disturbances.

Figure 7-1 shows individual IBBI measurements during a 40-second rest period, i.e., the piezos not scanning and, of course, no feedback locking [28].

On this timescale it is apparent that two IBBIs are measuring a fluttering, transverse motion of mask relative to wafer, of about 20 nm in the measuring direction.

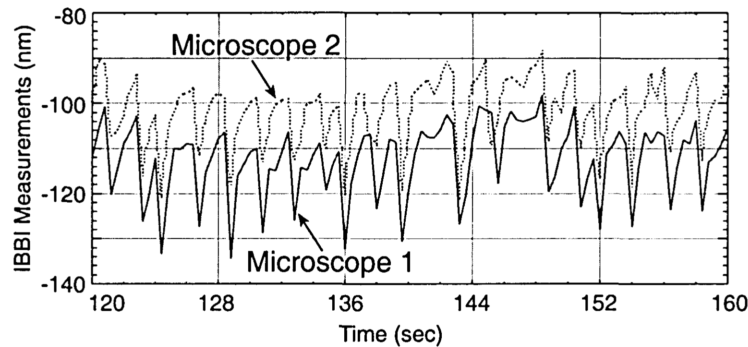

Figure 7-1: Vibration of mask/wafer detected simultaneously by two IBBI microscopes.

Since the IBBIs are looking from opposite directions, this agreement confirms that the flutter is real and not due to artifacts within the instruments. The difference between the two IBBI measurements is attributed to a small rotational misalignment between mask and wafer (the marks are separated by 5 mm along the direction of the grating lines).

The apparent period of the flutter is about 2 seconds. However, since the IBBI measurements were at intervals of 0.4 sec, the observed flutter may reflect aliasing from a higher frequency. It should be noted that this experiment was conducted during a busy afternoon period in the laboratory with environmental vibrations at their maximum and the x-ray equipment running. IBBI measured a flutter that we had not previously been aware of, demonstrating its usefulness for monitoring alignment at all times.

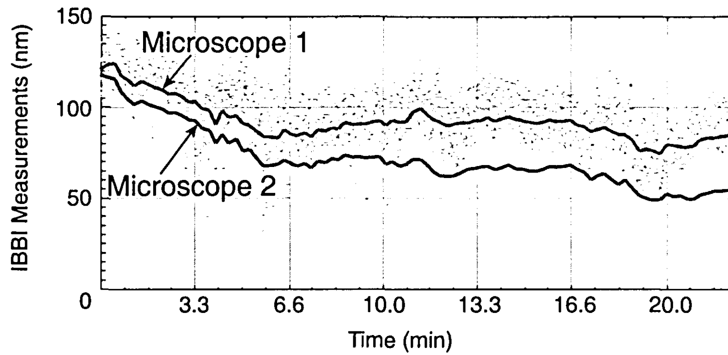

Figure 7-2: Drift trends of two microscopes over a period of 23 minutes.

In Fig. 7-2, IBBI measurement values are plotted for both microscopes over the 23-minute period of the experiment. The fluctuations in the data points are largely due to the flutter just discussed. We now focus on the trend lines, and confirm that the IBBI measurements, on the average, slowly drift relative to the piezo displacements, by up to 70 nm over the 23-minute period. Furthermore, this plot shows that the two IBBI readings drift relative to one another, from ~5 nm to ~30 nm. Because the two marks are separated by 5 mm in the X orientation (as defined in Section 6.4), this corresponds to a rotation of 5 μrad. During the course of the experiment the afternoon sun was shining on the stepper, which could easily cause asymmetrical thermal expansion and the observed drift and rotation. Of course, drifts and other perturbations can be corrected by feedback provided that the time constant of the feedback loop is short compared to the period of the disturbance.

In the NanoStructures Laboratory, the low-power x-ray source implies that we need to maintain alignment over the course of several hours. Figure 7-

3 shows an example of the drift in alignment detected during six hours at a mask-wafer gap of 50 microns. The piezo drives were held stationary, and the output of a single IBBI microscope was monitored for six hours. The relative mask/wafer alignment drifted slowly through about 150 nm, with faster, smaller fluctuations along the way. This data was taken during the night to minimize disturbances from laboratory activities. But clearly, these instabilities are unacceptable for nano-alignment.

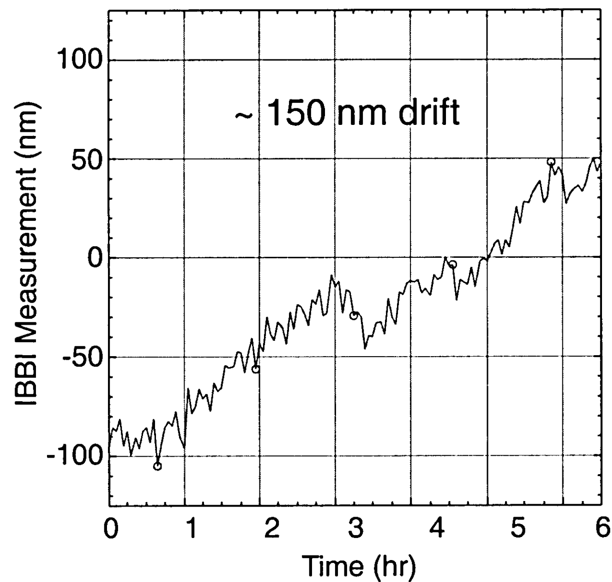

Figure 7-3: 150 nm drift in alignment over six hours.

In the past, one solution to thermal drift, which has been employed at MIT, is to place the mask and wafer in mechanical contact, e.g., set the mask on studs of a few microns. Friction holds mask and wafer together. Alignment must be done when the mask studs are above the wafer. Just before exposure the mask is lowered a few microns to rest on the studs. Lowering the mask

inevitably introduces an unpredictable misalignment of a few nanometers. When the studs are in contact with the wafer the alignment is stable to nanometer levels, but this "hit-or-miss" procedure (on the nanometer scale) is not suitable for future adoption by industry.

Unlike our laboratory, in an industrial setting the environment of a stepper is temperature-controlled to 0.1 C. This certainly will reduce thermal drift, but on the nanometer scale, a temperature change of only 0.1 C can still result in drift of tens of nanometers. Another common practice is to construct the stepper on a granite superstructure to improve structural rigidity and reduce vibrations. Finally, shorter exposure times in industry place less stringent requirements on long-term stability. If a synchrotron is used as the x-ray source, the reduction in exposure time will also reduce the importance of thermal drift during each exposure (planned to be <1 sec). However, this assumes site-by-site alignment. Global alignment is used today to align an entire wafer at the start of a series of runs and relies on the stages to step from one die to the next without checking alignment. Considering that a 12" wafer has ~800 1-cm^2 dies, assuming 16 dies are exposed at a time, this implies that the full wafer requires 50 exposures. At 1 second per exposure, plus an overhead time of 1 second to step from site to site, exposing an entire wafer takes 50x2 = 100 sec = 1.7 minutes. Under these conditions, thermal drift on the order of tens of nanometers is more than likely.

IBBI has demonstrated its usefulness in monitoring alignment, especially during the long x-ray exposures needed in a research environment. It would have a similar usefulness in monitoring the integrity of global alignment in a manufacturing stepper, since it can observe alignment during exposures, thus adding no overhead time. If global alignment was found to be inadequate, using the IBBI measurements for alignment corrections could be justified economically.

7.2 Feedback Stabilization to One Nanometer

Our approach to stepper design is based on continuous monitoring of mask-wafer alignment by IBBI and feeding back correction signals to the piezo drives. We believe this is sounder than approaches such as global alignment, which assumes that measuring the stage position alone will ensure mask-wafer alignment.

The alignment feedback loop consists of the alignment fringes imaged by the microscopes onto CCD cameras, image digitization by a framegrabber and extraction of the alignment condition by image analysis software running under LabVIEW. Depending on the amount of misalignment, correction signals are sent either to the wafer stage or to the piezos in the mask stage. For

misalignments larger than 250 nm, the wafer stage makes corrections (the response time is about 1 second). Smaller corrections are made by the piezo-actuated mask stage (its response time <0.1 sec). Figure 7-4 shows responses of the feedback-controlled system to very large disturbances.

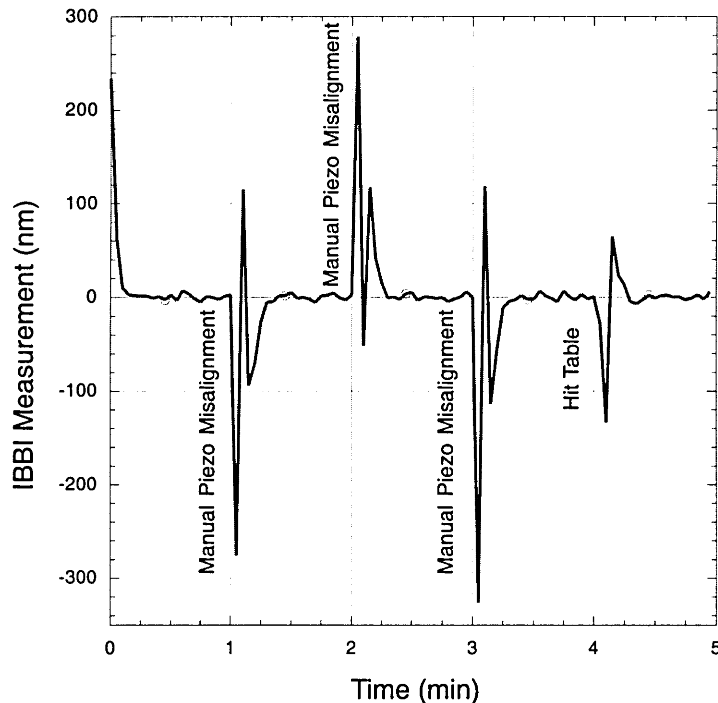

Figure 7-4 Response of feedback system to large misalignments. Disturbances as large as 300 nm resulting from manual displacement of piezos or pounding on the optical table are corrected in less than 15 seconds. (Results are improved sixfold with 300 MHz CPU.)

The feedback software was tested by manually misaligning the mask and observing the corrections made by the feedback system. The system could recover from large displacements in less than 15 seconds (with a 3 second loop time). As can be seen in Fig. 7-4, the system is overcompensating for the misalignment. Since the misalignment is over 250 nm, the wafer stage does the first correction. When the wafer stages have to move, as they do here,

there is the possibility of the feedback system in the wafer stage working at counter purposes to IBBI feedback. Large steps can cause overshoot and the attempt at correction by the feedback system in the stage occurs faster than the loop time of the IBBI algorithm, causing oscillations. Fine-tuning of the algorithm may reduce the overshoot evident in Fig. 7-4. Better performance can be achieved by faster image analysis to reduce the loop time. Small disturbances, however, can be corrected by the piezos in a single move.

The efficacy of feedback in maintaining position (using only the piezos) is illustrated by the experimental results depicted in Fig. 7-5. A six-hour experiment is shown with the IBBI output fed back to control the piezo inputs. Drift was eliminated within a standard deviation of 1.4 nm.

In this experiment the feedback loop had a 3 second time constant[1], which may account for much of the 1.4 nm deviation. With improvement in the algorithm and processor speed this can be reduced further, enabling IBBI to keep up with faster disturbances.

[1] These feedback experiments were done using a computer with a 180 MHz 604e CPU. The loop time with a newer, 300 MHz G3 CPU was reduced by a factor of six.

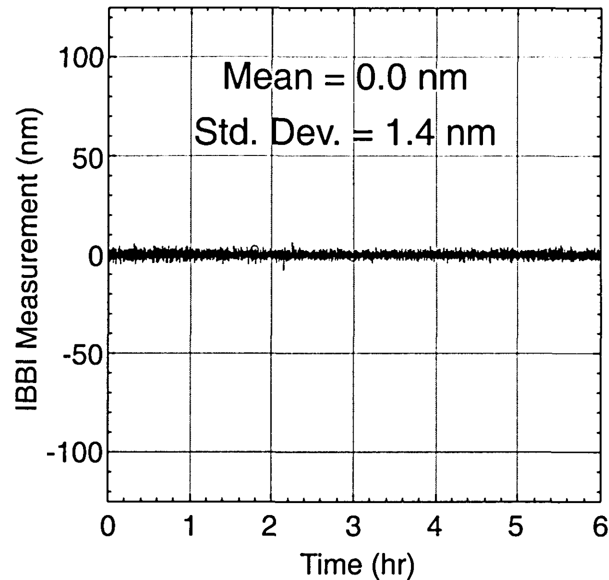

Figure 7-5: Six-hour alignment data with closed-loop operation. Feedback-stabilized IBBI alignment and gapping nullifies effect of thermal/mechanical drift to σ = 1.4 nm. Shorter feedback loop times are expected to improve this result.

Thus, the ability of IBBI to monitor alignment before and during exposure presents the opportunity to close the loop. The choice is between spending ever-increasing amounts of time and capital on heroic engineering efforts to increase the open-loop stability of an aligner, or to continually monitor alignment through the mask, site-by-site, and make whatever corrections are necessary "on the fly." Our contention is that continuous feedback yields higher performance at lower cost, now, and in the future.

Let us end this with a final thought: Imagine if you were driving in the country one day and had to cross a narrow bridge with no guardrails. Now imagine that an earthquake is shaking the bridge. Would you prefer to cross that bridge wearing a blindfold or with your eyes open every inch of the way?

CHAPTER 8:

CONCLUSION AND FUTURE EFFORTS

This thesis has developed a novel alignment scheme based on the sensitivity of interferometry and the virtues of imaging. The primary strengths of IBBI alignment are its spatial-phase-based measurement, its insensitivity to coatings of commonly used process materials such as resist, polysilicon and aluminum, and its off-axis operation, which allows continuous control and stabilization of alignment on the 1 nm level.

The focus of this thesis has been on the development of an experimental x-ray lithography apparatus, and the verification of the capabilities of IBBI alignment. The series of tests that were conducted showed the consistency of two completely separate and distinct IBBI measurement tools observing the same alignment mark, the scale of IBBI being within 1.5% of an external

reference over a wide range, and the ability to feedback-stabilize alignment to within σ=1.4 nm over six hours.

The results illustrated in this thesis may be described as encouraging but are by no means the final evidence of the efficacy of IBBI. The proof is in the pudding, so to speak, which in the case of IBBI means fabrication of working devices with aligned feature sizes on the order of a few tens of nanometers.

To accomplish this challenging task, several further things must be accomplished. As discussed in Chapter 6, the magnification produced by an x-ray point source was observed by IBBI, and found to agree with the predicted value within the uncertainty of the gap measurement. In order to have alignment to 1 nm over the entire surface of a mask at a finite gap, we must control the mask-wafer gap to better than 0.1 μm, and locate the mask-source axis to better than 50 microns. We are presently making progress on both of these fronts, and plan to test the alignment first on a dual-gate n-MOS transistor with 50 nm gate widths.

Other future efforts should be made to reduce the size of the alignment mark and increase the efficiency of illumination. At the moment we are using 12x optics and 100 micron marks. Theoretical analysis has shown that the magnification we are using is more than adequate - in fact, it could be reduced by a factor of three with the present mark size without adversely affecting the

detectivity of IBBI. Alternatively, the mark size could be reduced by 3x with the same microscopes. With narrowing kerf widths, it will likely be desirable in the future to reduce the mark size.

On the hardware side, we can retain high accuracy with smaller marks only if the image noise can be reduced. This will mean replacing the analog output cameras with digital output cameras having higher bit-depths. At the present time, 10 and 16-bit digital cameras are available. The output of these cameras should be channeled directly into a DSP board, thus bypassing the overhead of transferring the images over the computer bus and the inaccuracies introduced by the D-A and A-D conversions.

As for the light source, we do not consider the multi-line argon laser to be the ideal light source; it is merely an expedient solution. Work to increase the efficiency of IBBI will progress in concert with investigations of alternate light sources. Possible candidates include superluminescent diodes, xenon discharge lamps, etc., which will also make the system cheaper. The new light source should have more lines, and be shifted towards the red to increase the viewing angle.

The most obvious way to increase the efficiency is to remove the beamsplitter from the microscope. This will double the efficiency on both input and imaging paths. Thus a 4x improvement can be seen without resorting

to a change in the magnification. Moreover, this will reduce bothersome scattering of the input light beam, which necessitates additional complexity in the microscope alignment procedures.

The in-house system can also benefit from minor improvements:

- Design and construct a smaller helium enclosure for a faster purge rate and reduced helium consumption.
- Increase the hole diameter of the viewport to increase the exposure area.
- Reduce the source-mask distance to decrease the exposure time.

Appendix A:

Operation of Exposure System

The operation of Head 4 exposure is as follows. Open the "Head 4 Control" LabVIEW program (see Appendix B for details). Click the arrow to run the program. Click the button called "HELIUM" to turn on the solenoid allowing helium flow. Go in the chase and open the valve on the helium tank. Check that output pressure is at 10 PSI. Turn on the DeltaV oxygen sensor. Press the button to select range=0-1000. The LCD display will initially show "1123" or thereabouts. This is the maximum reading possible (in ppm O_2). At this point there is no helium flowing into the helium chamber. Check the Omega differential pressure meter (red LED display). The overpressure inside the chamber should be near zero. The display is calibrated in terms of milli-PSI over atmospheric pressure. The sensor has two inputs, one for room air and the other from inside the helium box. The difference between these is

displayed. Overpressure of the helium box will burst the 1.5 micron thick silicon nitride vacuum window separating the helium ambient from vacuum in the x-ray source.

Helium flow going into the top of the box must be balanced with vacuum pulling air out of the bottom of the box. Helium, being lighter, rises to the top of the box and air settles to the bottom. First open the vacuum valve leading out of the oxygen controller. This can be at its maximum of 5 SCCM for the oxygen purge. Using the ball-type flow control knob (KING flow controller with integral readout) slowly increase the helium flow while observing the overpressure. Do not exceed 90 milli-PSI overpressure. This corresponds to a helium flow of about 15 SCCM. Wait until the air is purged. Typically this takes about 15 minutes. After about 10 minutes the reading on the oxygen sensor will start decreasing. When the oxygen content has gone below 200 ppm the x-ray exposure may begin. During the exposure a small "maintenance" helium flow is required. Bring the flow through the oxygen sensor down to 0.5 SCCM and the helium flow to about 8 SCCM.

Now for the fun part: Turn on the power to the high voltage supply. Set the duration you want for the exposure in the LabVIEW front panel. Press the "START" button on the LabVIEW panel to enable the run. Press the "HV ON" button on the high voltage source to start the x-rays. You will hear a sound emanating from the x-ray source that is ramped in frequency, not unlike the

sound of a turbine spooling up. Apparently this is due to a resonant frequency of the vacuum cube. The frequency increases linearly with the voltage going to the source. The filament will glow bright purple. Now you may go home and wait for a few hours for your run to finish.

Appendix B:

Detection and Control Software

All software operating the exposure system and the feedback-controlled alignment and gapping is written by the author in LabVIEW. As such it is a graphic programming language, which uses a logic structure depending on the use of frames for WHILE and FOR loops, and CASE and SEQUENCE structures. This makes the description of the software in a paper more difficult since you must, in essence, translate a multi-layered logic structure into a two-dimensional representation. We will attempt to convey the meaning of the code in the following pages by means of a series of snapshots of the LabVIEW structures. The function of each vi should be apparent to someone versed in LabVIEW. Questions may be directed to euclid@nano.mit.edu.

Closed-Loop Alignment Control:

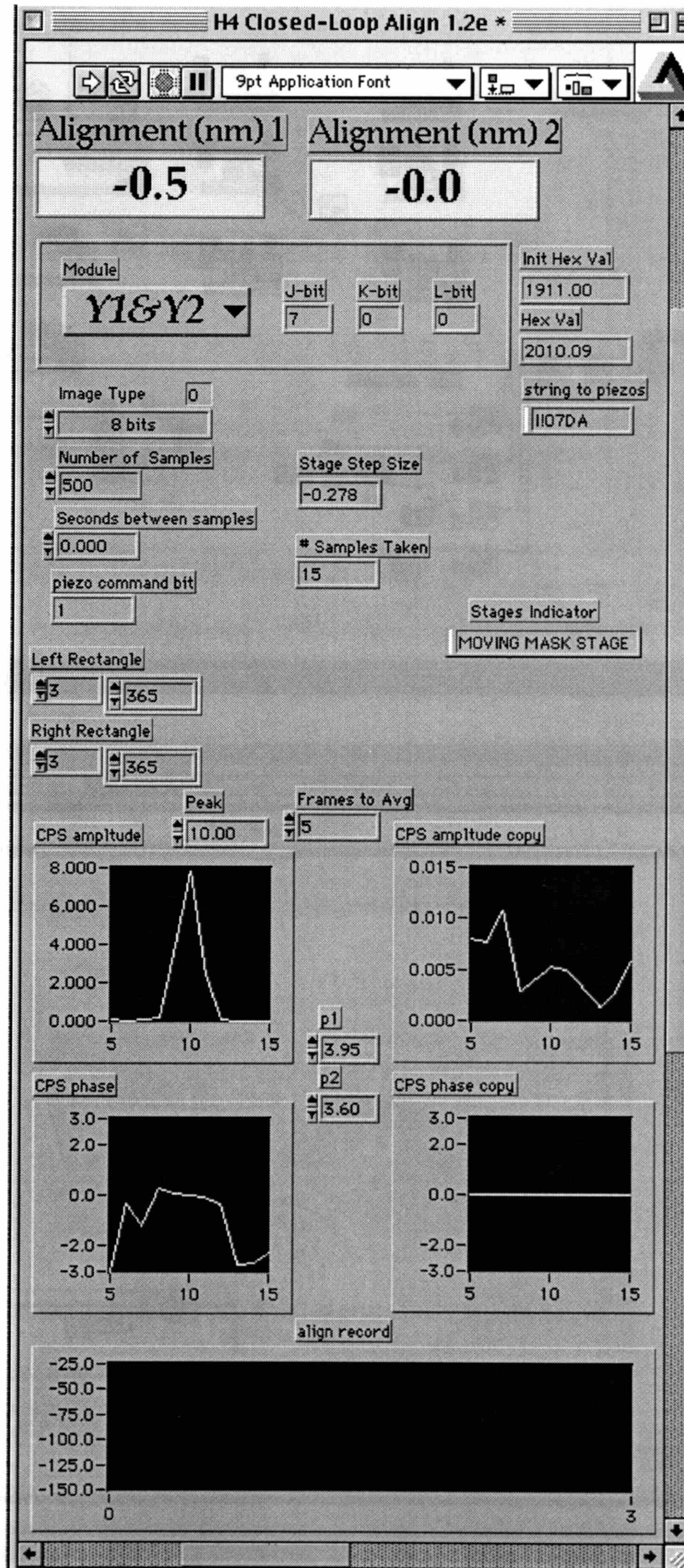

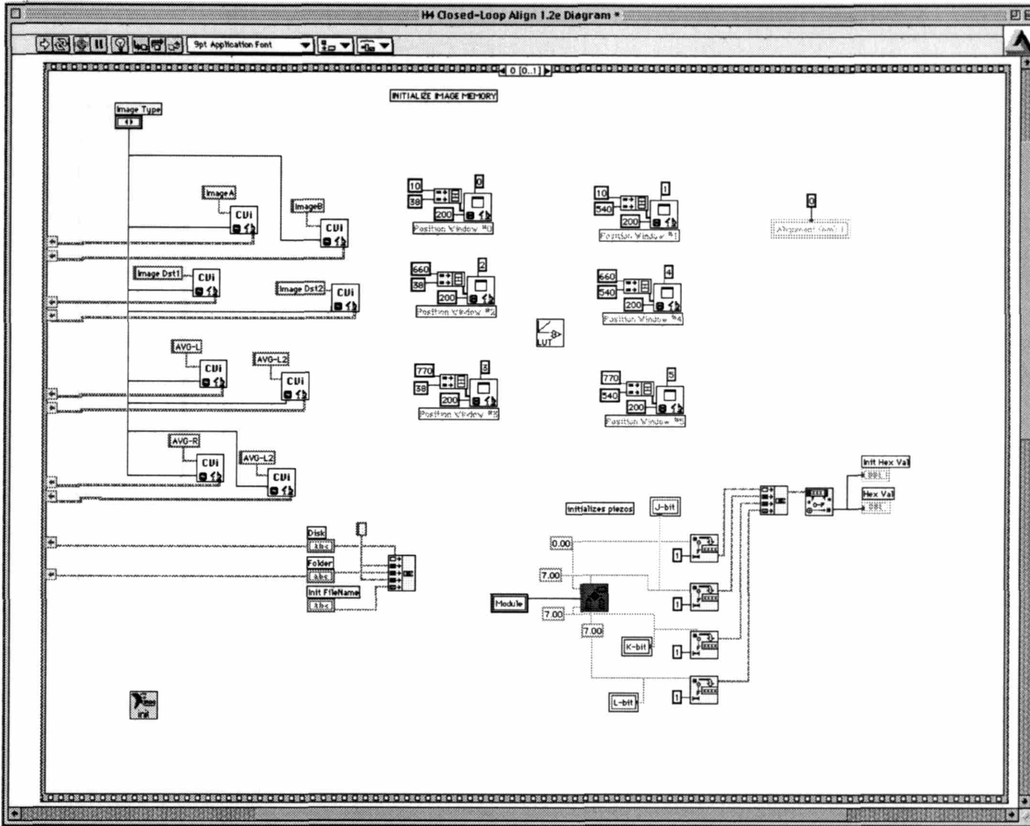
H4 Closed-Loop Align 1.2e Diagram
INITIALIZE IMAGE MEMORY
Image Type
ImageA
ImageB
Image Dst1
Image Dst2
AVG-L
AVG-L2
AVG-R
Disk
Folder
Init FileName
Initializes piezos
Module
Init Hex Val
Hex Val

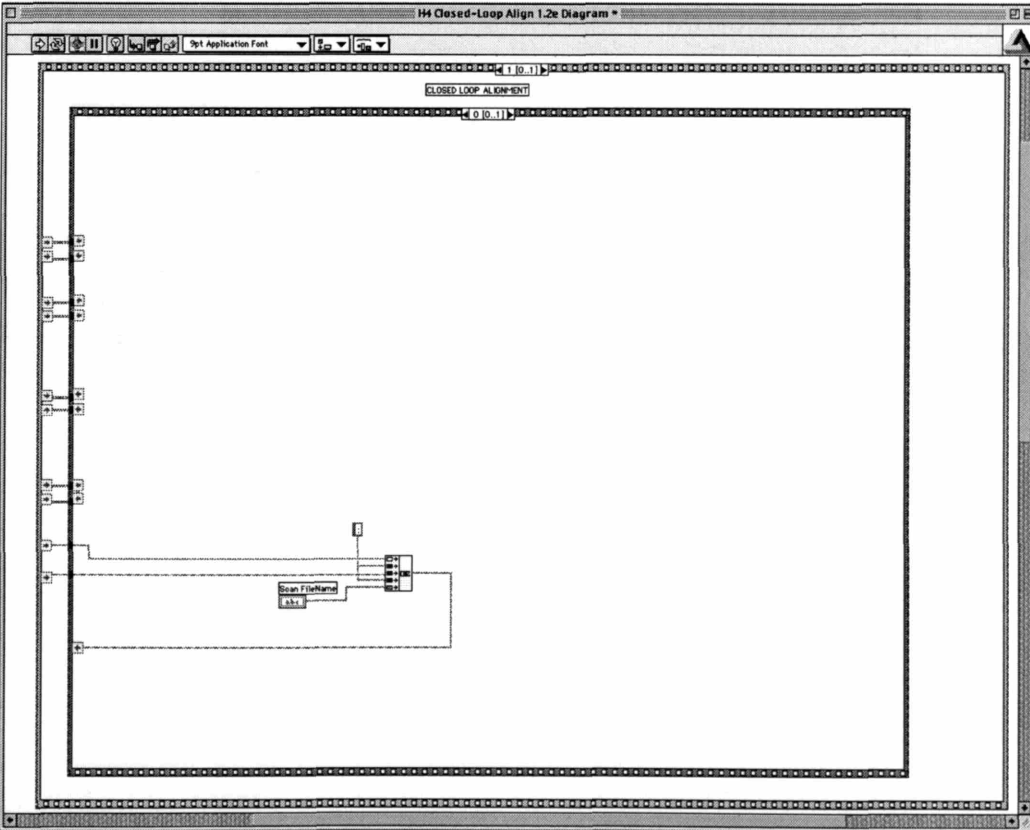
H4 Closed-Loop Align 1.2e Diagram
CLOSED LOOP ALIGNMENT
Scan FileName

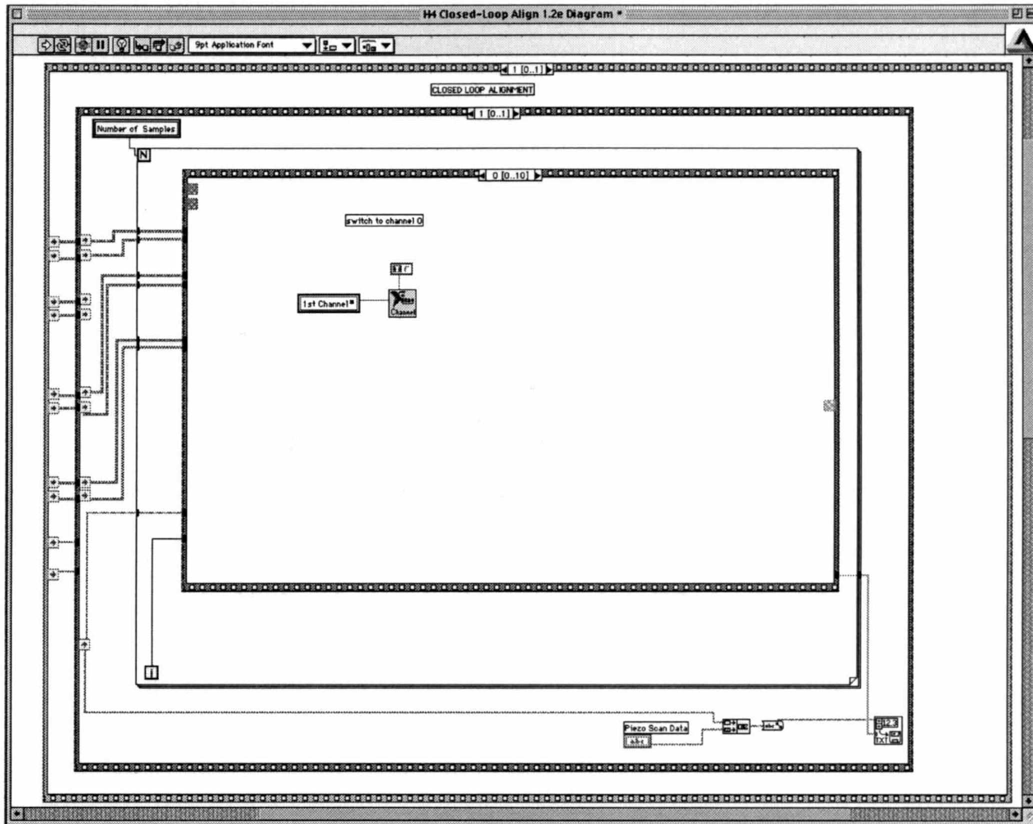
H4 Closed-Loop Align 1.2e Diagram *
9pt Application Font
CLOSED LOOP ALIGNMENT
Number of Samples
switch to channel 0
1st Channel#
Piezo Scan Data

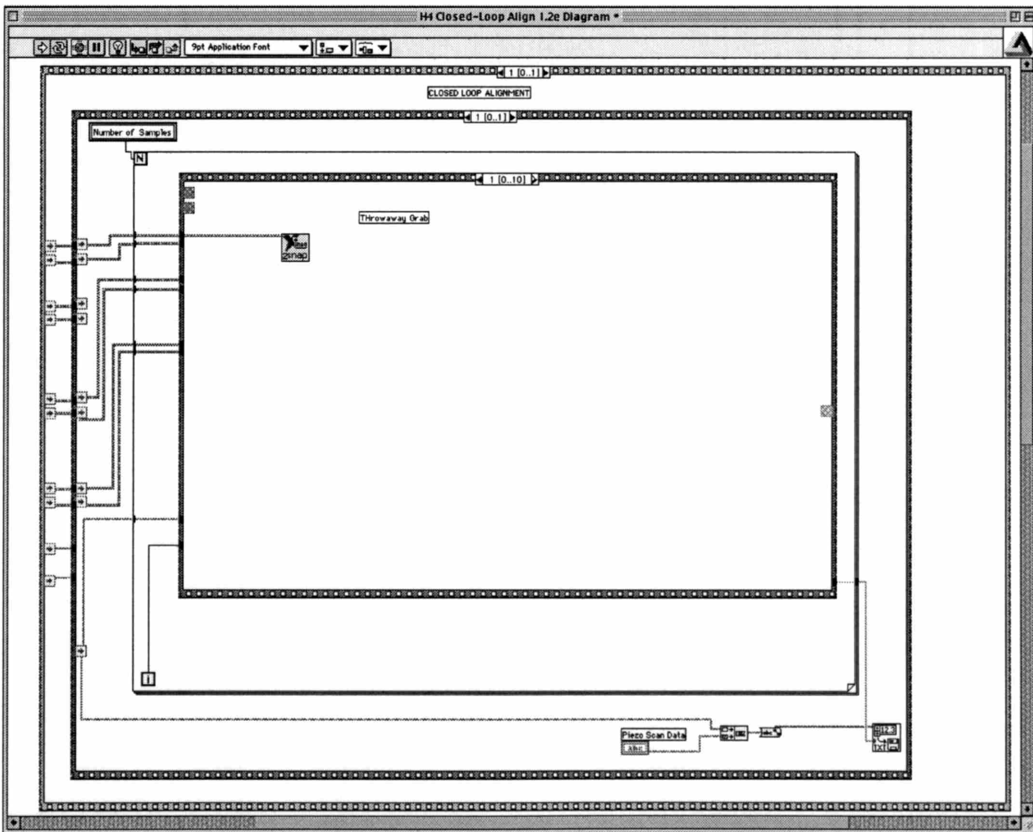
H4 Closed-Loop Align 1.2e Diagram *
9pt Application Font
CLOSED LOOP ALIGNMENT
Number of Samples
THrowaway Grab
snap
Piezo Scan Data

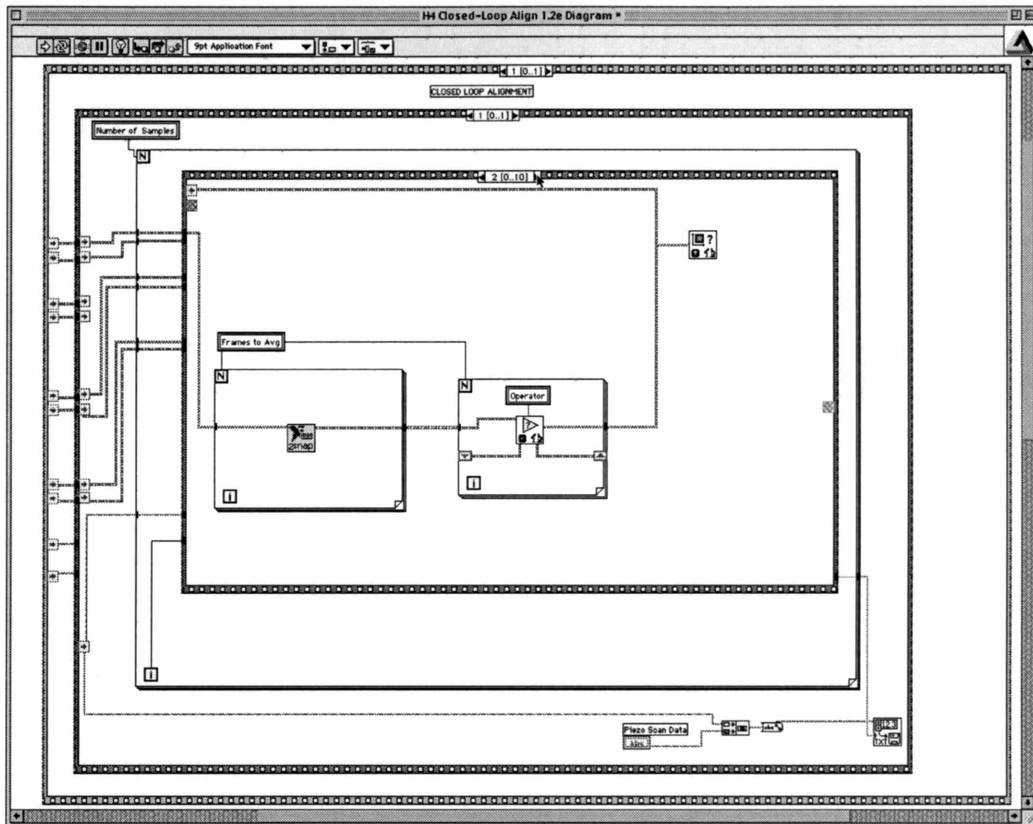
H4 Closed-Loop Align 1.2e Diagram *
9pt Application Font
CLOSED LOOP ALIGNMENT
Number of Samples
Frames to Avg
Operator
Piezo Scan Data

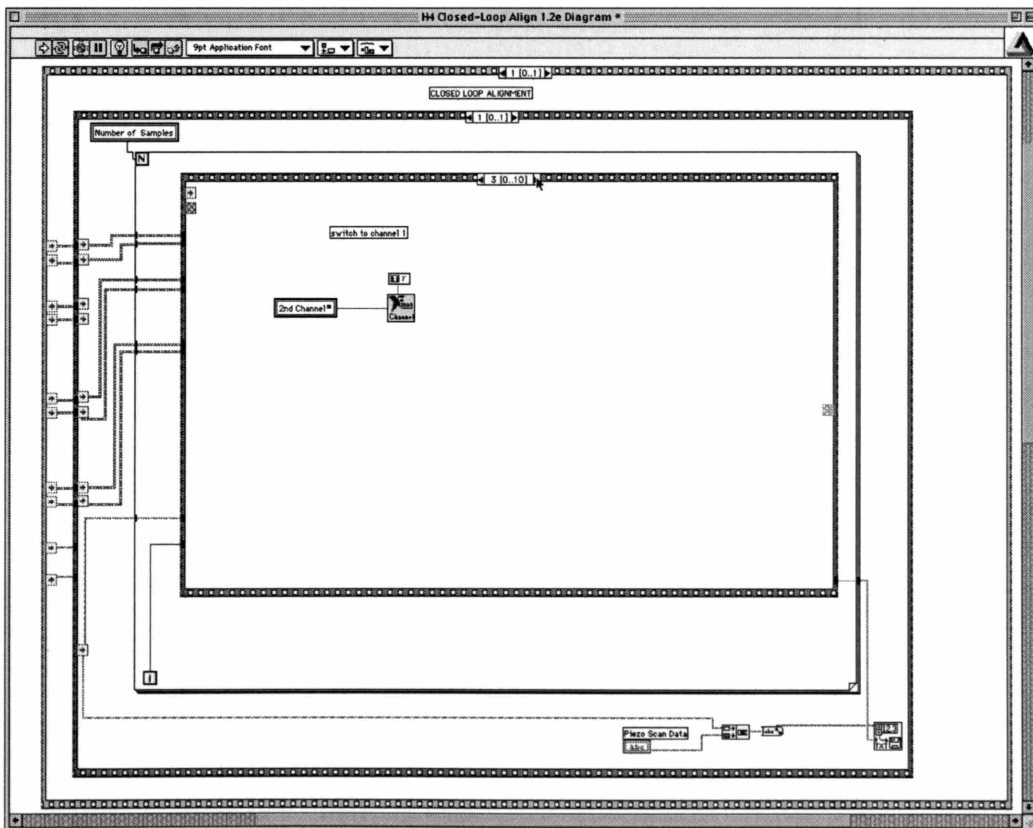
H4 Closed-Loop Align 1.2e Diagram *
9pt Application Font
CLOSED LOOP ALIGNMENT
Number of Samples
switch to channel 1
2nd Channel*
Piezo Scan Data

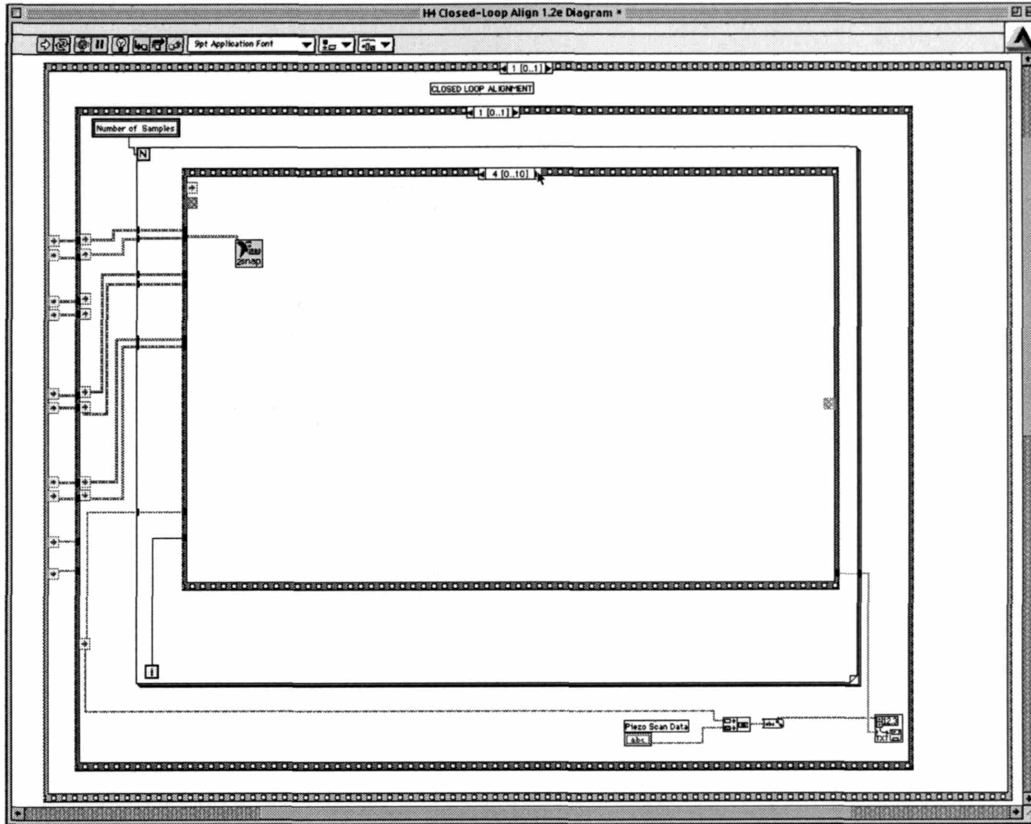
H4 Closed-Loop Align 1.2e Diagram *
9pt Application Font
CLOSED LOOP ALIGNMENT
Number of Samples
Piezo Scan Data

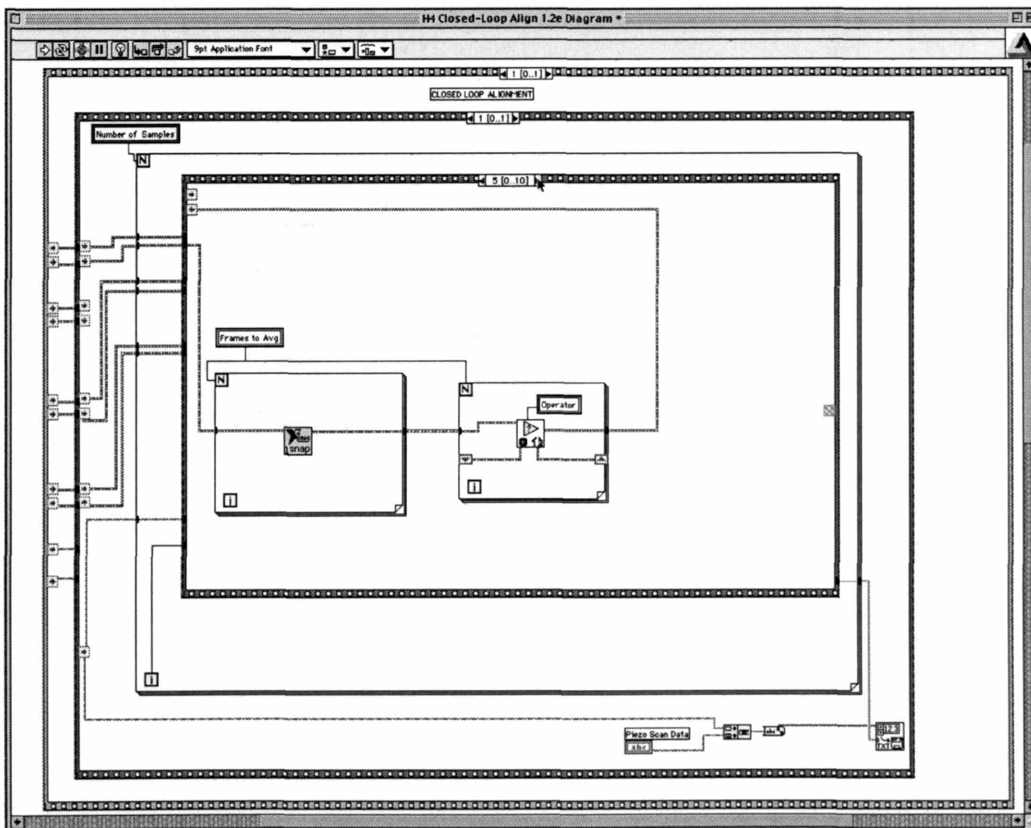
H4 Closed-Loop Align 1.2e Diagram *
9pt Application Font
CLOSED LOOP ALIGNMENT
Number of Samples
Frames to Avg
Operator
Piezo Scan Data

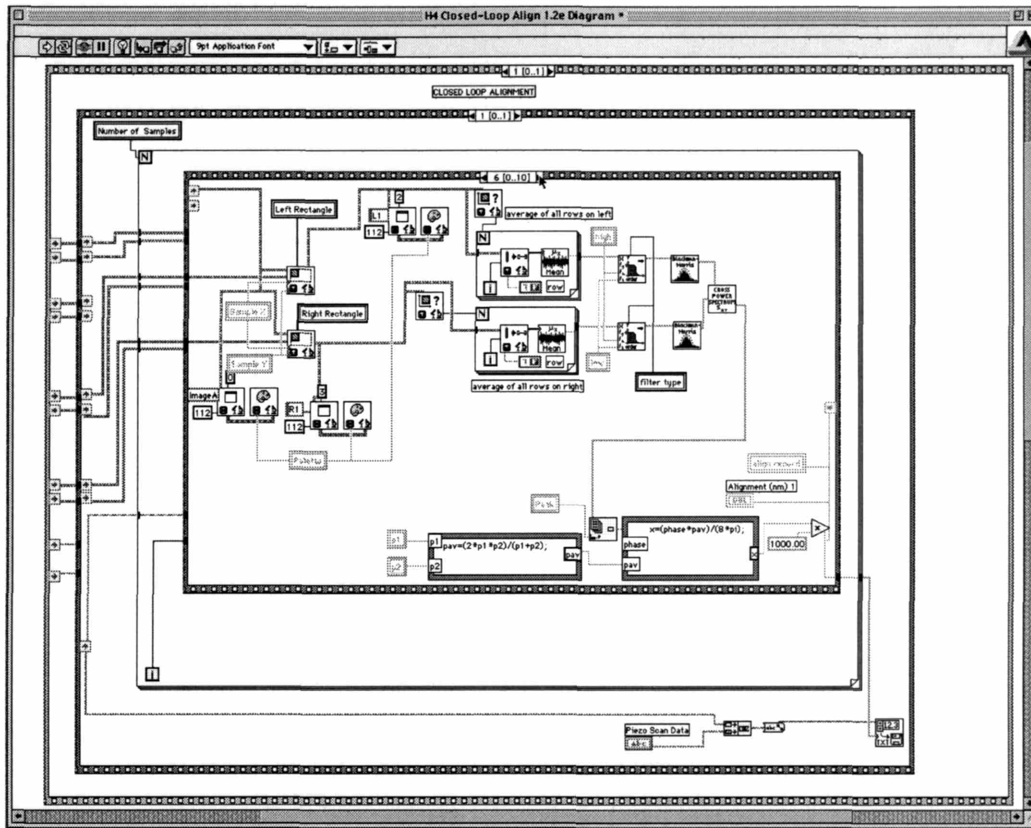
H4 Closed-Loop Align 1.2e Diagram *
9pt Application Font
CLOSED LOOP ALIGNMENT
Number of Samples
Left Rectangle
Right Rectangle
average of all rows on left
average of all rows on right
filter type
ImageA
Alignment (nm) 1
pav=(2*p1*p2)/(p1+p2);
x=(phase*pav)/(8*pi);
phase
pav
1000.00
Piezo Scan Data

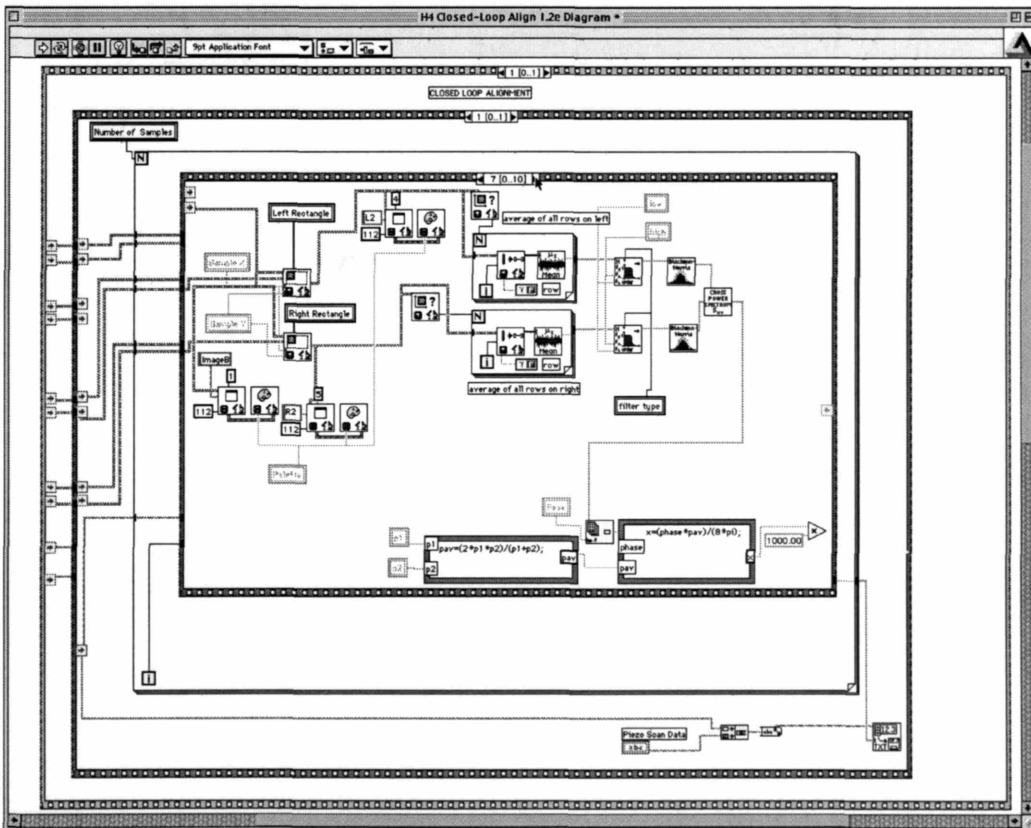
H4 Closed-Loop Align 1.2e Diagram *
9pt Application Font
CLOSED LOOP ALIGNMENT
Number of Samples
Left Rectangle
Right Rectangle
average of all rows on left
average of all rows on right
filter type
ImageB
pav=(2*p1*p2)/(p1+p2);
x=(phase*pav)/(8*pi);
phase
pav
1000.00
Piezo Scan Data

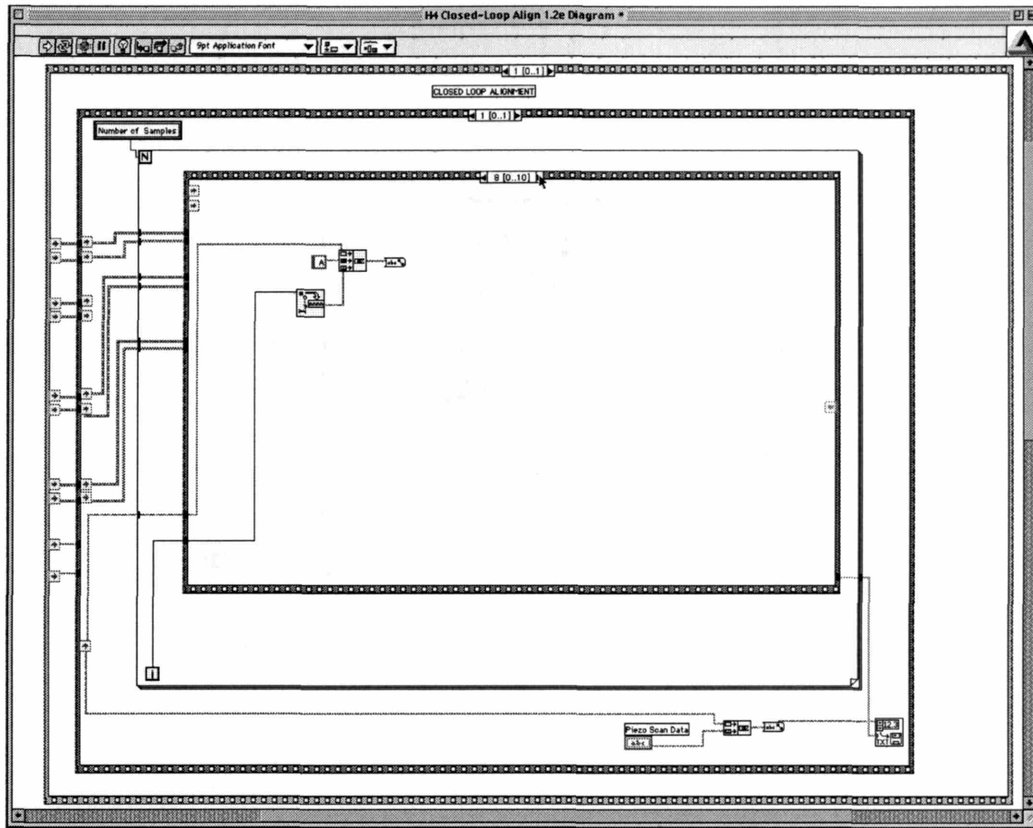
H4 Closed-Loop Align 1.2e Diagram *
9pt Application Font
1 [0..1]
CLOSED LOOP ALIGNMENT
Number of Samples
8 [0..10]
Piezo Scan Data

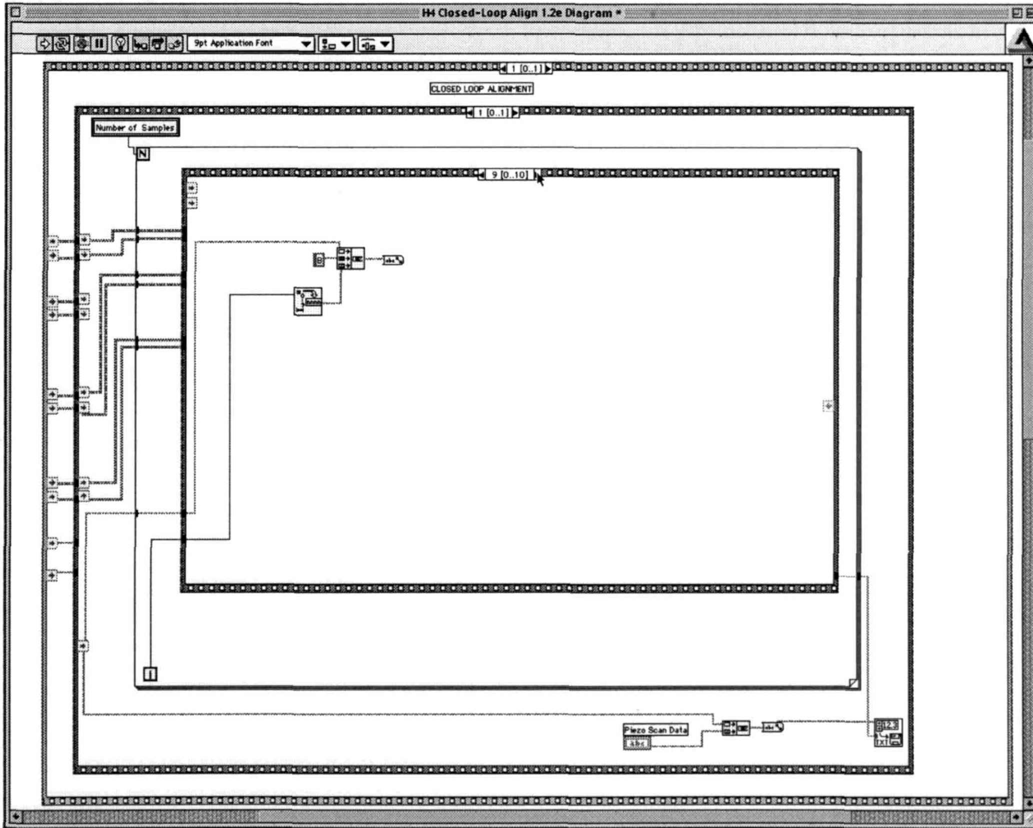
H4 Closed-Loop Align 1.2e Diagram *
9pt Application Font
1 [0..1]
CLOSED LOOP ALIGNMENT
Number of Samples
9 [0..10]
Piezo Scan Data

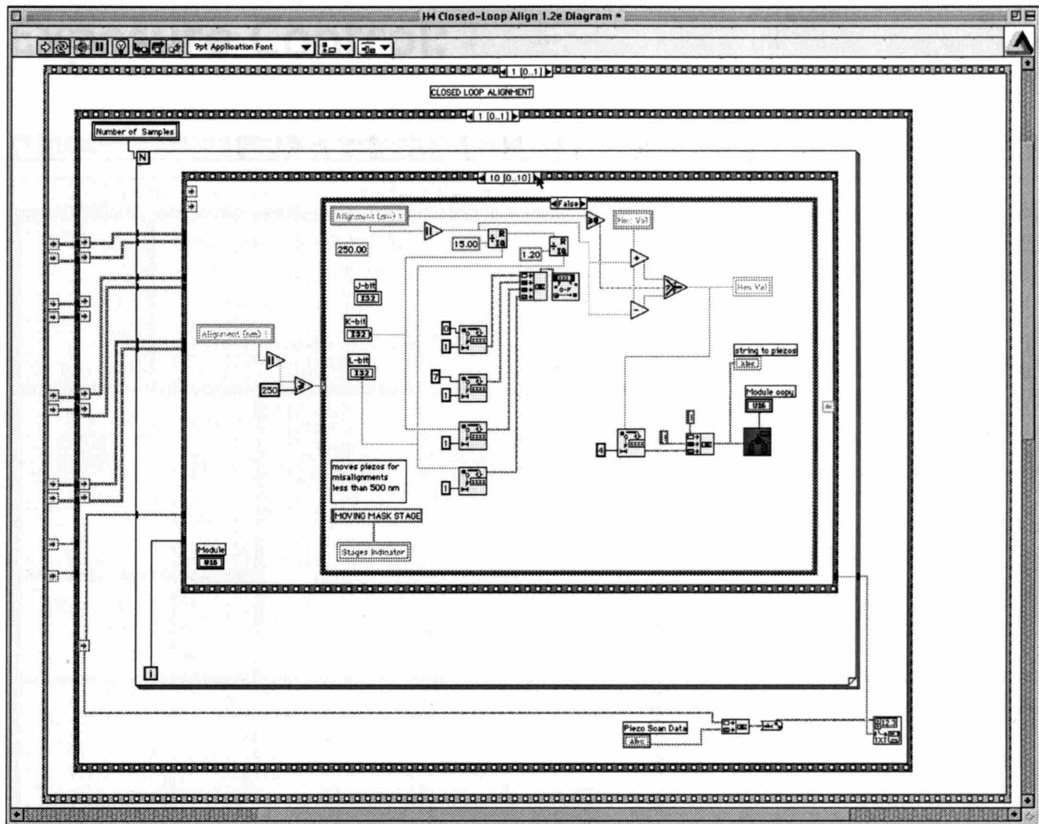
H4 Closed-Loop Align 1.2e Diagram
9pt Application Font
CLOSED LOOP ALIGNMENT
Number of Samples
250.00
15.00
1.20
Hex Val
string to piezos
Module copy
moves piezos for
misalignments
less than 500 nm
MOVING MASK STAGE
Stages Indicator
Module
Piezo Scan Data

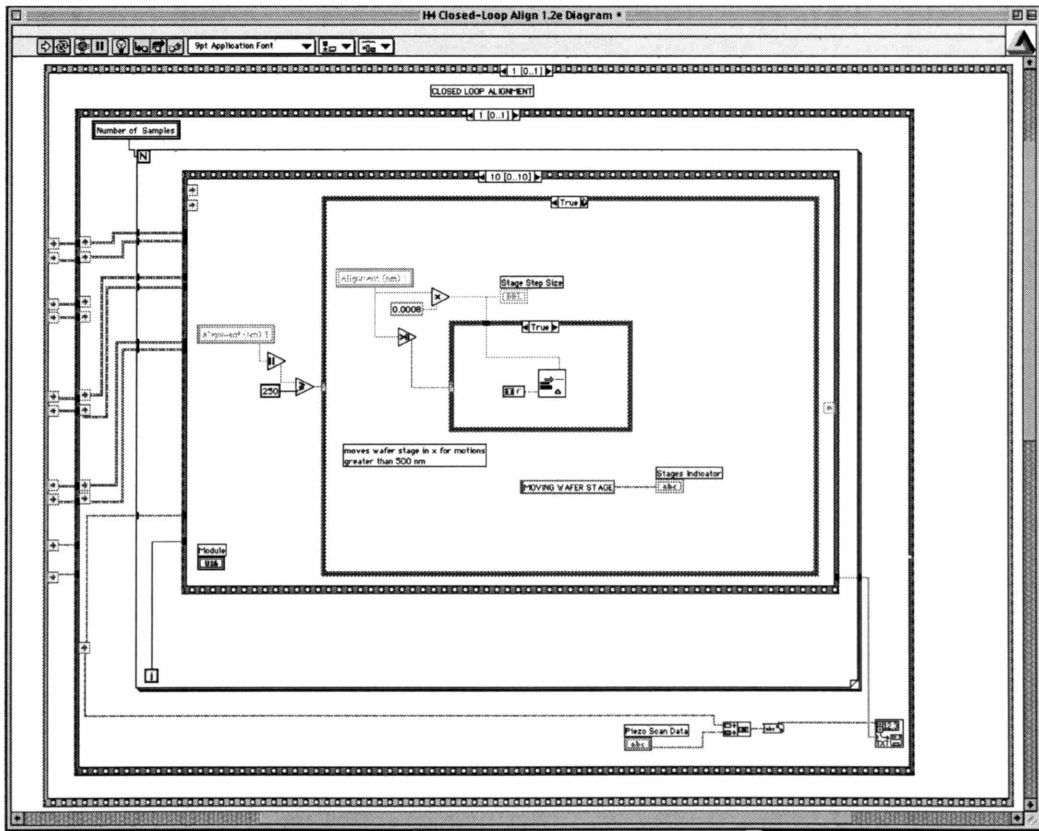
H4 Closed-Loop Align 1.2e Diagram
9pt Application Font
CLOSED LOOP ALIGNMENT
Number of Samples
Stage Step Size
0.0008
moves wafer stage in x for motions
greater than 500 nm
MOVING WAFER STAGE
Stages Indicator
Module
Piezo Scan Data

Exposure Control:

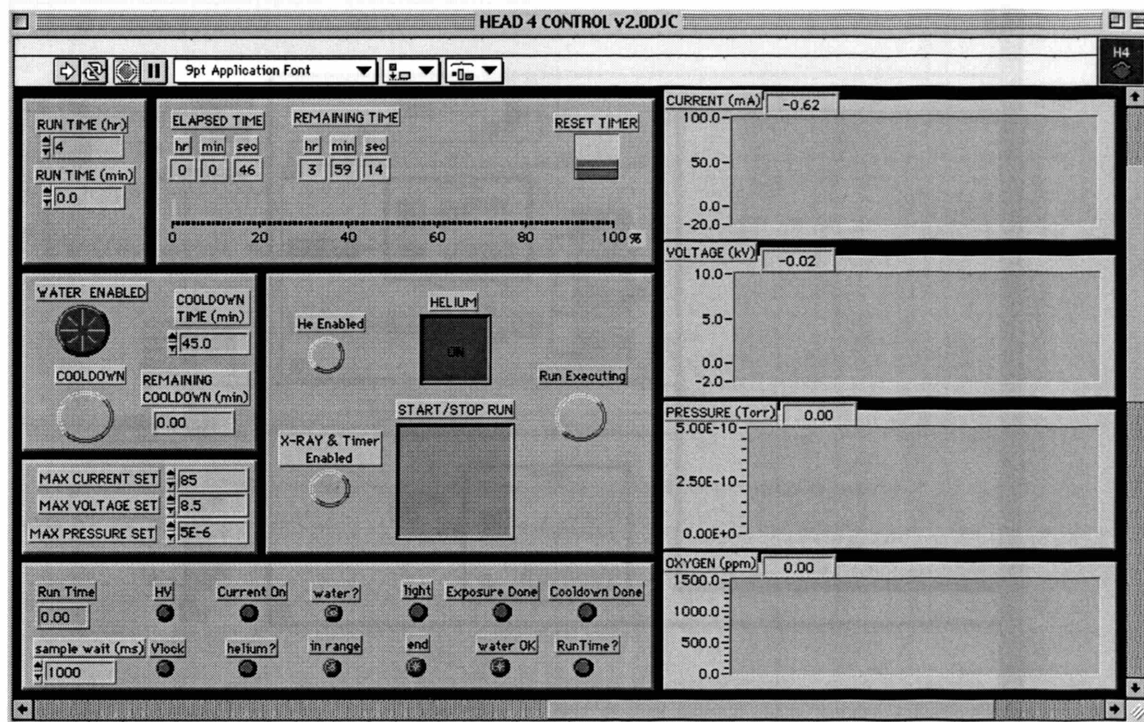

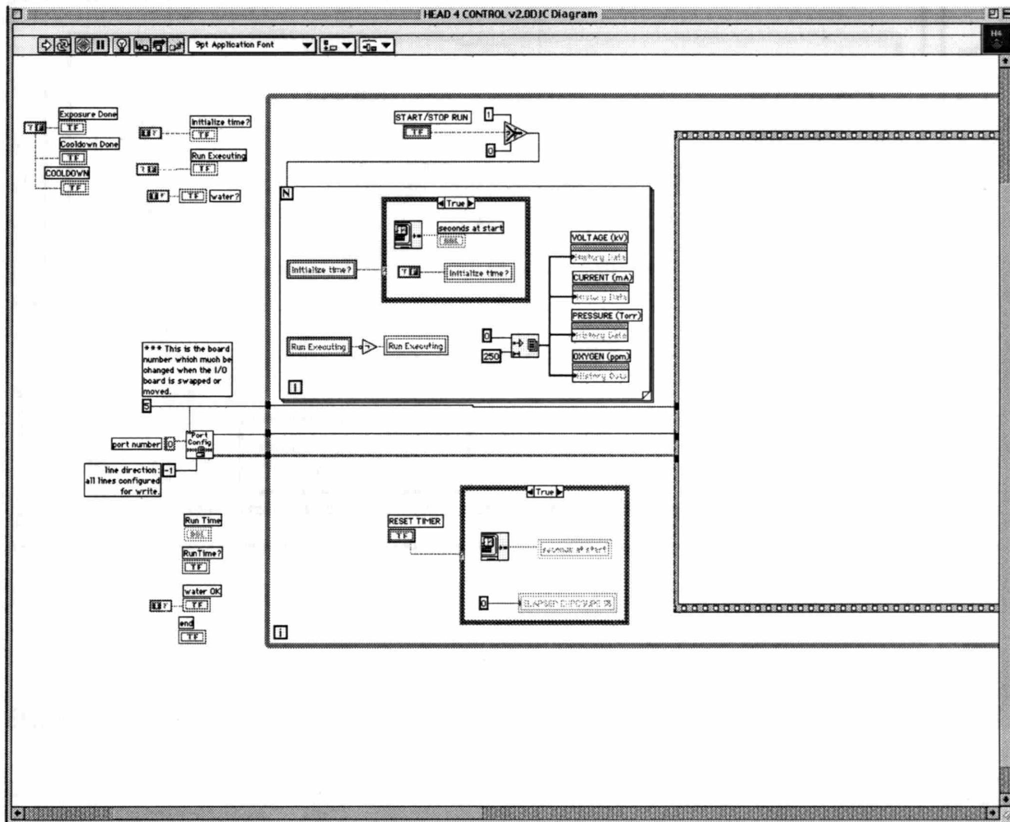
HEAD 4 CONTROL v2.0DJC Diagram
9pt Application Font
Exposure Done
Cooldown Done
COOLDOWN
Initialize time?
Run Executing
water?
START/STOP RUN
True
seconds at start
Initialize time?
Initialize time?
VOLTAGE (kV)
CURRENT (mA)
PRESSURE (Torr)
OXYGEN (ppm)
Run Executing
Run Executing
250
*** This is the board number which much be changed when the I/O board is swapped or moved.
port number
Port Config
line direction: all lines configured for write.
Run Time
RunTime?
water OK
end
RESET TIMER
True

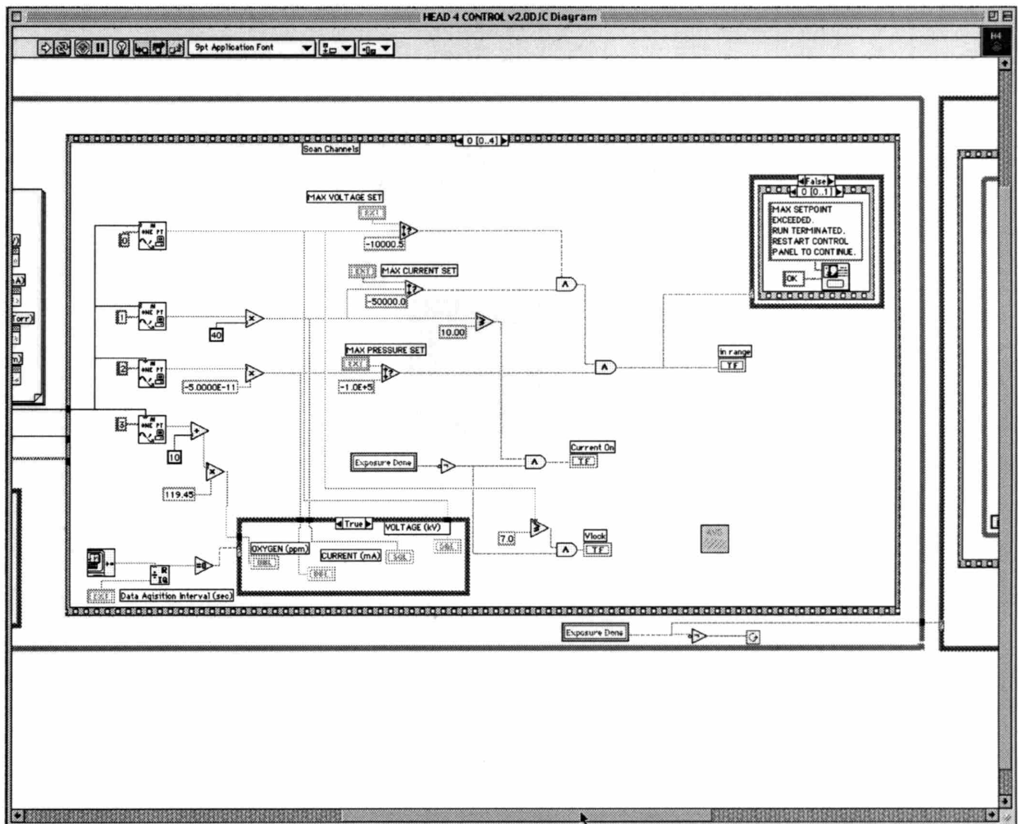

HEAD 4 CONTROL v2.0DJC Diagram
9pt Application Font
0 [0..4]
Scan Channels
MAX VOLTAGE SET
-10000.5
MAX CURRENT SET
-50000.0
10.00
MAX PRESSURE SET
-1.0E+5
-5.0000E-11
40
10
119.45
False
0 [0..1]
MAX SETPOINT EXCEEDED. RUN TERMINATED. RESTART CONTROL PANEL TO CONTINUE.
OK
In range
Current On
Exposure Done
True
VOLTAGE (kV)
OXYGEN (ppm)
CURRENT (mA)
7.0
Vlock
Data Aqisition Interval (sec)
Exposure Done

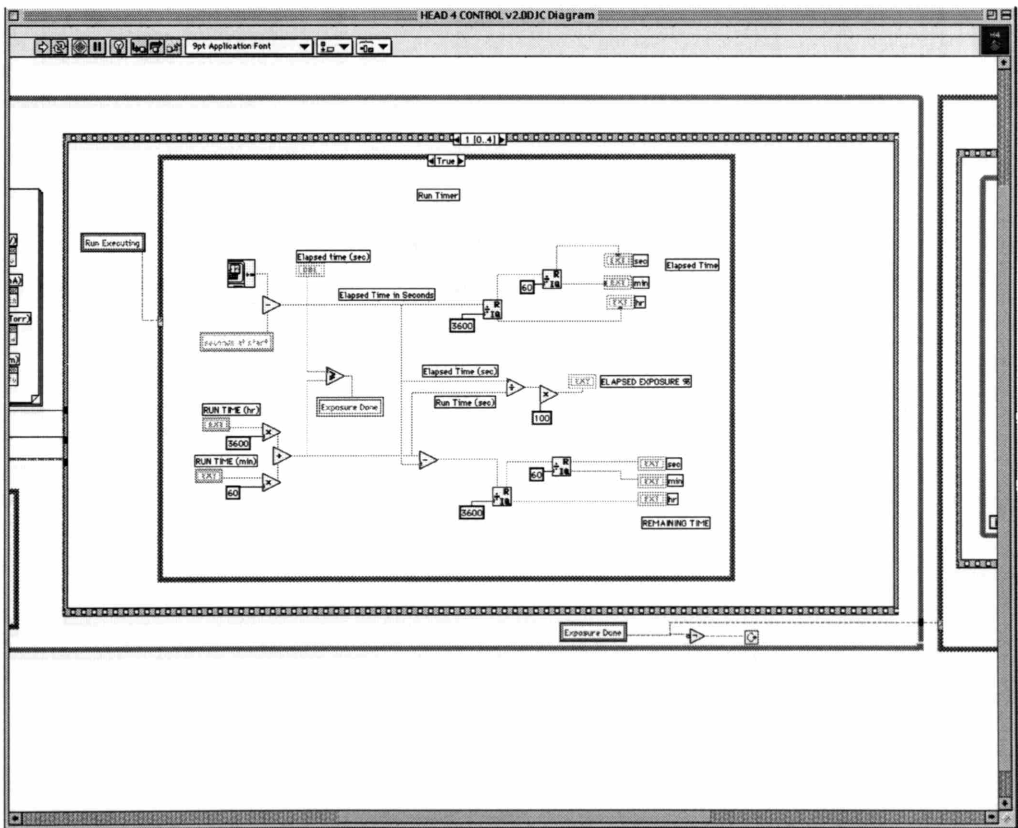

HEAD 4 CONTROL v2.0DJC Diagram
9pt Application Font
1 [0..4]
True
Run Timer
Run Executing
Elapsed time (sec)
Elapsed Time in Seconds
60
3600
sec
min
hr
Elapsed Time
Elapsed Time (sec)
Run Time (sec)
ELAPSED EXPOSURE %
100
Exposure Done
RUN TIME (hr)
3600
RUN TIME (min)
60
60
3600
sec
min
hr
REMAINING TIME
Exposure Done

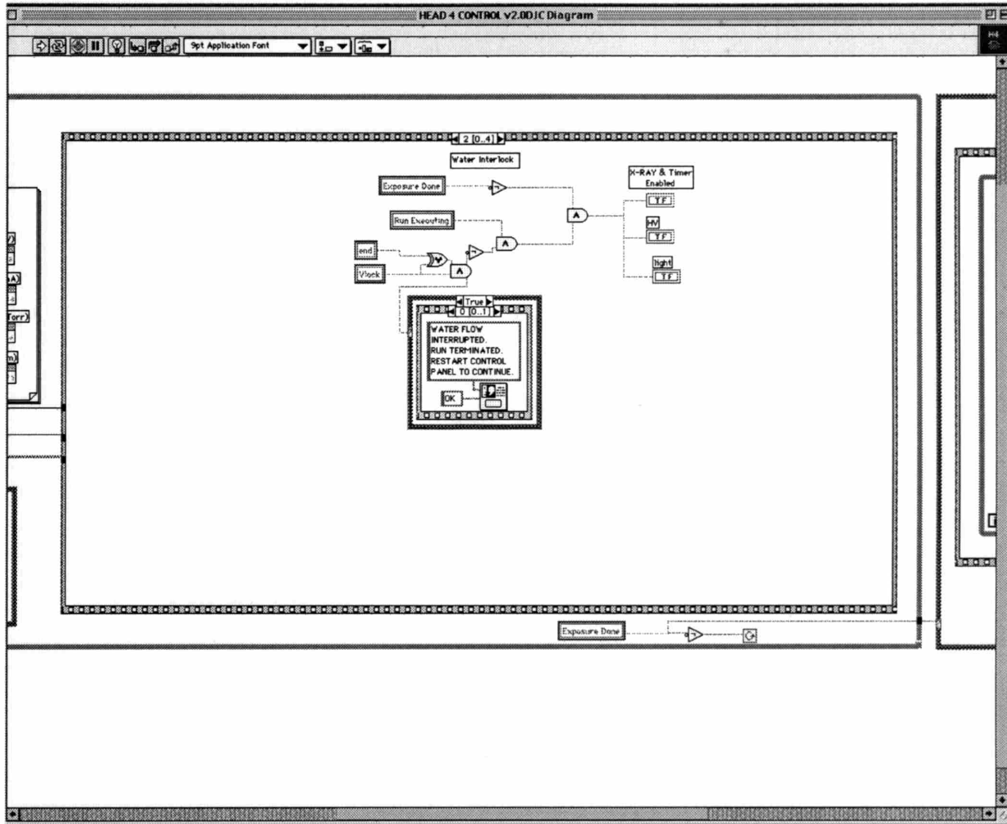
HEAD 4 CONTROL v2.0DJC Diagram
9pt Application Font
Water Interlock
Exposure Done
Run Executing
end
Vlock
X-RAY & Timer Enabled
HV
light
WATER FLOW INTERRUPTED. RUN TERMINATED. RESTART CONTROL PANEL TO CONTINUE.
OK
Exposure Done

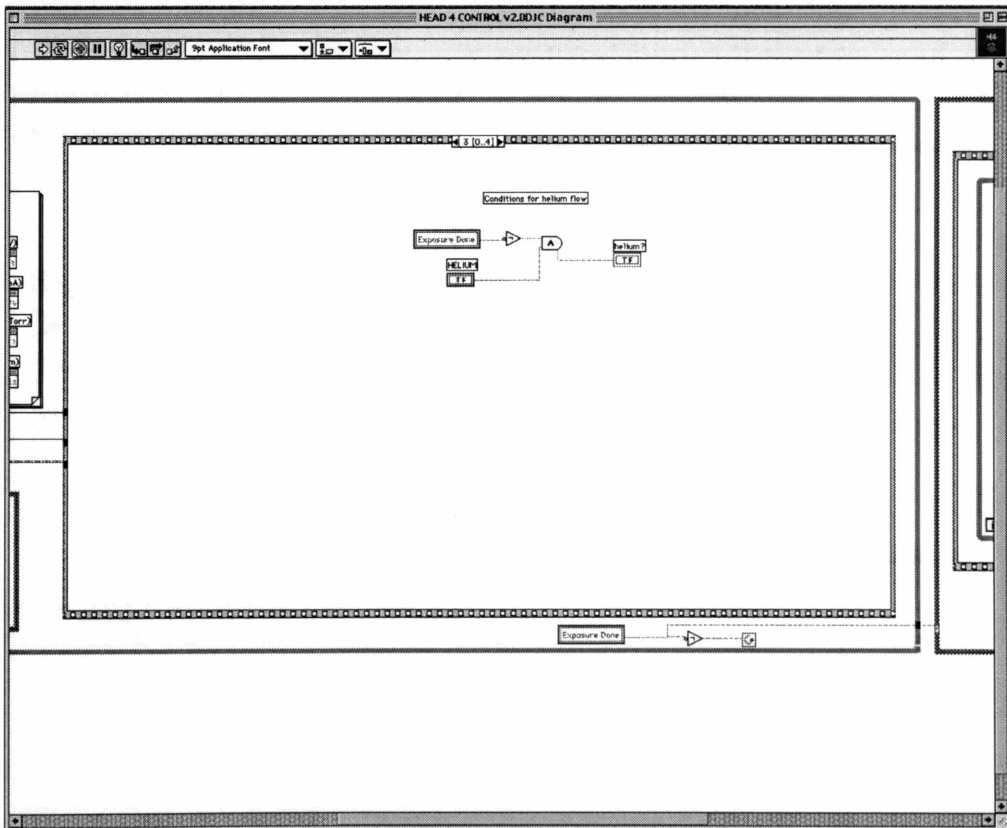
HEAD 4 CONTROL v2.0DJC Diagram
9pt Application Font
Conditions for helium flow
Exposure Done
HELIUM
helium?
Exposure Done

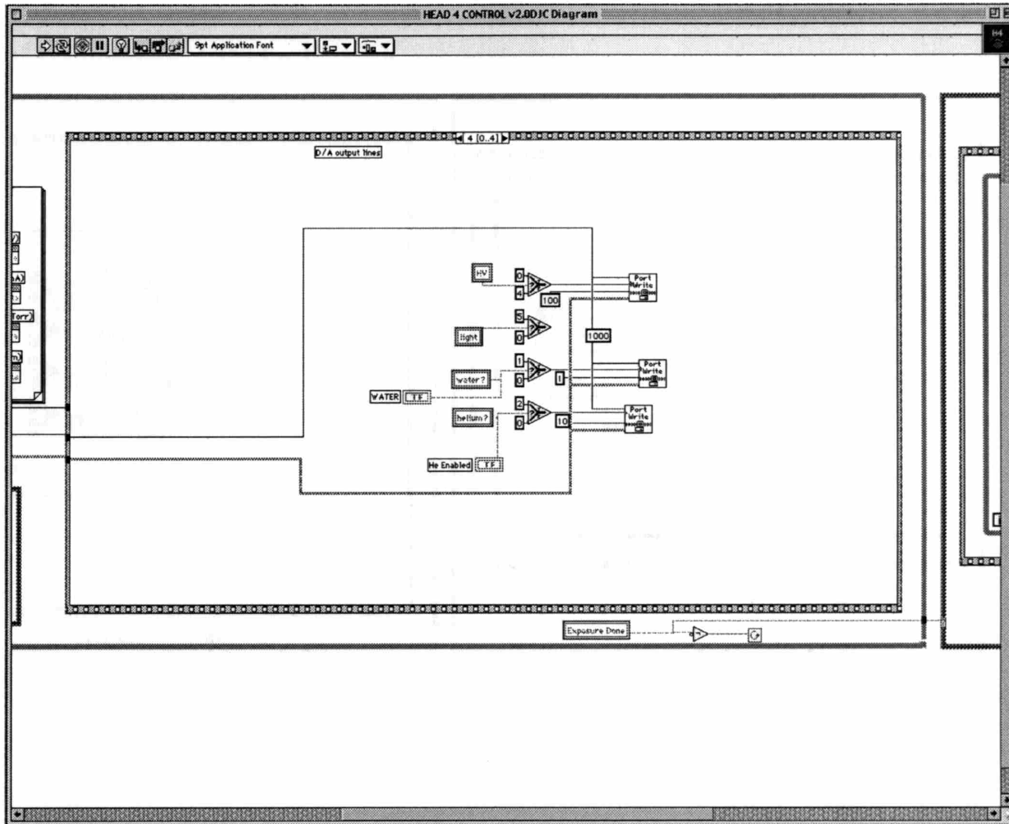
HEAD 4 CONTROL v2.0DJC Diagram
9pt Application Font
D/A output lines
HV
light
water?
WATER
helium?
He Enabled
100
1000
1
10
Port Write
Exposure Done

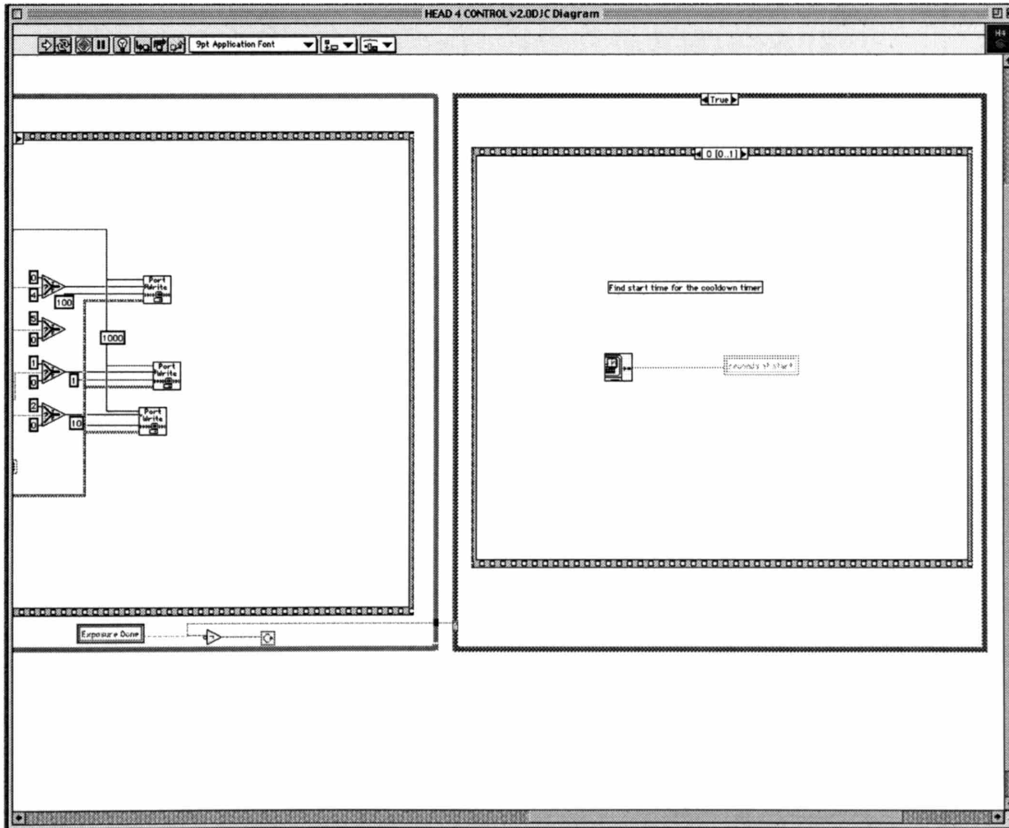
HEAD 4 CONTROL v2.0DJC Diagram
9pt Application Font
True
Find start time for the cooldown timer
100
1000
1
10
Port Write
Exposure Done

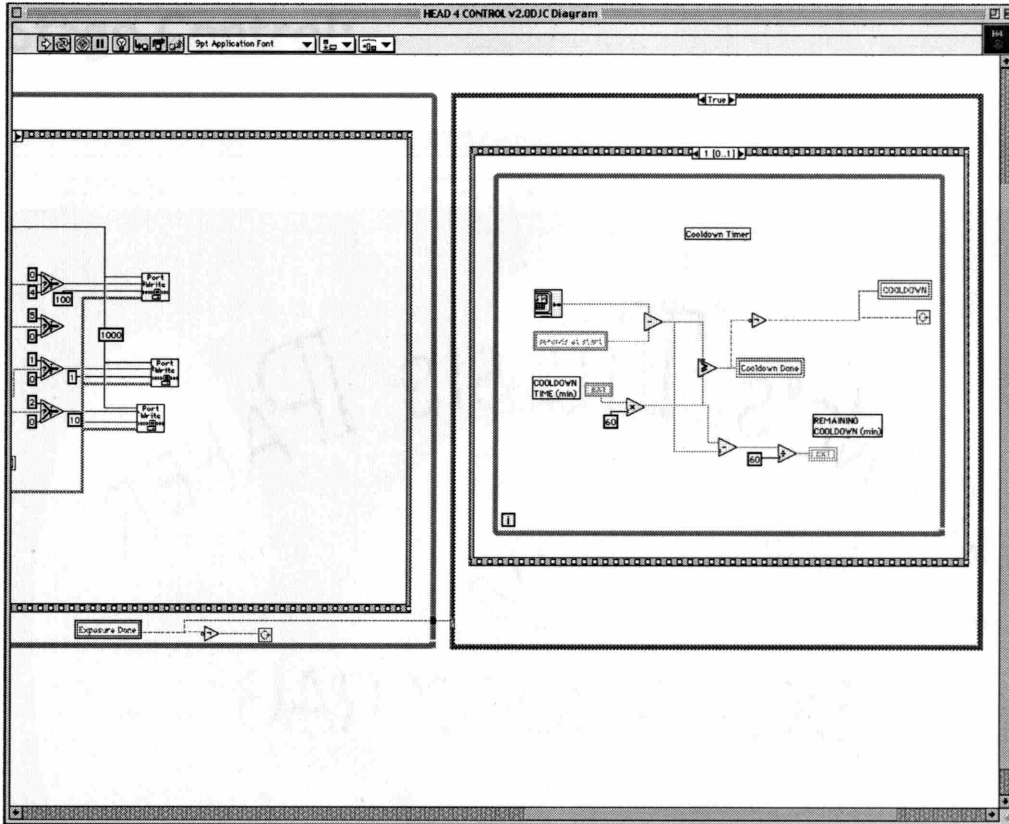
HEAD 4 CONTROL v2.0DJC Diagram
9pt Application Font
True
Cooldown Timer
COOLDOWN
Cooldown Done
COOLDOWN TIME (min)
REMAINING COOLDOWN (min)
Exposure Done
Port Write
100
1000
60

Stage Control:

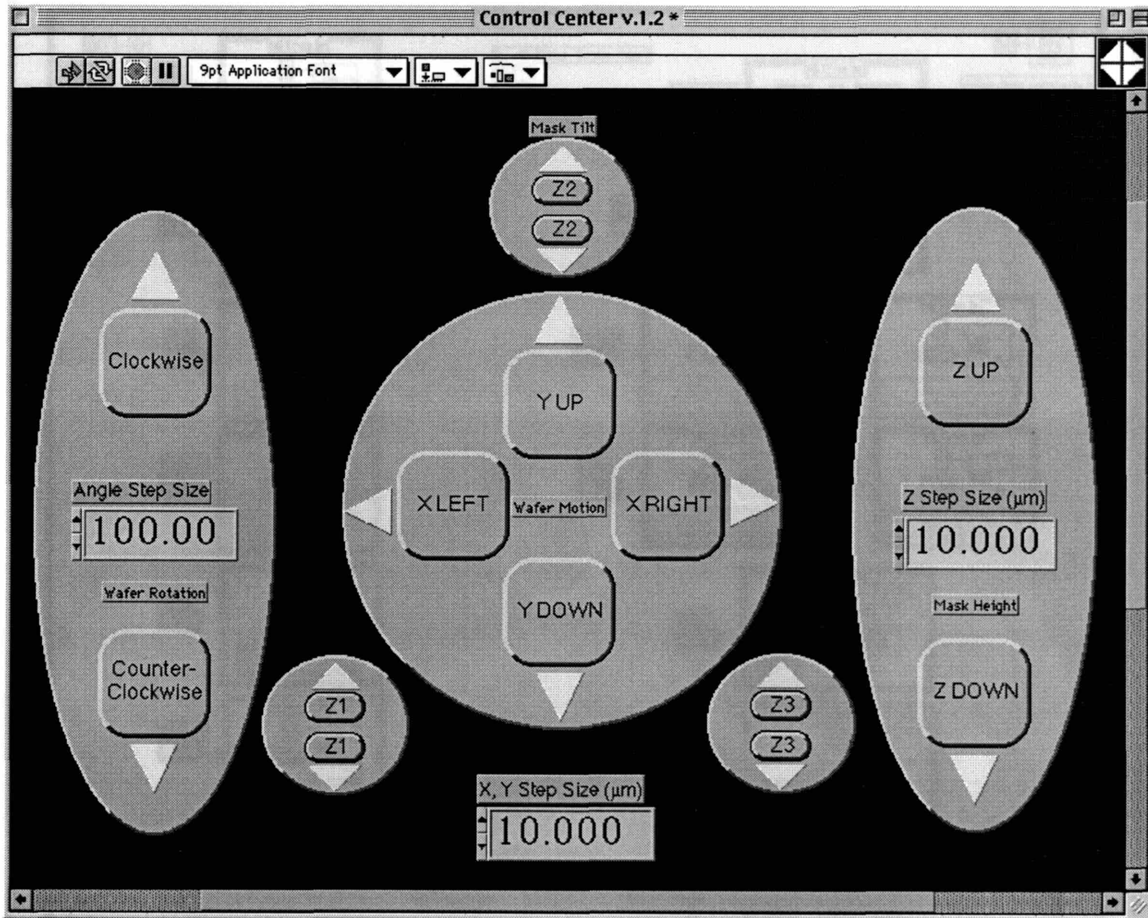

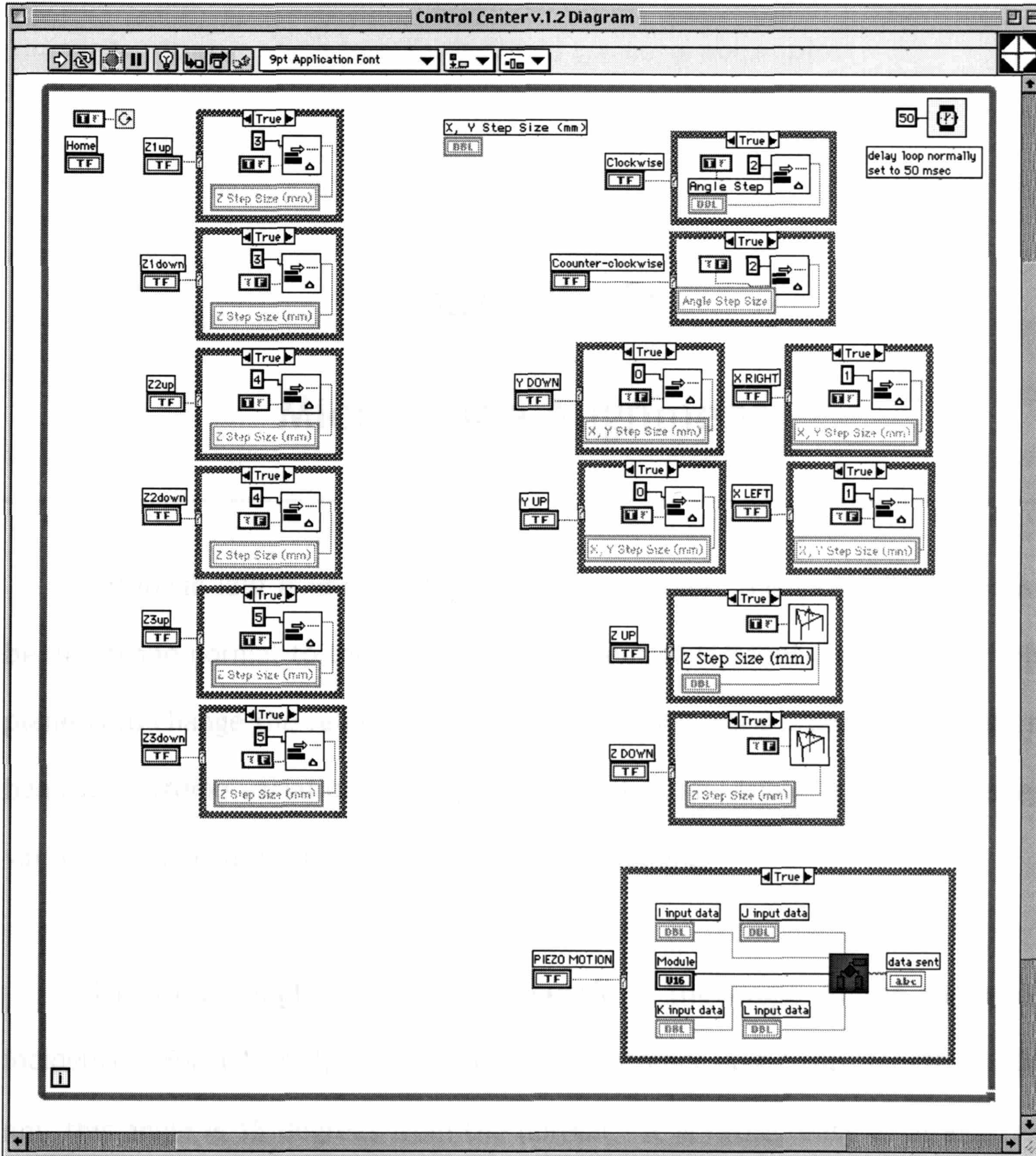

Control Center v.1.2 Diagram
9pt Application Font
Home
Z1up
Z1down
Z2up
Z2down
Z3up
Z3down
Z Step Size (mm)
X, Y Step Size (mm)
Clockwise
Counter-clockwise
Angle Step
Angle Step Size
Y DOWN
Y UP
X RIGHT
X LEFT
Z UP
Z DOWN
PIEZO MOTION
I input data
J input data
K input data
L input data
Module
data sent
True
50
delay loop normally set to 50 msec

Appendix C:
Microscope Alignment

Although IBBI is immune to many error sources, the incident light must be in a plane normal to the surface. The effect of incident angles out of this plane is to change the relative strengths of the diffracted orders in the return beams. Extreme variations in angle will result in no visible image and lesser variations will cause errors in the detected alignment.

The other angle we need to specify is the angle in the plane of incidence. For a 1 μm hatch period and the primary (avg.) wavelength at 506 nm, this angle is 15 degrees from the normal. It is rather easy to adjust the incident angle. With a test mark, one starts with the mirror adjusted for normal incidence to the wafer. The incident light reflects from the wafer and a bright spot is observed in the CCD image. This is a good time to adjust the transverse angle by sweeping through the reflected spot and centering it in the

image. Now that the transverse angle is set, the in-plane angle can be adjusted until the return from the hatched grating is maximized.

The above is a simple explanation of the final alignment, when the microscope is on Head 4. Prior to this we have to know that the fiber is sending the beam nearly on-axis inside the microscope. Due to a beamsplitter in the microscope, we cannot direct the input laser beam along the optical axis since the front faces of the beamsplitter will reflect a small fraction of light incident along the optical axis. The intensity of this reflection is far stronger than any alignment fringes. As a result, the incident beam must be offset in the plane of incidence such that the outgoing beam is (for instance) below the optical axis and the returning diffracted orders are slightly above the optical axis. This is done by adjusting the 5-axis fiber positioner on a separate test stand. Using a mirror placed in front of the objective lens the input beam is oriented along the optical axis. The position of the reflected beam is gauged by observing the spot on the CCD. The mirror is removed and a narrow slit is placed in front of the objective lens. The position of the fiber is adjusted along the axis of the slit until the internal reflections from the beamsplitter inside the microscope are essentially eliminated. At this point a test wafer is used to check proper imaging of light diffracted at the Littrow angle. After passing these tests, the microscope is placed in the alignment system.

Appendix D:

Head 4 Mechanical Drawings

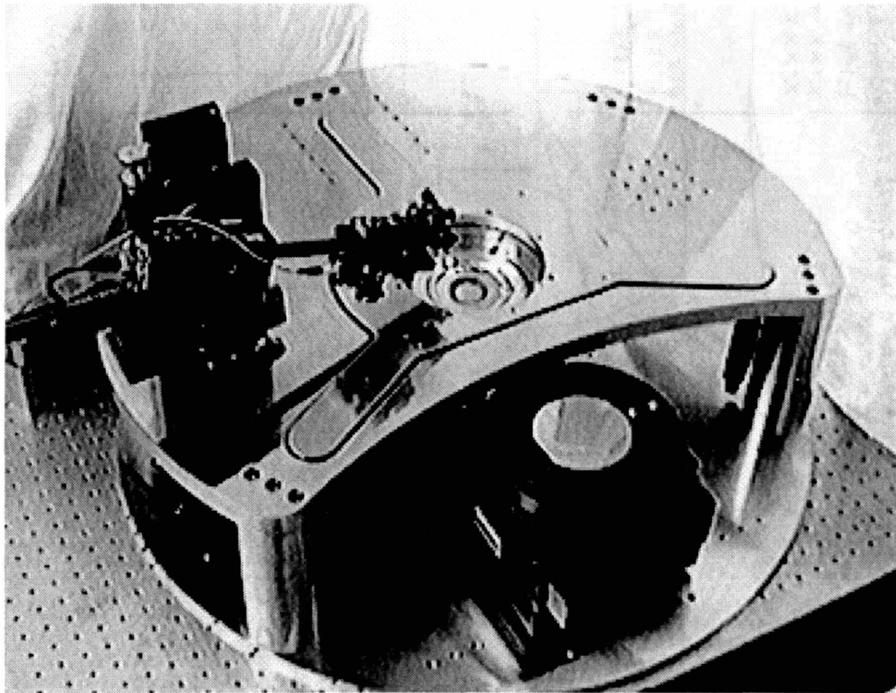

Figure E-1: Photograph of Head 4 alignment stages during construction.

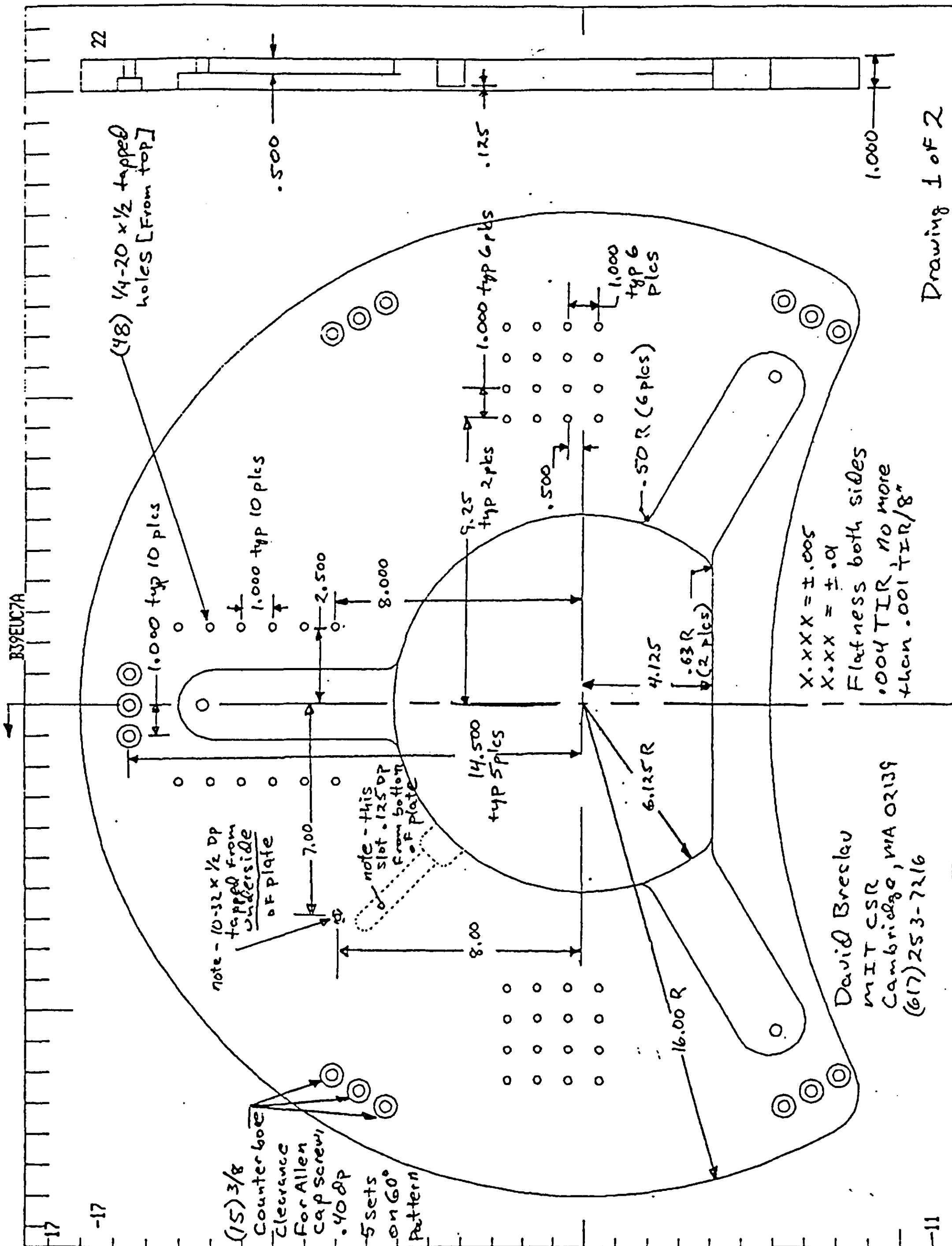
(48) 1/4-20 x 1/2 tapped holes [From top]
.500
.125
1.000
Drawing 1 of 2
1.000 typ 10 plcs
1.000 typ 10 plcs
2.500
8.000
9.25 typ 2 plcs
1.000 typ 6 plcs
.500
.50 R (6 plcs)
14.500 typ 5 plcs
4.125
.63 R (2 plcs)
6.125 R
16.00 R
7.00
8.00
X.XXX = ±.005
X.XX = ±.01
Flatness both sides
.004 TIR, no more than .001 TIR/8"
David Breslau
MIT CSR
Cambridge, MA 02139
(617)253-7216
(15) 3/8 Counterbore Clearance For Allen cap screw, .40 dp
5 sets on 60° Pattern
B39EUC7A

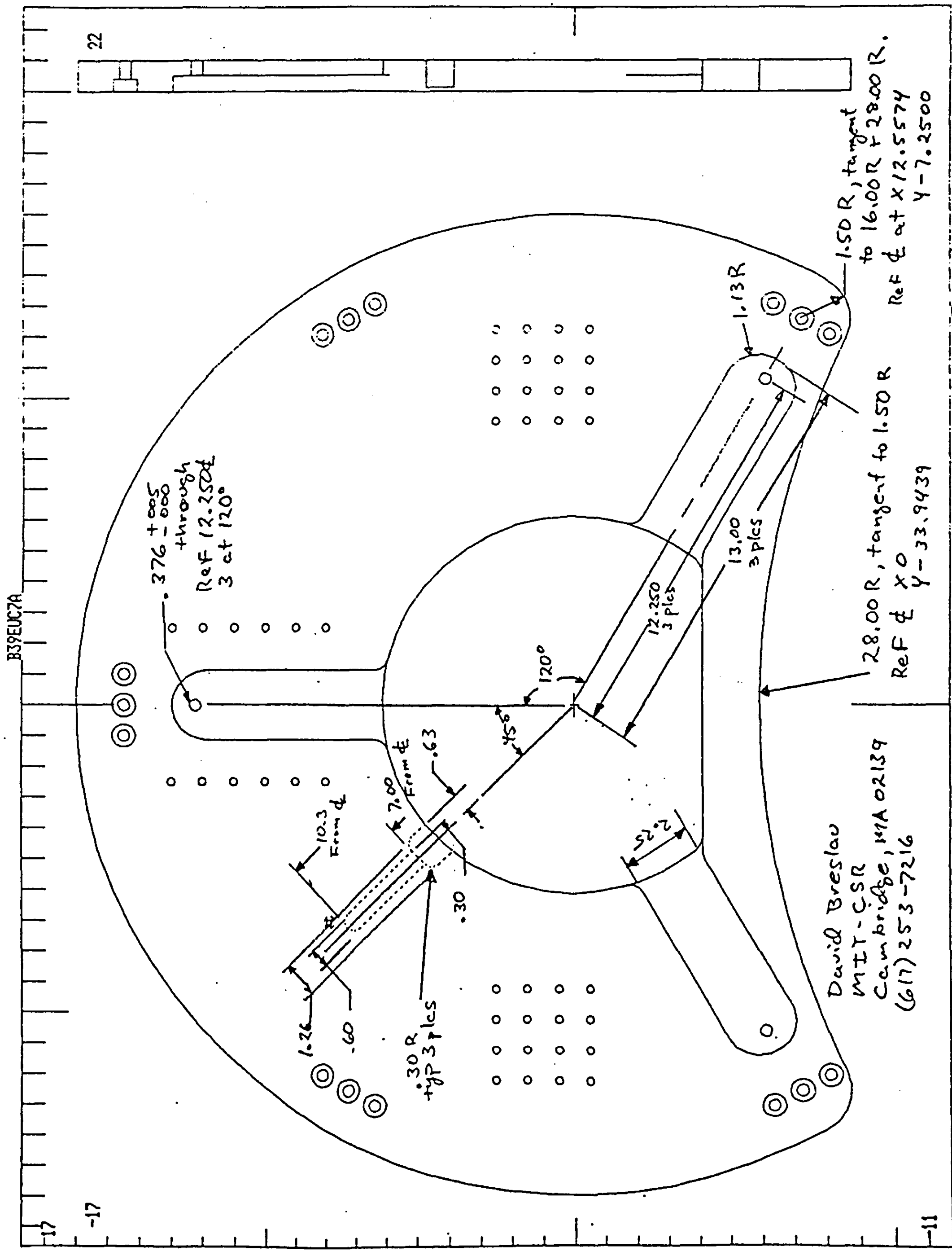

B39EUC7A
.376 +.005 -.000 through
Ref 12.250 ℄
3 at 120°
120°
45°
7.00 From ℄
.63
10.3 From ℄
.30
.30 R typ 3 plcs
1.26
.60
2.25
12.250 3 plcs
13.00 3 plcs
1.13R
1.50 R, tangent to 16.00 R + 28.00 R.
Ref ℄ at X 12.5574 Y -7.2500
28.00 R, tangent to 1.50 R
Ref ℄ X 0 Y -33.9439
David Breslau
MIT-CSR
Cambridge, MA 02139
(617) 253-7216
Drawing 2 of 2

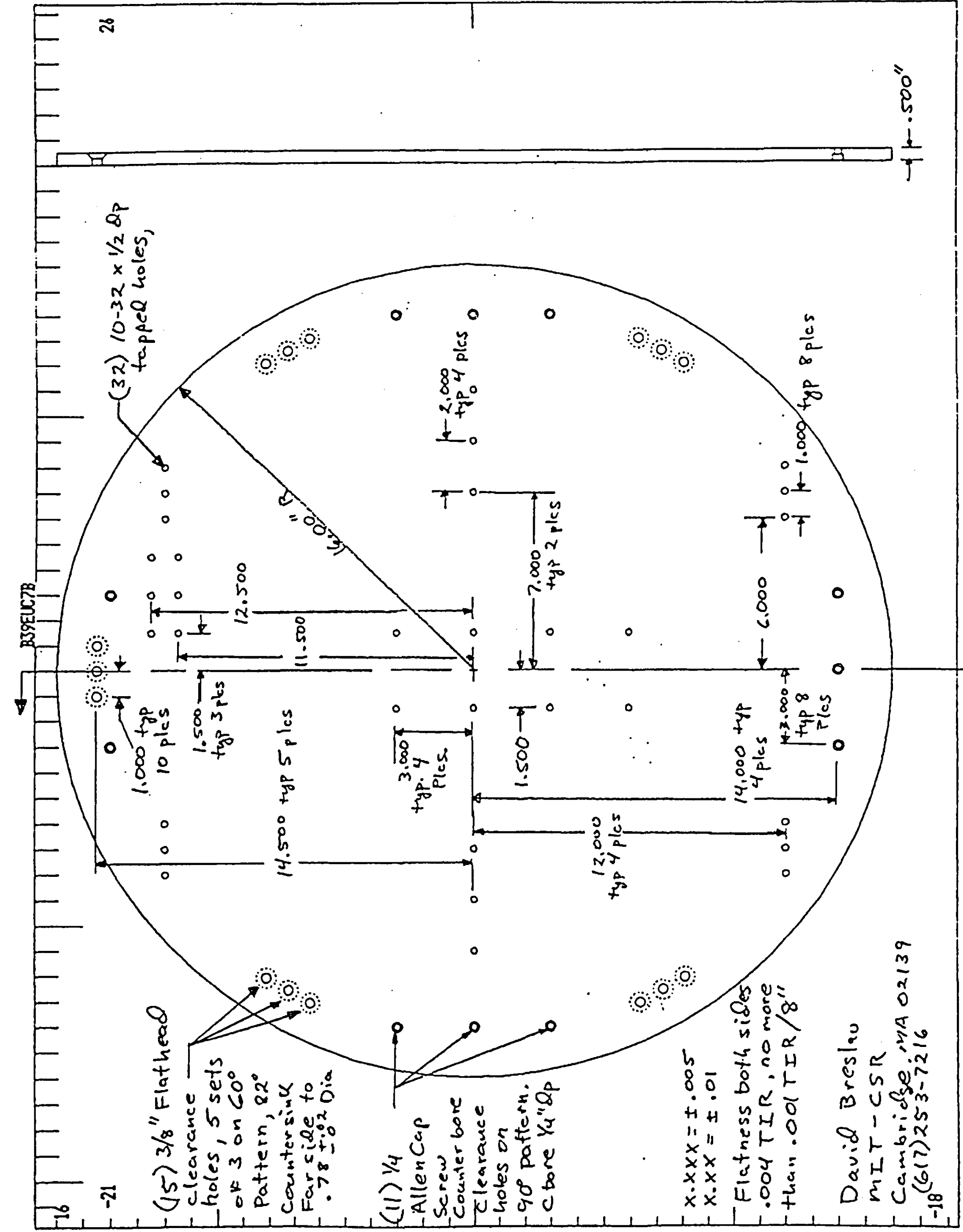
(32) 10-32 x 1/2 Dp
tapped holes,
(15) 3/8" Flathead clearance holes, 5 sets of 3 on 60° Pattern, 82° Countersink Far side to .78 +.02 -0 Dia
(11) 1/4 Allen Cap Screw Counter bore Clearance holes on 90° pattern. c bore 1/4" Dp
x.xxx = ±.005
x.xx = ±.01
Flatness both sides .004 TIR, no more than .001 TIR/8"
David Breslau
MIT - CSR
Cambridge, MA 02139
(617)253-7216
B39EUC7B

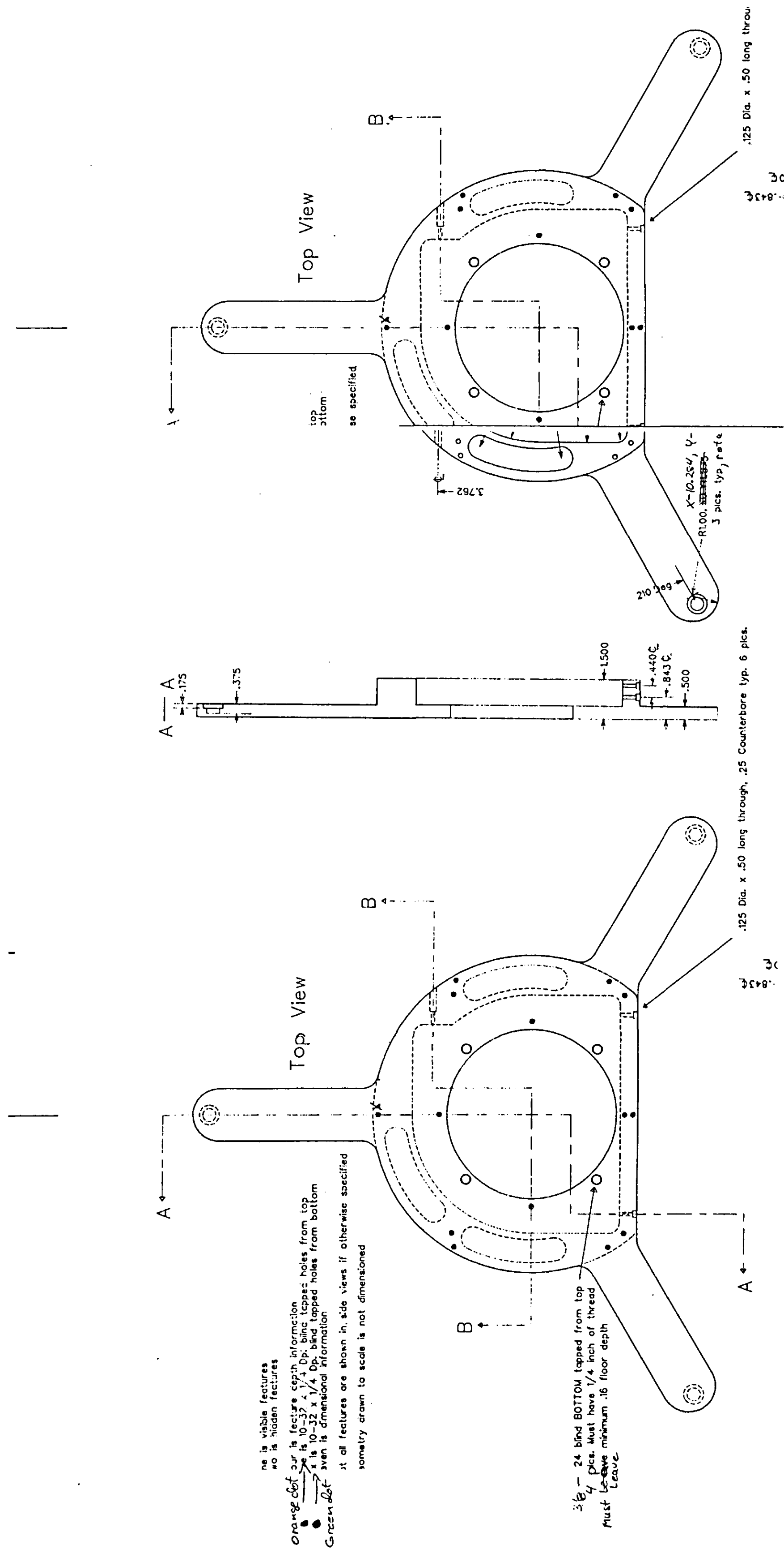

Top View
Top View
.125 Dia. x .50 long through, .25 Counterbore typ. 6 plcs.
1.500
.375
.175
.500
3.762

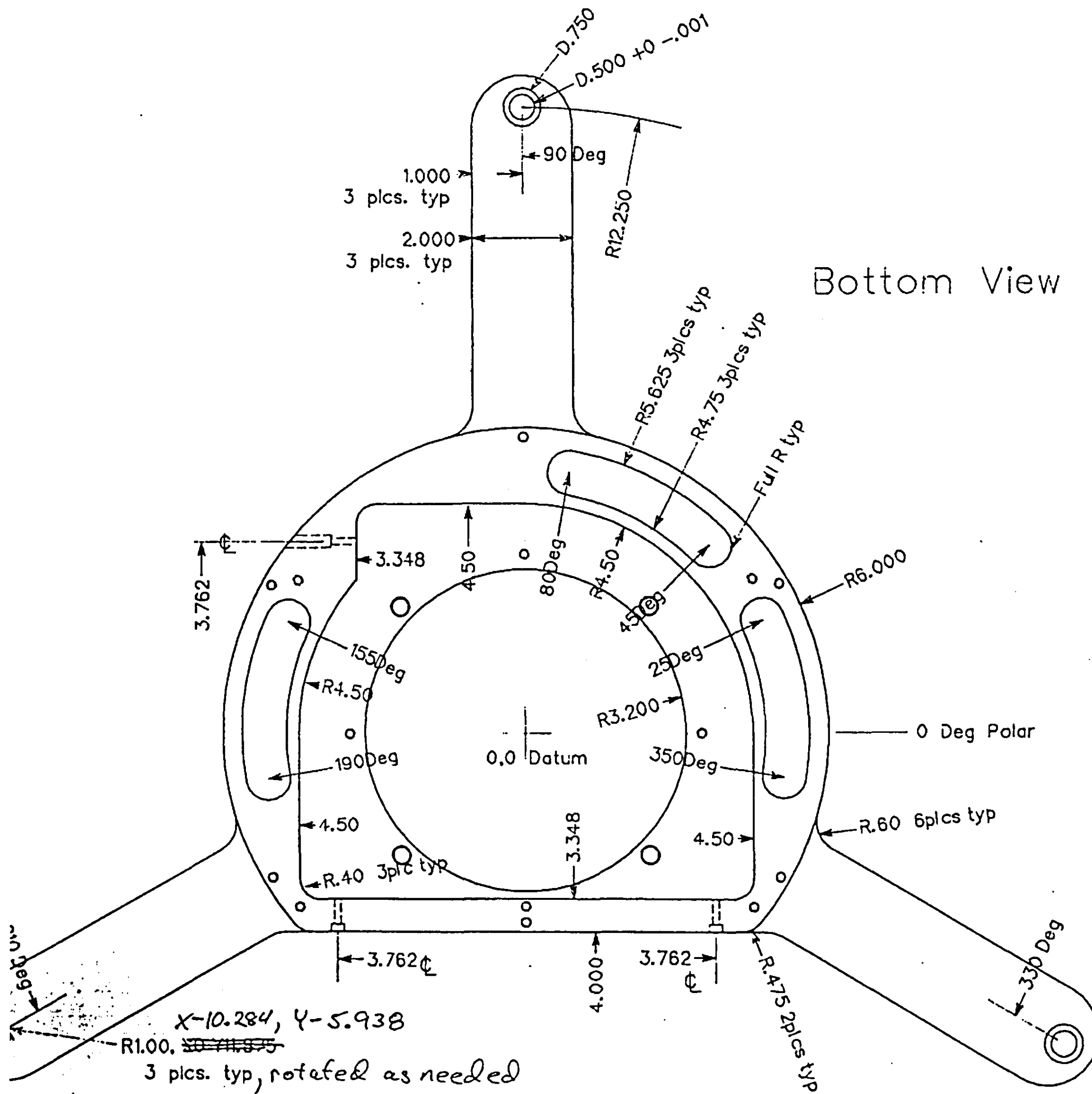
D.750
D.500 +0 -.001
90 Deg
1.000
3 plcs. typ
2.000
3 plcs. typ
R12.250
Bottom View
R5.625 3plcs typ
R4.75 3plcs typ
Full R typ
3.348
4.50
80Deg
R4.50
45Deg
R6.000
3.762
155Deg
25Deg
R4.50
R3.200
0 Deg Polar
190Deg
0.0 Datum
350Deg
4.50
3.348
4.50
R.60 6plcs typ
R.40 3plc typ
3.762
3.762
4.000
R.475 2plcs typ
330 Deg
X-10.284, Y-5.938
R1.00,
3 plcs. typ, rotated as needed

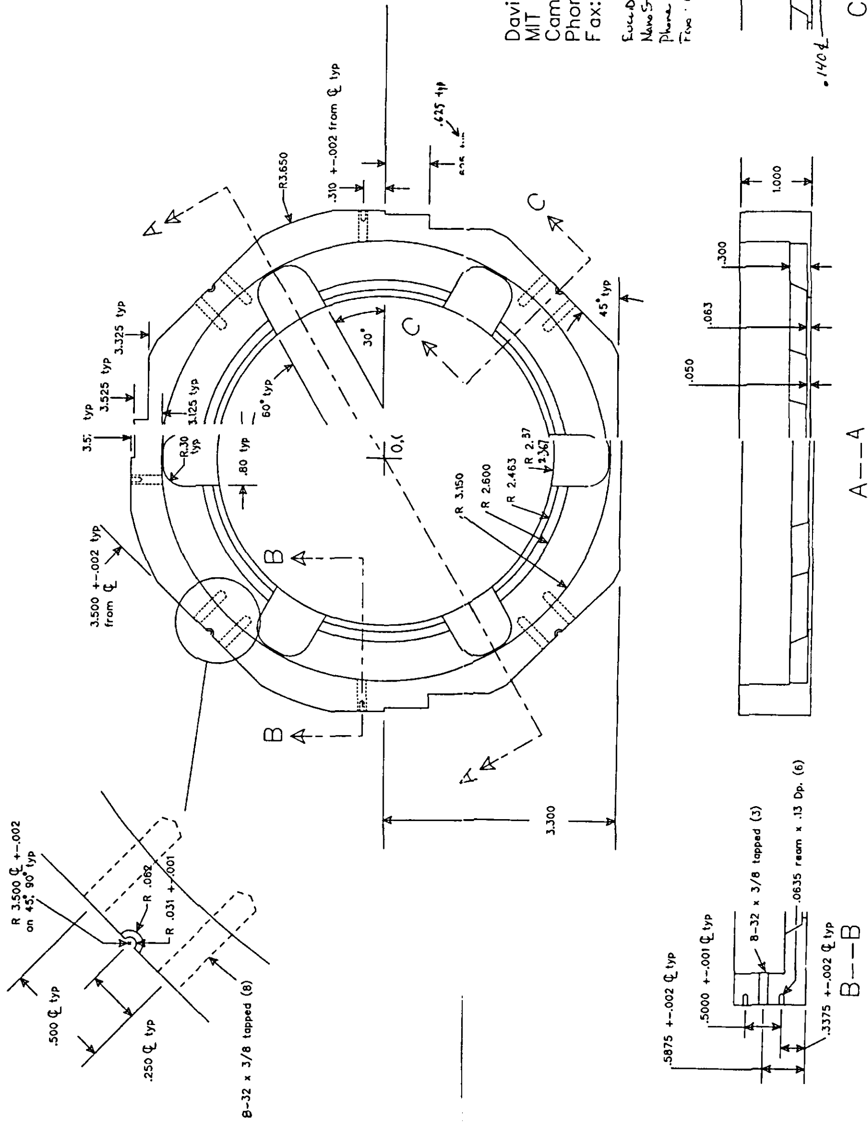
David Breslau
MIT Center for Space Research
Cambridge MA 02139
Phone: (617) 253-7216
Fax: (617) 253-0861
A--A
B--B
C--C
R3.650
R 3.150
R 2.600
R 2.463
3.300
1.000
.300
.063
.050
3.325 typ
3.525 typ
3.125 typ
.80 typ
60° typ
30°
45° typ
.310 +-.002 from ℄ typ
3.500 +-.002 typ from ℄
R 3.500 ℄ +-.002 on 45°, 90° typ
R .062
R .031 +-.001
.500 ℄ typ
.250 ℄ typ
8-32 x 3/8 tapped (8)
8-32 x 3/8 tapped (3)
.0635 ream x .13 Dp. (6)
.5875 +-.002 ℄ typ
.5000 +-.001 ℄ typ
.3375 +-.002 ℄ typ
.281 typ

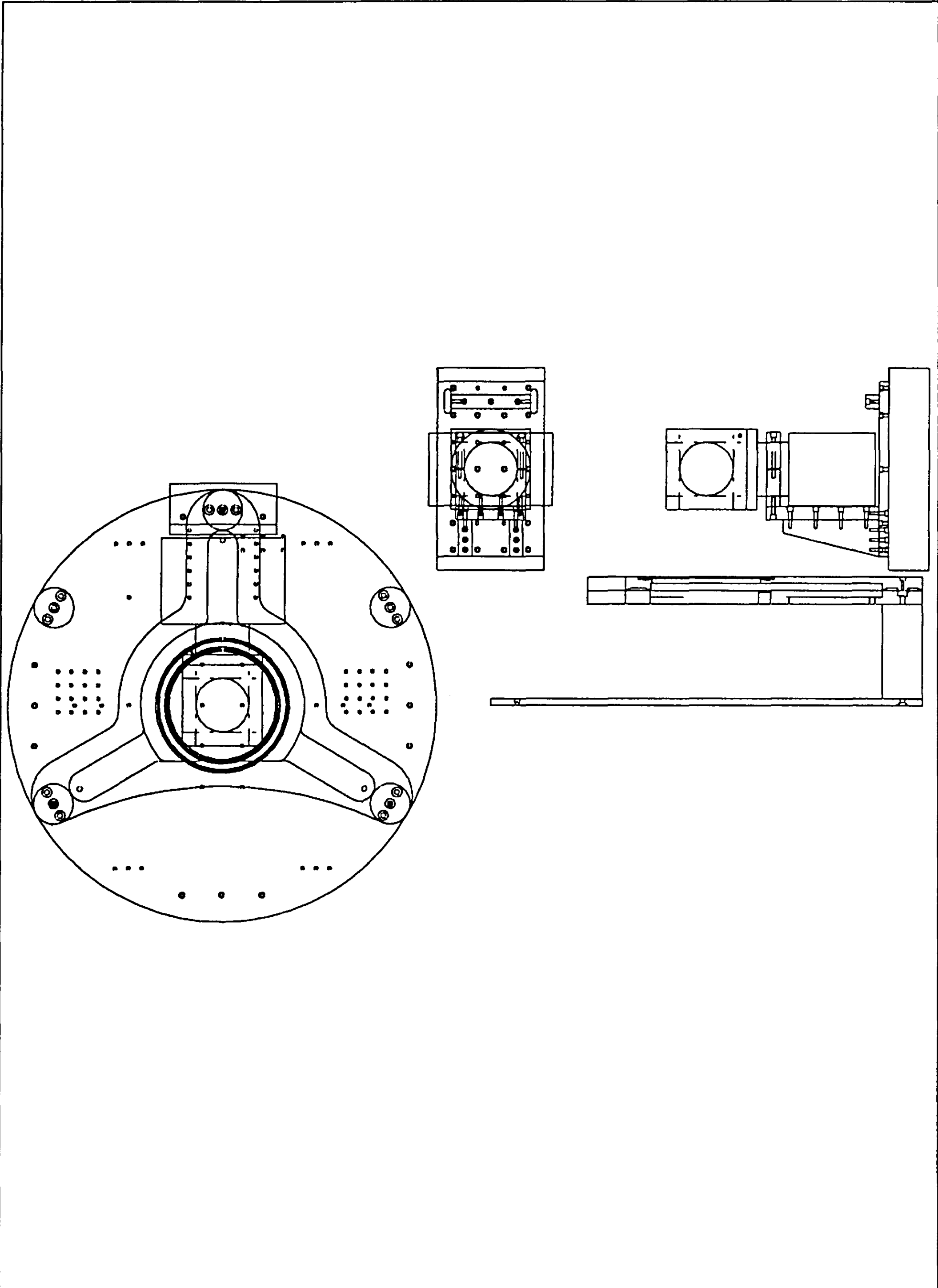

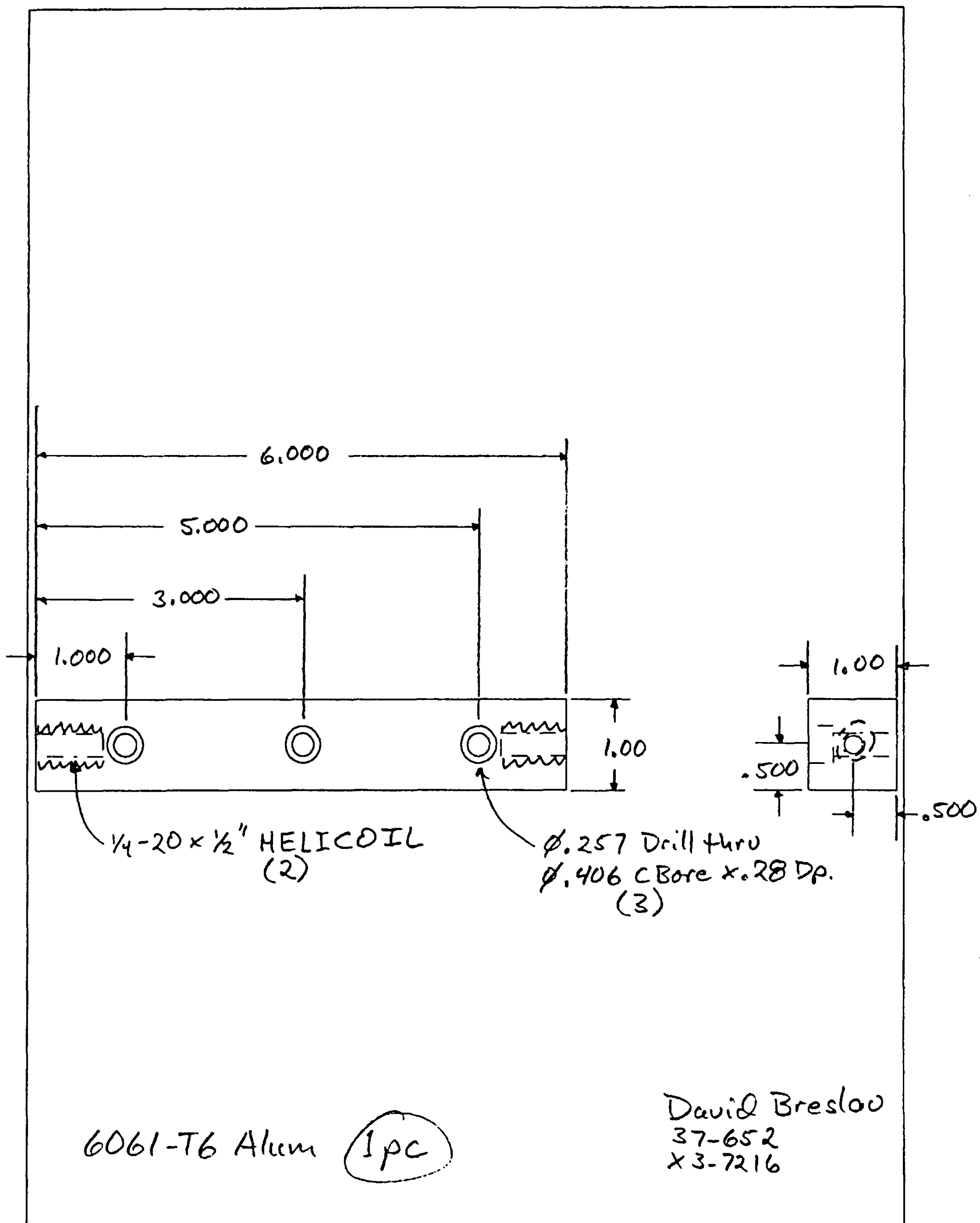
6.000
5.000
3.000
1.000
1.00
1.00
.500
.500
1/4-20 x 1/2" HELICOIL
(2)
⌀.257 Drill thru
⌀.406 CBore x.28 Dp.
(3)
6061-T6 Alum
1pc
David Breslau
37-652
X3-7216

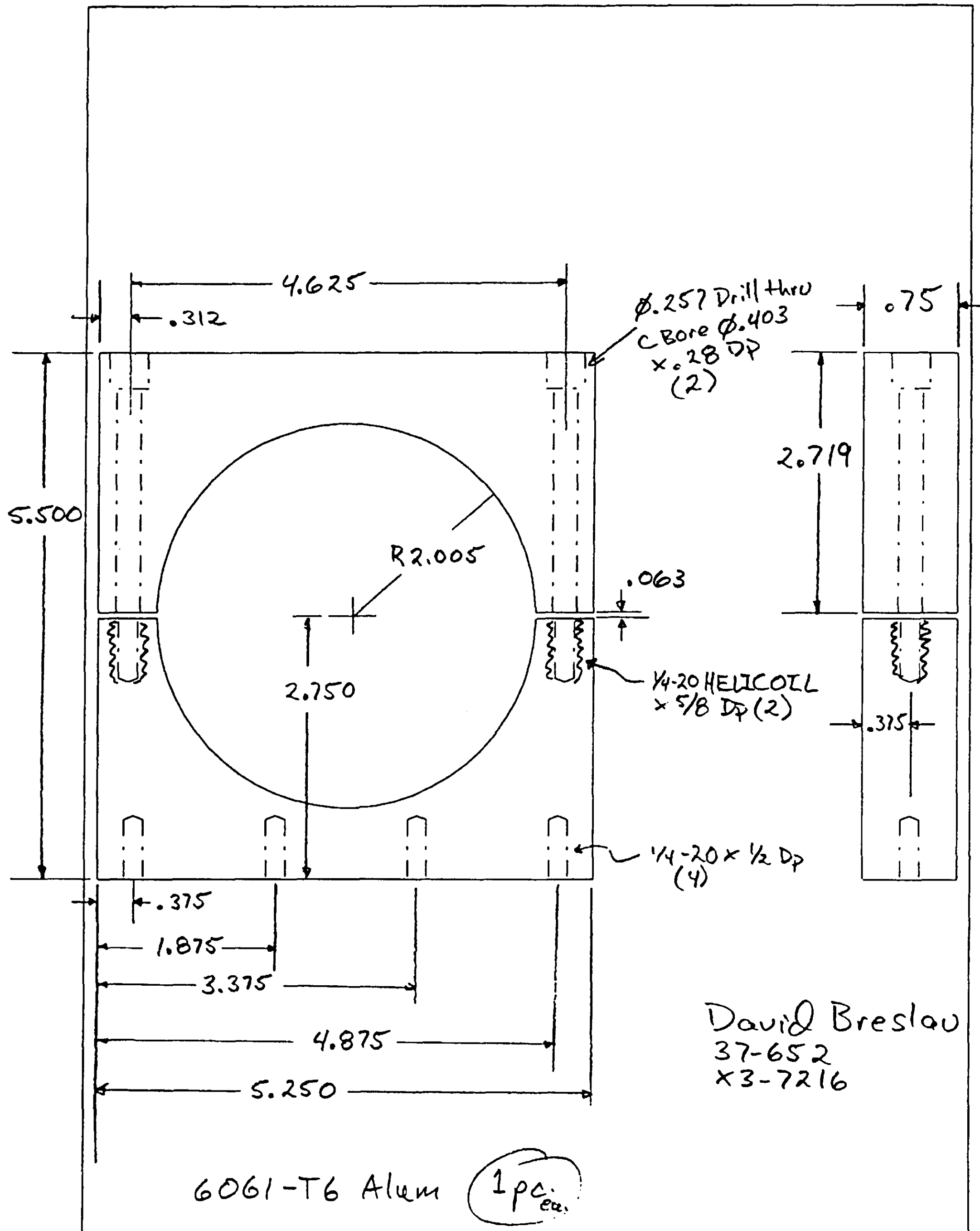
4.625
.312
Ø.257 Drill thru
C Bore Ø.403
x.28 DP
(2)
.75
5.500
2.719
R2.005
.063
2.750
1/4-20 HELICOIL
x 5/8 DP (2)
.375
1/4-20 x 1/2 DP
(4)
.375
1.875
3.375
4.875
5.250
David Breslau
37-652
x3-7216
6061-T6 Alum
1pc. ea.

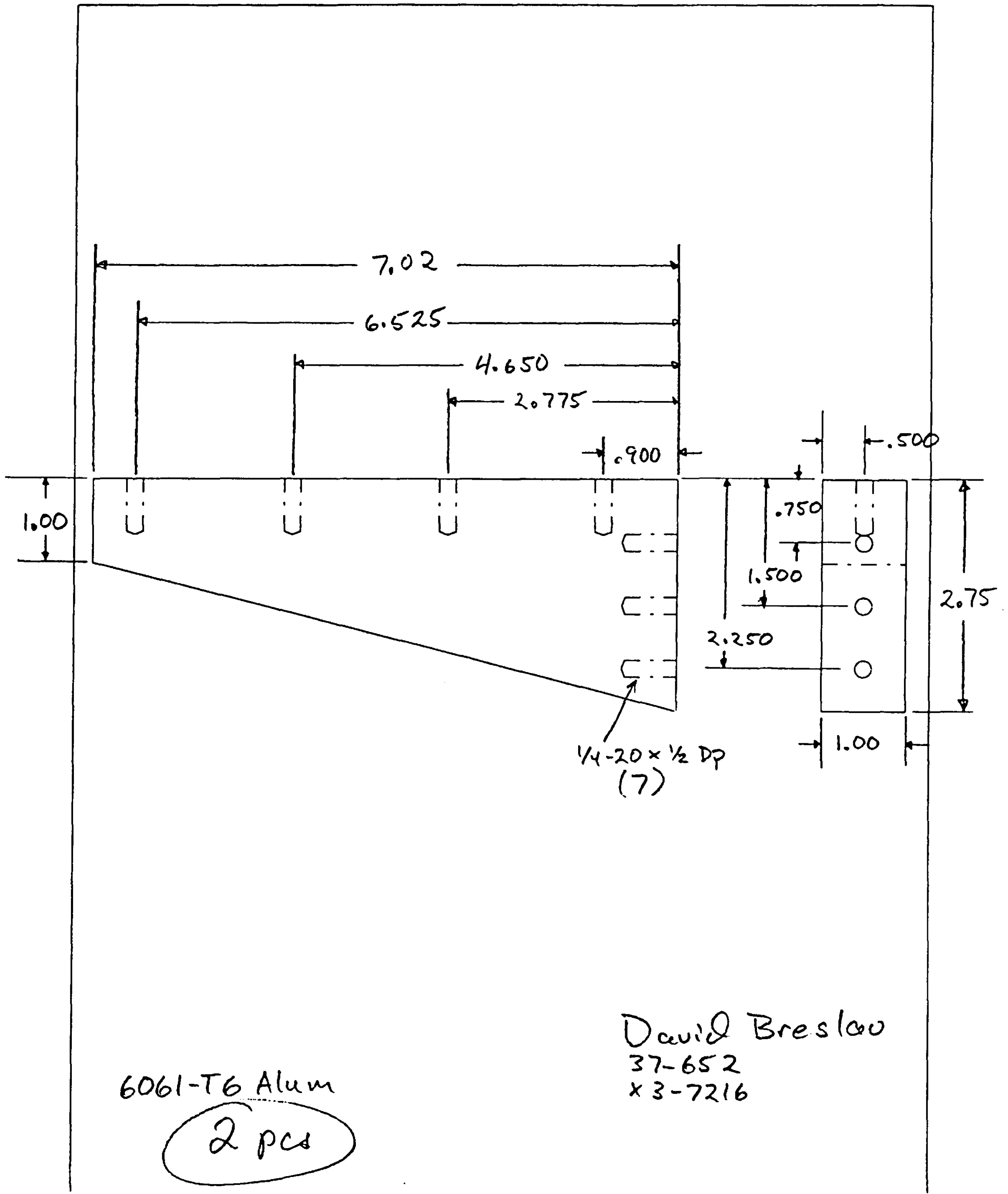

7.02
6.525
4.650
2.775
.900
.500
1.00
.750
1.500
2.250
2.75
1.00
1/4-20 x 1/2 Dp
(7)
David Breslau
37-652
x 3-7216
6061-T6 Alum
2 pcs

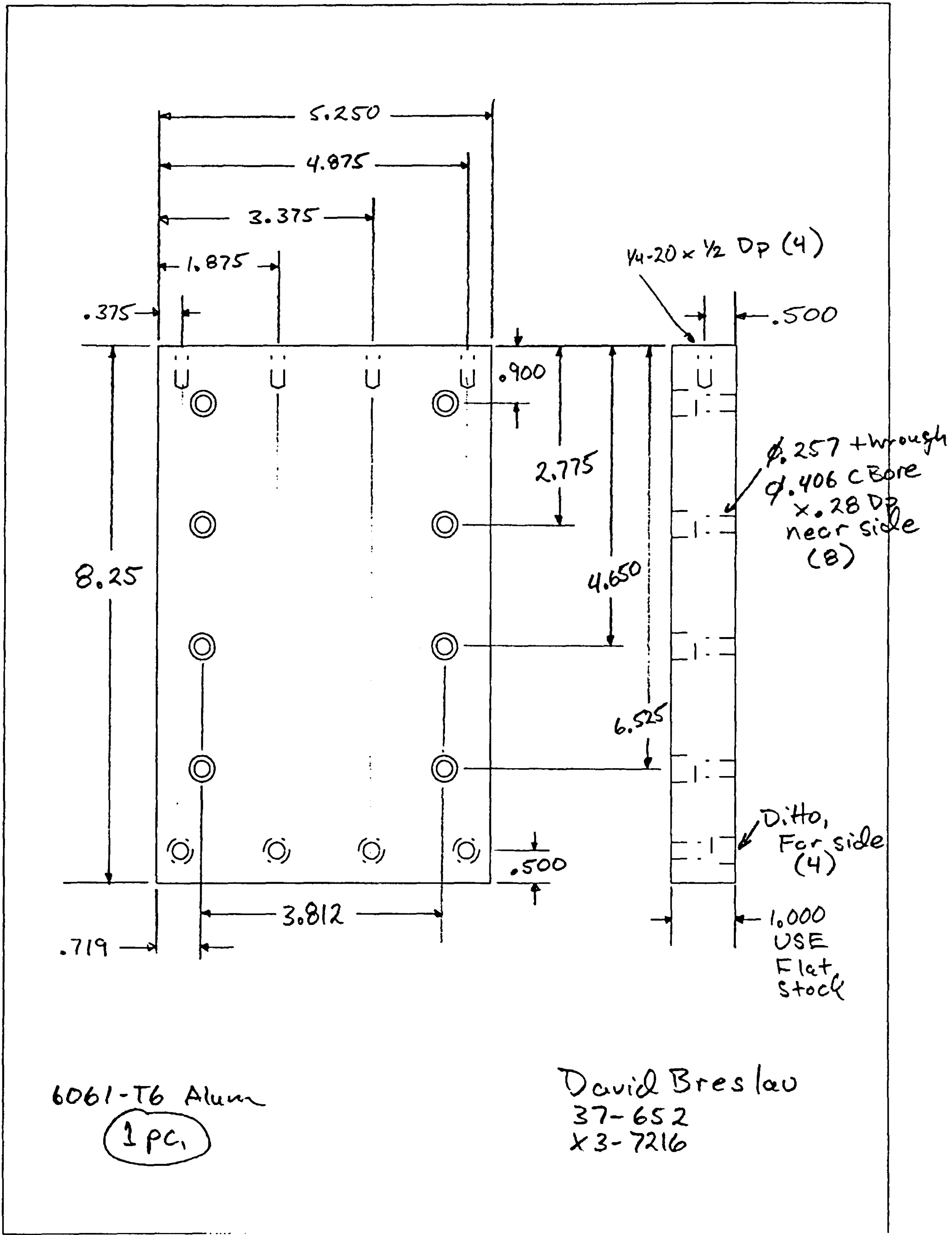
5.250
4.875
3.375
1.875
.375
1/4-20 x 1/2 Dp (4)
.500
.900
2.775
4.650
6.525
8.25
Ø.257 through
Ø.406 C Bore
x.28 Dp
near side
(8)
Ditto,
Far side
(4)
.500
3.812
.719
1.000
USE
Flat
Stock
6061-T6 Alum
1 pc.
David Breslau
37-652
x3-7216

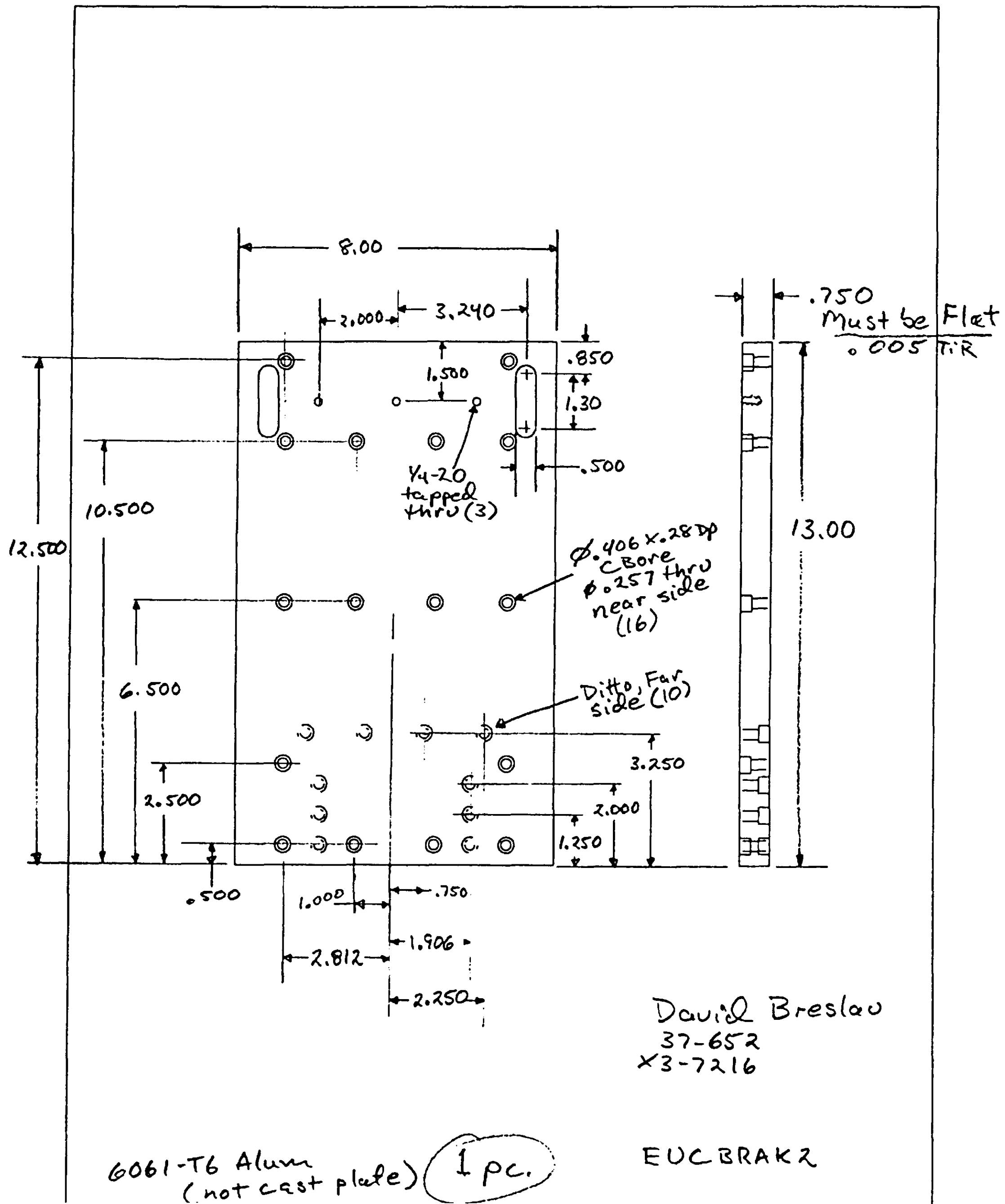
8.00
2.000
3.240
.750
Must be Flat
.005 TIR
.850
1.500
1.30
.500
1/4-20
tapped
thru (3)
10.500
12.500
13.00
⌀.406 x .28 Dp
C Bore
⌀.257 thru
near side
(16)
6.500
Ditto, Far
side (10)
3.250
2.500
2.000
1.250
.500
1.000
.750
1.906
2.812
2.250
David Breslau
37-652
x3-7216
6061-T6 Alum
(not cast plate)
1 pc.
EUCBRAK2

Mirror Mount

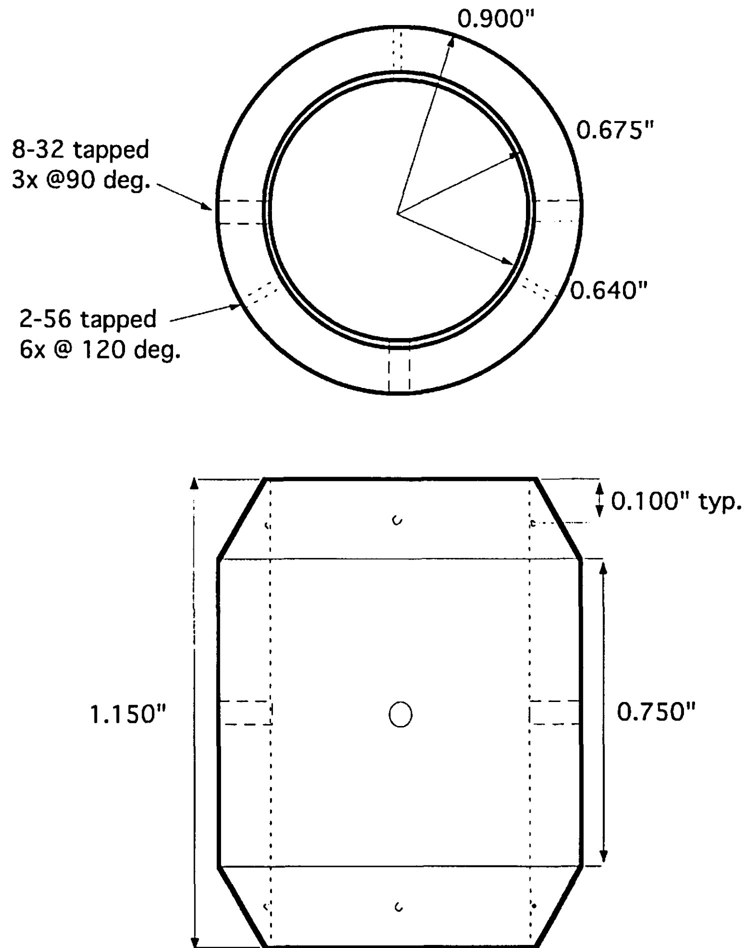

Euclid Moon

QUANTITY = 4

1:3 scale
304 Stainless Steel
x3-0979

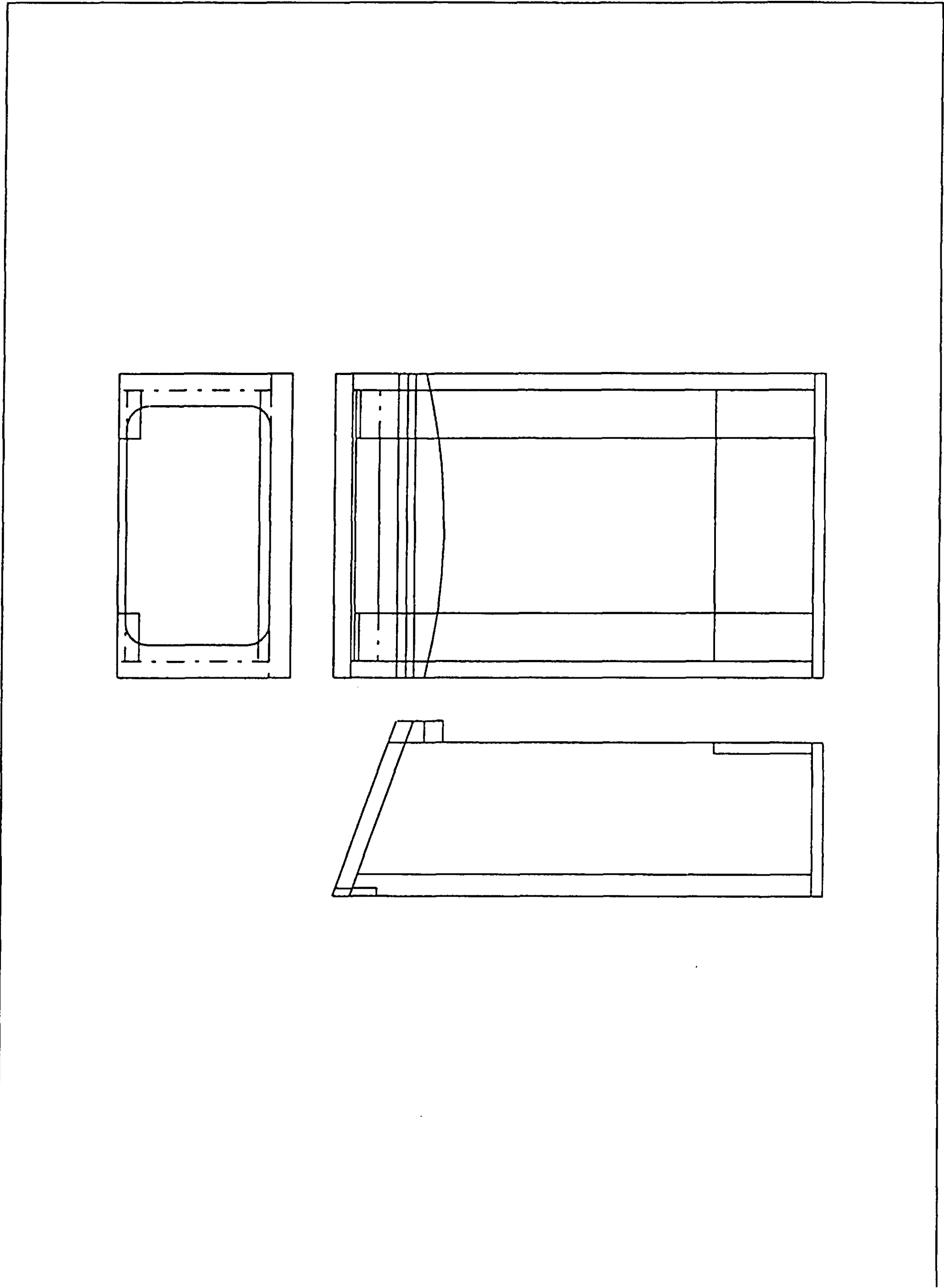

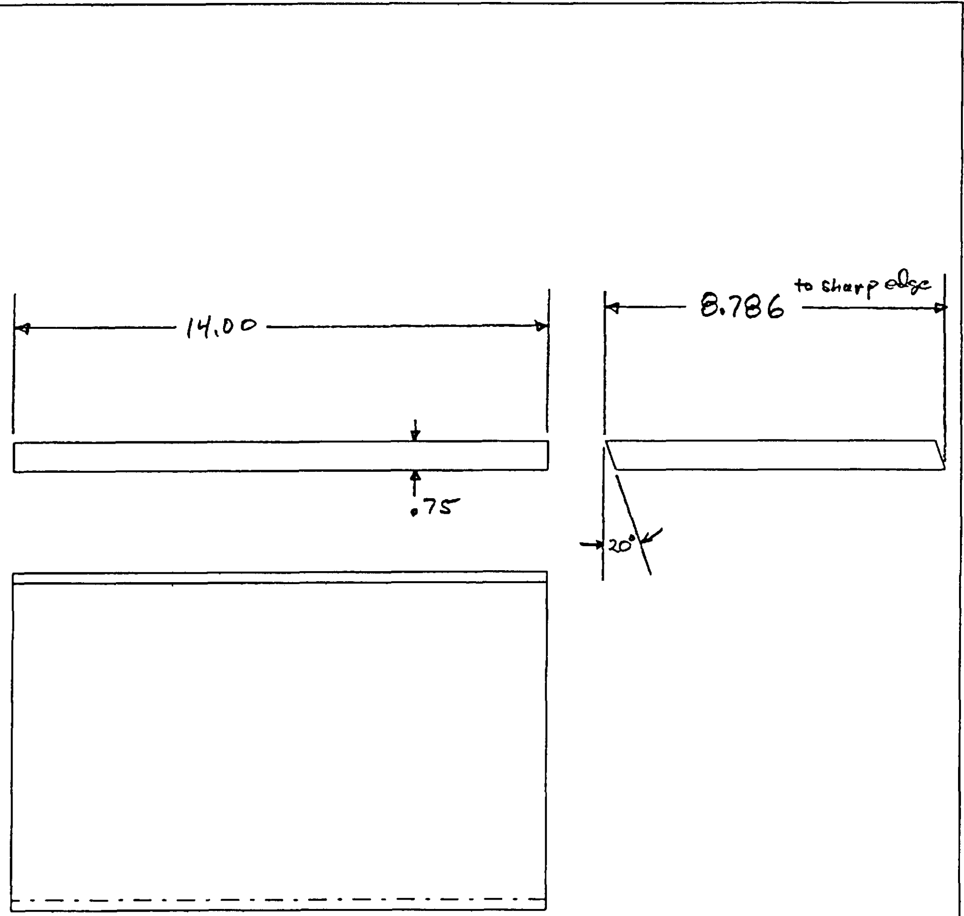
14.00
8.786 to sharp edge
.75
20°
1 pc. Clear Acrylic
David Breslau
MIT CSR
(617)253-7216(W)
(617)253-0861 (Fax)

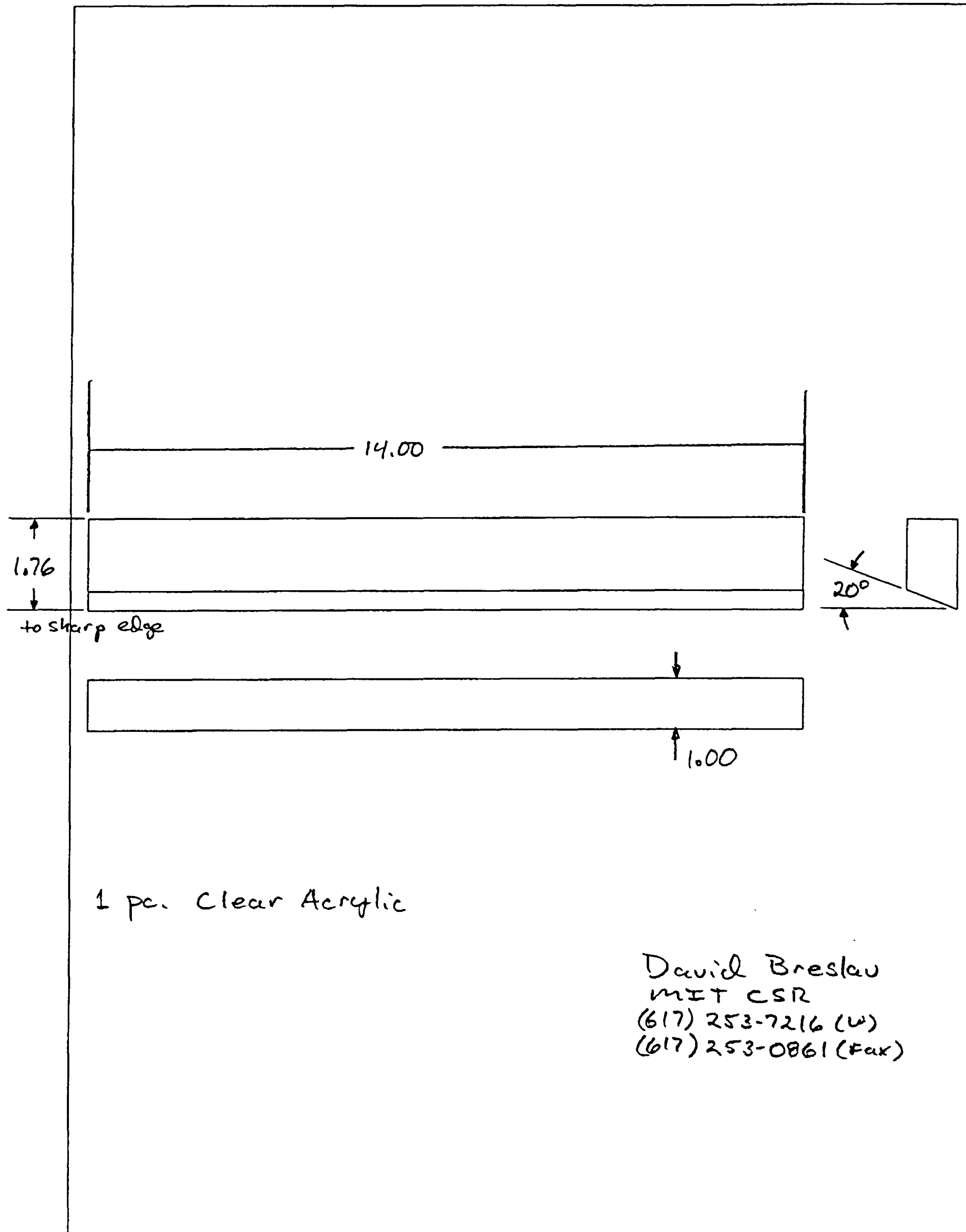
14.00
1.76
to sharp edge
20°
1.00
1 pc. Clear Acrylic
David Breslau
MIT CSR
(617) 253-7216 (W)
(617) 253-0861 (Fax)

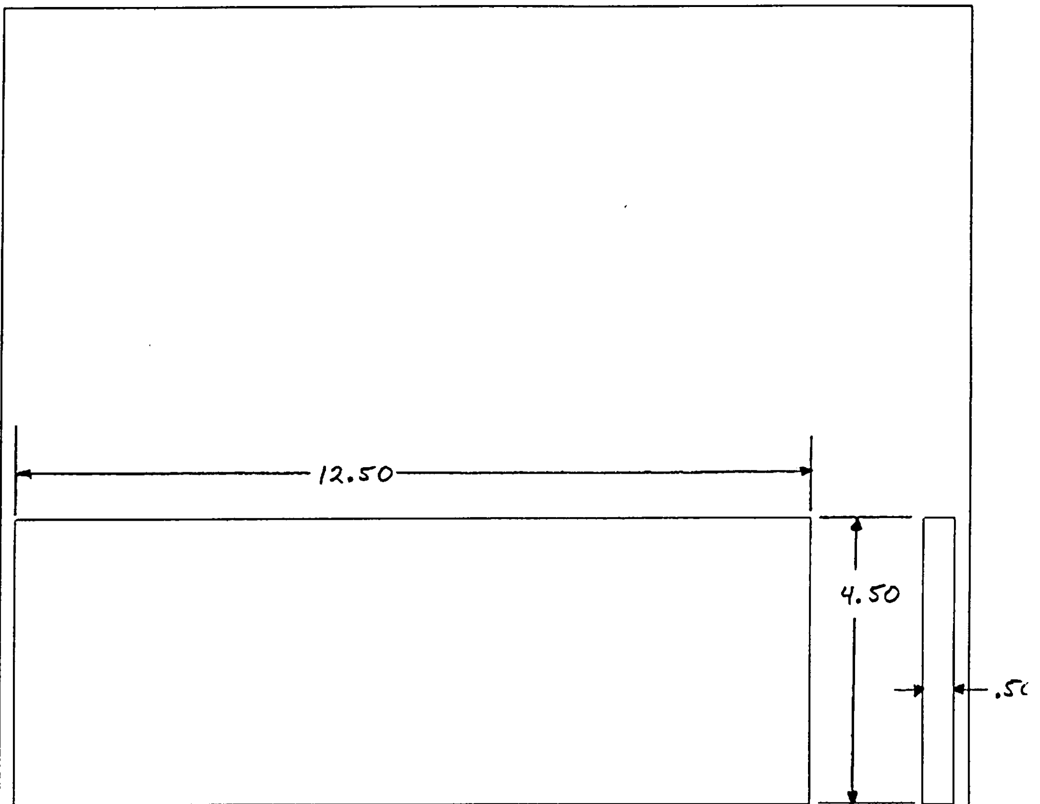

1 pc. Clear Acrylic

David Breslau
MIT CSR
(617) 253-7216 (w)
(617) 253-0861 (Fax)

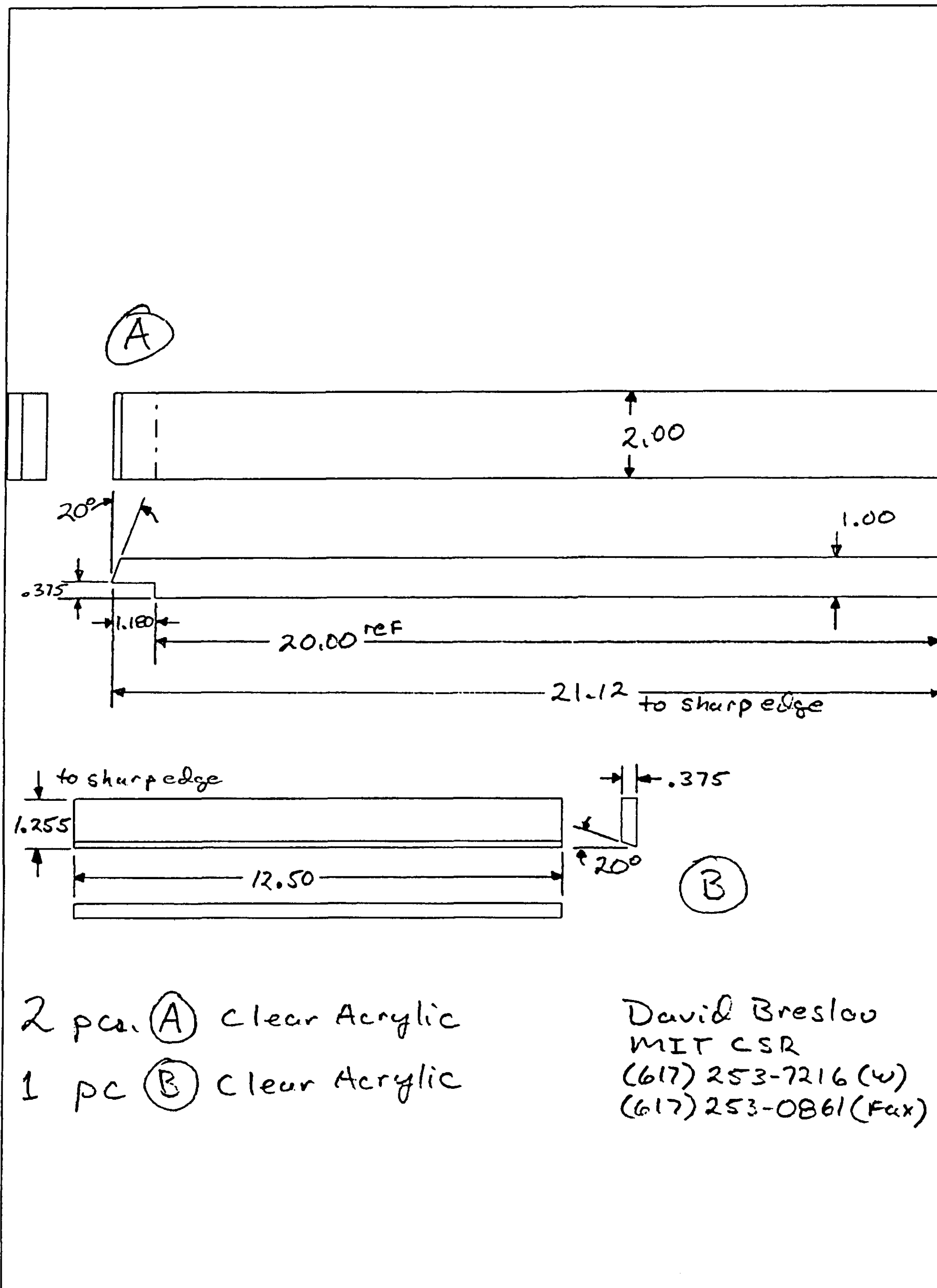
A
2.00
20°
1.00
.375
1.180
20.00 ref
21.12 to sharp edge
to sharp edge
.375
1.255
12.50
20°
B
2 pcs. A Clear Acrylic
1 pc B Clear Acrylic
David Breslau
MIT CSR
(617) 253-7216 (w)
(617) 253-0861 (Fax)

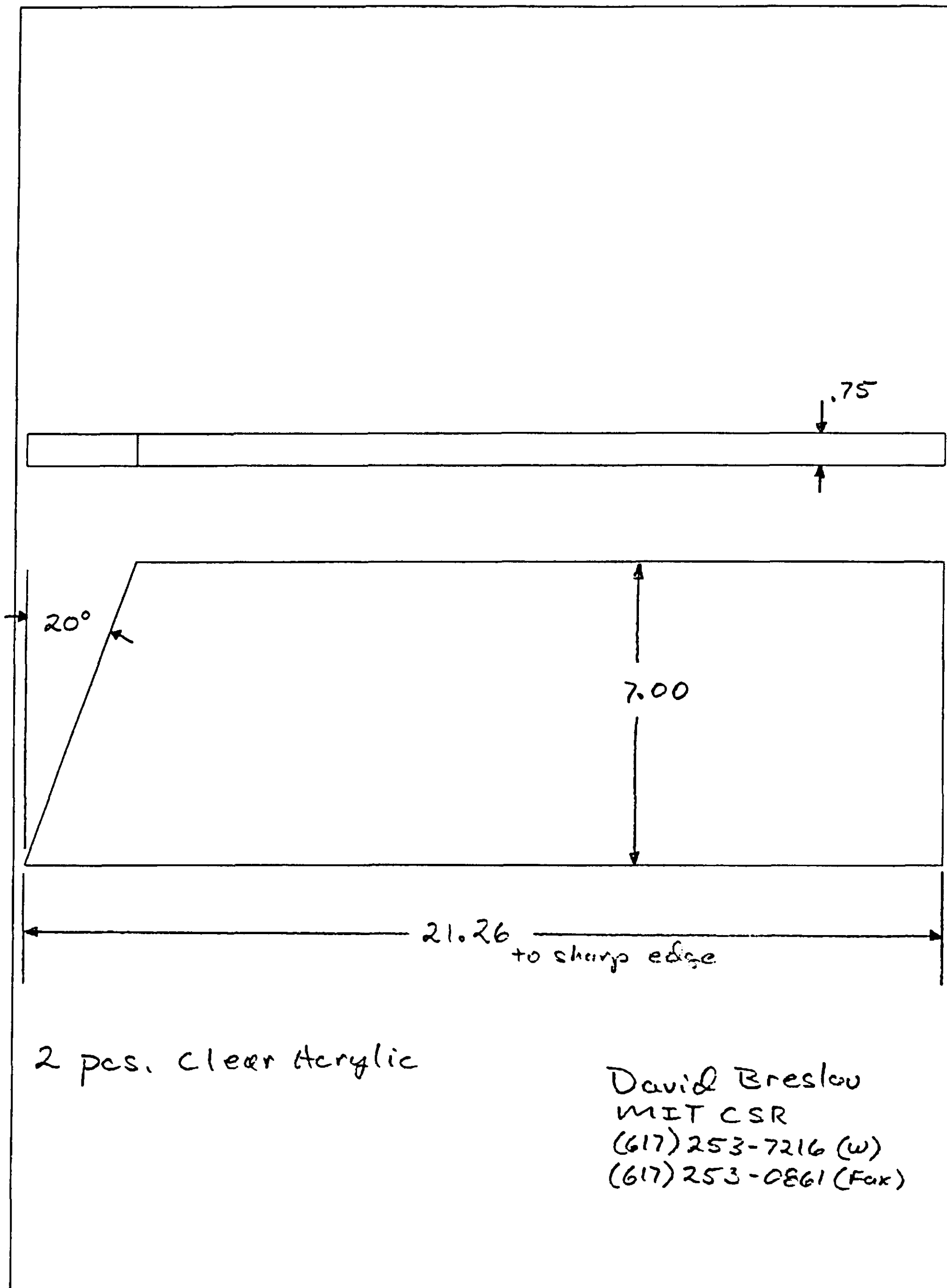
.75
20°
7.00
21.26 to sharp edge
2 pcs. Clear Acrylic
David Breslau
MIT CSR
(617) 253-7216 (W)
(617) 253-0861 (Fax)

Helium Enclosure
Top plate

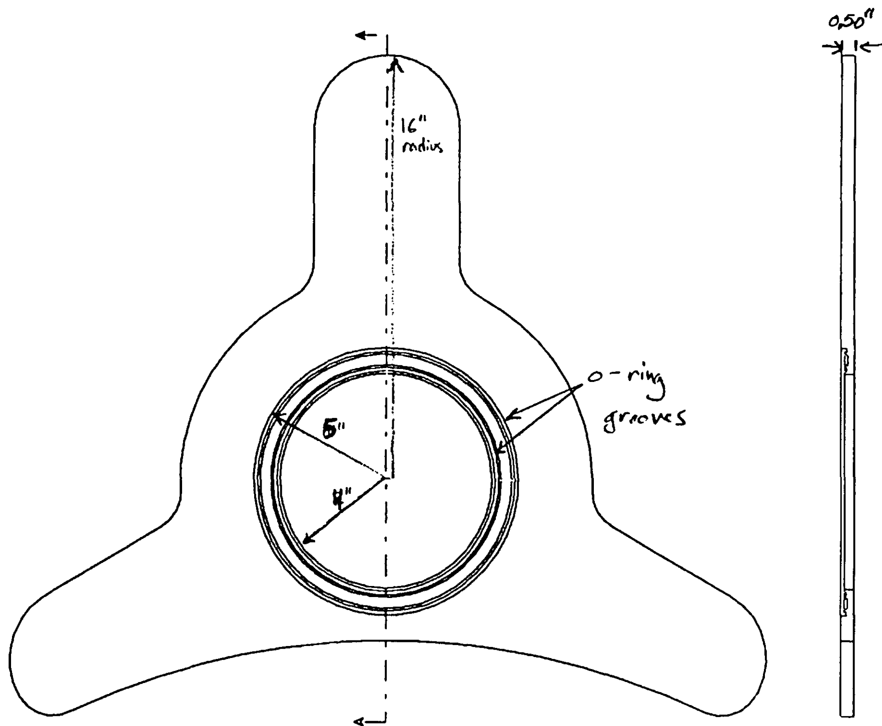

Euclid Moon
David Breslau
(617) 253-[illegible]979
(617) 253-8509 fax
Plexiglas

Page 1

Helium Enclosure
Bottom plate

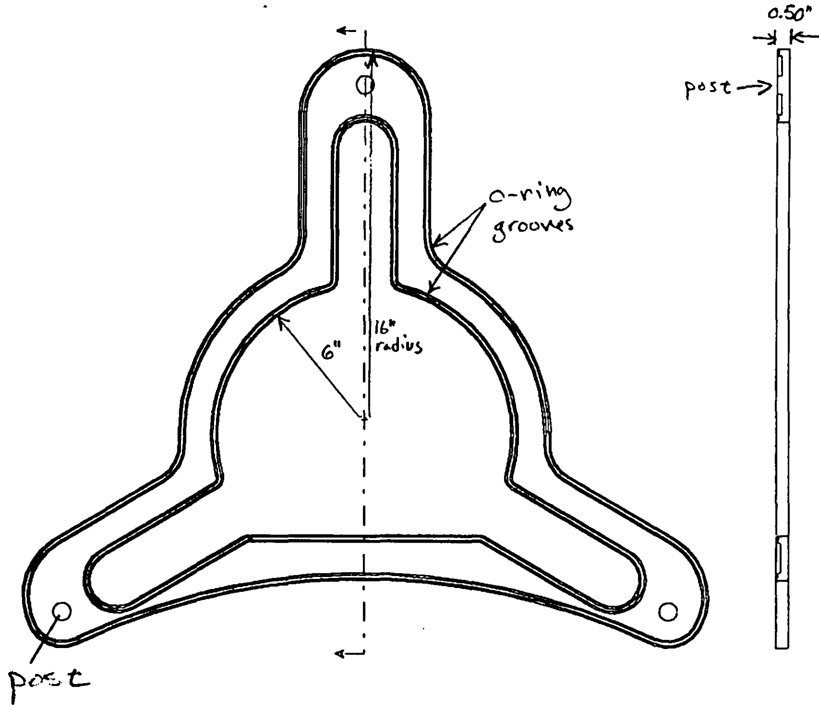

Bond upper & lower plates,
o-ring grooves facing out

Euclid [illegible]
David Breslau
(617) 253-0979
(617) 253-8503 fax
Plexiglas

page 2

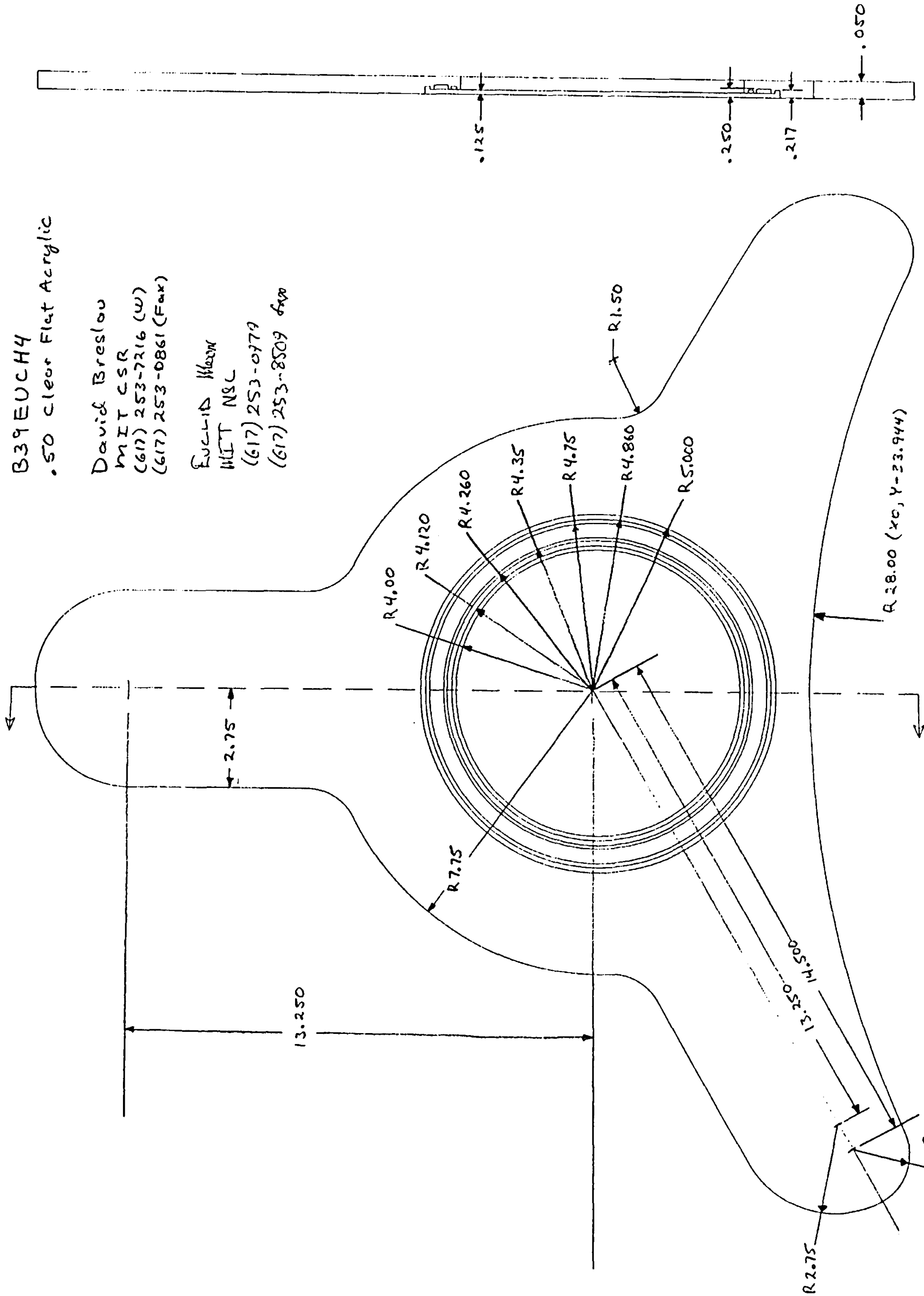
B39EUCH4
.50 clear Flat Acrylic
MIT CSR
(617) 253-7216 (W)
(617) 253-0861 (Fax)
MIT NSL
(617) 253-0779
(617) 253-8509 fax
R4.00
R4.120
R4.260
R4.35
R4.75
R4.860
R5.000
R1.50
R28.00 (XC, Y-23.944)
R7.75
2.75
13.250
13.250
14.500
R2.75
R1.50
.125
.250
.217
.050

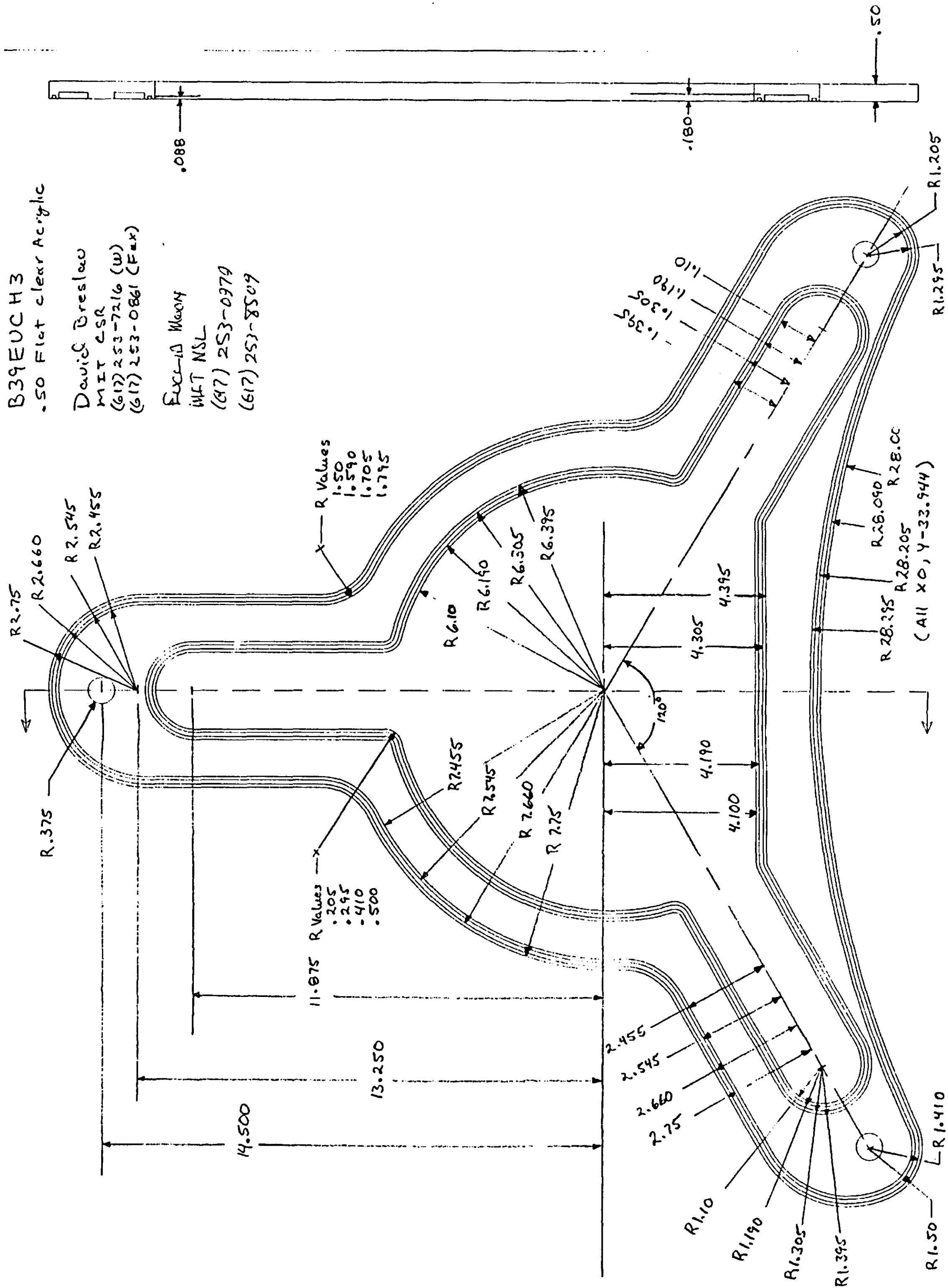

B39EUCH3
.50 Flat clear Acrylic
David Breslau
MIT CSR
(617) 253-7216 (W)
(617) 253-0861 (Fax)
MIT NSL
(617) 253-0379
(617) 253-8509
.088
.180
.50
R Values
1.50
1.590
1.705
1.795
R Values
.205
.295
.410
.500
R2.75
R2.660
R2.545
R2.455
R.375
R6.10
R6.190
R6.305
R6.395
R2.455
R2.545
R 2.660
R 2.75
4.395
4.305
4.190
4.100
120°
11.875
13.250
14.500
2.455
2.545
2.660
2.75
R1.10
R1.190
R1.305
R1.395
R1.50
R1.410
R1.205
R1.295
R28.090
R28.205
R28.295
(All X0, Y-33.944)

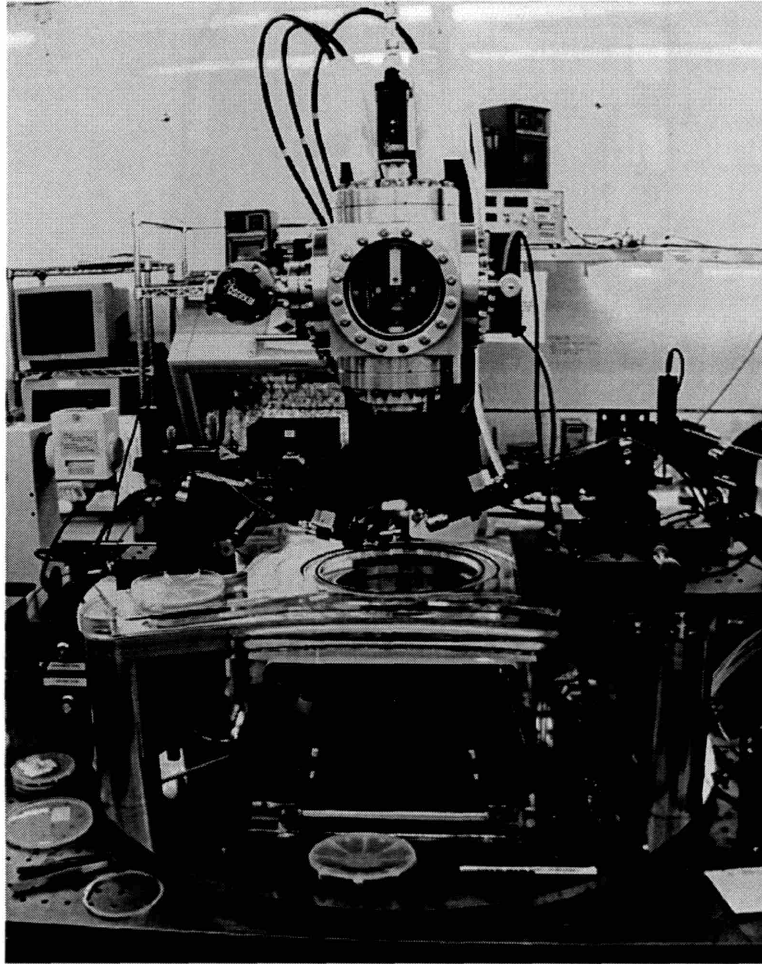

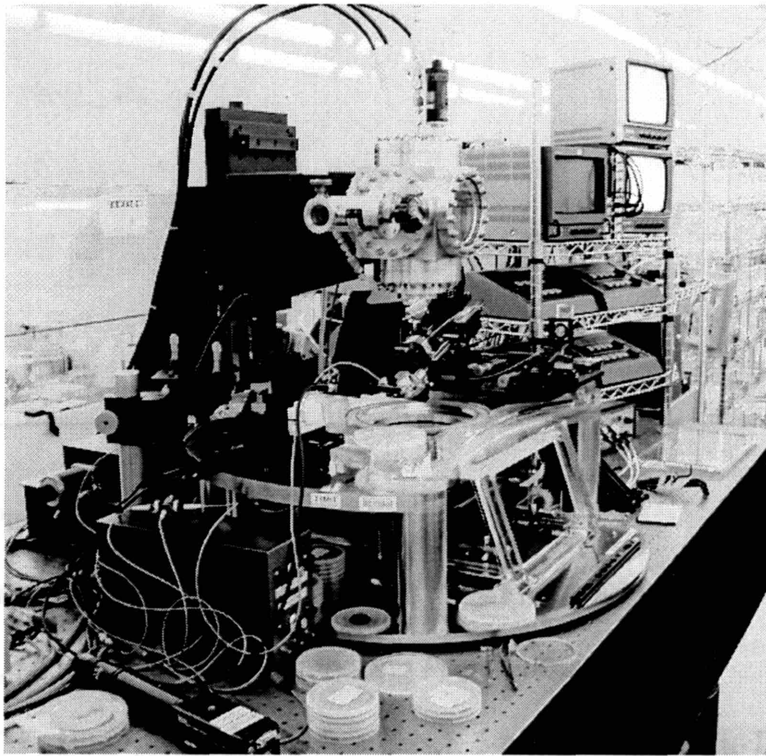

BIBLIOGRAPHY

[1] Hewlett-Packard, Providence, RI.

[2] J.P. Silverman, J. Vac. Sci. Technol. B **15**, 2117 (1997).

[3] S. Hector, Microelectronic Engineering Proceedings, 1997.

[4] A. Moel, E.E. Moon, R.D. Frankel, and H.I. Smith, J. Vac. Sci. Technol. B **11**, 2191 (1993).

[5] B. Fay, J. Trotel, and A. Frichet, J. Vac. Sci. Technol. **16**, 1954 (1979).

[6] National Instruments, Inc., Austin TX.

[7] Alacron, Inc. Nashua, NH.

[8] New England Affiliated Technologies, Lawrence, MA.

[9] Graftek Imaging, Inc., Austin, TX.

[10] National Instruments, Inc., Austin TX.

[11] H.I. Smith and M.L. Schattenburg, IBM J. Res. Develop Vol. 37 No. 3, 319 (1993).

[12] A. W. Yanof, G. L. Zipfel, and E. E. Moon, J. Vac. Sci. Technol. B **11**, 2920 (1993).

[13] A. Moel, W. Chu, K. Early, Y.-C. Ku, E.E. Moon, F. Tsai, and H.I. Smith, J.Vac. Sci. Technol. B **9**, 3287 (1991).

[14] Newport Corp., Irvine, CA.

[15] Queensgate Instruments, Ltd., Ascot, Berks UK.

[16] Delta F Corp., Woburn, MA.

[17] CVI Laser Corp., Albuquerque, NM.

[18] Omega Corp., Stamford, CT.

[19] Unphase Laser, Inc., San Jose, CA.

[20] OZ Optics, Ltd., Nepean, Ontario Canada.

[21] Moritex USA, Inc., San Diego, CA.

[22] Sony Corp., New York, NY.

[23] New Focus Inc., Santa Clara, CA.

[24] OZ Optics, Ltd., Nepean, Ontario Canada.

[25] E.E. Moon, P.N. Everett, K. Rhee, and H.I. Smith, J. Vac. Sci. Technol. B **14**, 3969 (1996).

[26] J. Ferrera, V.V. Wong, S. Rishton, V. Boegli, E.H. Anderson, D.P. Kern, and H.I. Smith, J. Vac. Sci. Technol. B **11**, 2342 (1993).

[27] E.E. Moon, P.N. Everett, and H.I. Smith, J. Vac. Sci. Technol. B **13**, 2648 (1995).

[28] E.E. Moon, J. Lee, P.N. Everett, and H.I. Smith, to be published in J. Vac. Sci. Technol. (1998).